IntechOpen

Electrocatalysts for Fuel Cells and Hydrogen Evolution

Theory to Design

Edited by Abhijit Ray, Indrajit Mukhopadhyay and Ranjan K. Pati

ELECTROCATALYSTS FOR FUEL CELLS AND HYDROGEN EVOLUTION - THEORY TO DESIGN

Edited by **Abhijit Ray, Indrajit Mukhopadhyay** and **Ranjan K. Pati**

Electrocatalysts for Fuel Cells and Hydrogen Evolution - Theory to Design
http://dx.doi.org/10.5772/intechopen.72563
Edited by Abhijit Ray, Indrajit Mukhopadhyay and Ranjan K. Pati

Contributors

Lindiwe Khotseng, Sang UCk Lee, Chi Ho Lee, Dan Xu, Winston Wu, Feng Yan, Adriana Marinoiu, Carcadea Elena, Aida Ghiulnare Pantazi, Raluca Mesterca, Simona Nica, Raceanu Mircea, Oana Tutunaru, Mihai Varlam, Marius Enachescu, Daniela Bala, Yuliya Yapontseva, Valeriy Kublanovsky

Notice

First published in London, United Kingdom, 2018 by IntechOpen
eBook (PDF) Published by IntechOpen, 2019
IntechOpen is the global imprint of INTECHOPEN LIMITED, registered in England and Wales, registration number: 11086078, The Shard, 25th floor, 32 London Bridge Street
London, SE19SG – United Kingdom
Printed in Croatia

British Library Cataloguing-in-Publication Data
A catalogue record for this book is available from the British Library

Additional hard and PDF copies can be obtained from orders@intechopen.com

Electrocatalysts for Fuel Cells and Hydrogen Evolution - Theory to Design
Edited by Abhijit Ray, Indrajit Mukhopadhyay and Ranjan K. Pati

p. cm.

Print ISBN 978-1-78984-812-0

Online ISBN 978-1-78984-813-7

eBook (PDF) ISBN 978-1-83881-705-3

Meet the editors

Dr. Abhijit Ray is an Associate Professor at the Pandit Deendayal Petroleum University (PDPU), India and currently heading the Department of Solar Energy. His current research works are focused on the development of eco-friendly functional materials and devices for photovoltaic, photo-/electro-chemical and capacitive energy conversion and storage applications.

Prof. Indrajit Mukhopadhyay is a Professor of PDPU, heading the Solar Research and Development Center at PDPU. He has been involved in establishing a modern laboratory with state-of-the-art facilities for carrying out frontier research in the field of solar photovoltaics.

Dr. Ranjan K. Pati is an Assistant Professor at the School of Petroleum Technology, PDPU. His research focuses are nanomaterials, oxide ceramics, and their application on fuel cell technology.

Contents

Preface

Electrocatalysts play a major role in two forms of green energy conversions: the controlled reaction of hydrogen and oxygen producing electricity in fuel cells, and the water-splitting reaction where water is reduced into hydrogen and oxygen in an up-hill thermodynamic process. They are equally important in new energy storage technologies, such as in re-chargeable metal-air batteries, where reduction of oxygen must be assisted by a catalyst. The science of electrocatalysis, which originated as a special field in electrochemistry, has seen tremendous progress after the late eighties due to several applications not only in chemistry, but also in chemical and industrial engineering. The field of electrocatalysis is still one of the most studied fields in research and development with emerging and advanced materials. Some of these materials are nano-carbon forms, including graphene, other materials are nanostructured two-dimensional materials, such as transition metal dichalcogenides (TMDCs) (MoS_2, WS_2 etc), metal-carbides, -nitrides, and –phosphide etc. This book is intended to bring together various theoretical and experimental aspects of designing efficient electrocatalysts for two major applications of oxygen reduction reactions in the fuel cells and hydrogen evolution reaction (HER) in water-splitting cells.

This book starts with a theoretical understanding of electrocatalysis in the framework of density functional theory followed by a vivid review of oxygen reduction reactions. A special emphasis has been placed on electrocatalysts for a proton-exchange membrane-based fuel cell where graphene with noble metal dispersion plays a significant role in electron transfer at thermodynamically favourable conditions. The latter part of the book deals with two major TMDCs with high economic viability, MoS_2 and WS_2 for their prospects in HER activities.

We trust that readers with a specific interest in the subject and above research, development and applications will find the book convenient and informative.

Dr. Abhijit Ray
Pandit Deendayal Petroleum University, India

Prof. Indrajit Mukhopadhyay
Pandit Deendayal Petroleum University, India

Dr. Ranjan K. Pati
Pandit Deendayal Petroleum University, India

Section 1

Electrocatalysts for Fuel Cells

Chapter 1

Theoretical Basis of Electrocatalysis

Chi Ho Lee and Sang Uck Lee

Additional information is available at the end of the chapter

http://dx.doi.org/10.5772/intechopen.77109

Abstract

In this chapter, we introduce the density functional theory (DFT)-based computational approaches to the study of various electrochemical reactions (hydrogen evolution reaction (HER), oxygen evolution reaction (OER), oxygen reduction reaction (ORR)) occurring on heterogeneous catalysis surfaces. A detailed computational approach to the theoretical interpretation of electrochemical reactions and structure-catalytic activity relationships for graphene-based catalysts will be discussed. The electrocatalytic activity of catalysis can be theoretically evaluated by overpotential value determined from free energy diagram (FED) of electrochemical reactions. By comparing electrocatalytic activity of systematically designed graphene-based catalysts, we will discuss the structure-catalytic activity relationships, especially the electronic and geometrical effects of heteroatom dopants.

Keywords: DFT, electrocatalysis, HER, OER, ORR, FED, overpotential, dopant, carbon

1. Introduction

With the climate change, fast consumption of fossil fuels, and environment situations due to carbon release, the research and development of clean energy is of vital importance in the coming decades. Promising applications of electrocatalysis for clean energy conversion, for example fuel cells, water electrolysis, metal-air batteries, and CO_2 to fuel conversion, are the subjects of both extensive fundamental and utilitarian studies. These technologies play a crucial role in the future of sustainable energy utilization infrastructure, and thus huge research efforts have been dedicated to improving the electrocatalytic activity of these reactions, which include electrocatalytic oxygen reduction reaction (ORR), and hydrogen oxidation reaction (HOR) that occur on the cathode and anode of a hydrogen-oxygen fuel cell, respectively, and hydrogen evolution reaction (HER) and oxygen evolution reaction (OER) at the

cathode and the anode of an electrolytic cell producing gaseous molecular hydrogen and oxygen, respectively. These reactions play an important role in regenerative fuel cells and dominate their overall performance [1–5]. Understanding the HER/OER/ORR mechanisms of various catalysts could provide design guidelines for material and process development, as well as facilitating the discovery of new catalysts. Above all, the detailed OER/ORR mechanisms in acid/alkaline environment are still being studied. Generally, OER/ORR can proceed in Langmuir-Hinshelwood (LH) or Eley-Rideal (ER) mechanisms [6]. The LH mechanism comprises all reactive intermediates on the surface while the ER mechanism includes species from the electrolyte that reacts with the surface intermediate. Despite the controversy over the mechanism, ER mechanism is generally accepted with lower reaction energy barrier than that of LH mechanism [7], and many researchers have conducted theoretical studies on OER/ORR based on the ER mechanism. However, there are two feasible reaction pathways in ER mechanism, two-step pathway and four-step pathway depending on the relative stability of O* and OOH* intermediates generated after the adsorption of O_2 on the catalyst [8]. Thus, we sought to describe the detailed reaction pathway of the OER/ORR as well as proposing solutions for the determination of the preferred reaction pathway on the ER mechanism.

Precious metals such as platinum (Pt), iridium (Ir), and ruthenium (Ru)-based catalysts [9–11] are generally needed to promote the HER for the generation of hydrogen fuel from the electrochemical splitting of water, the ORR in fuel cells for energy conversion, and the OER in metal-air batteries for energy storage. Besides the requirement for high catalytic activity, other issues related to these catalysts are their limited reserves and comparatively high cost, which have precluded these renewable energy technologies from large-scale commercial applications. In this regard, huge amount of efforts has been devoted to develop novel electrocatalysts to completely or partially replace precious metal catalysts in energy technologies. Along with the intensive research efforts in developing nonprecious electrocatalysts to reduce or to replace precious metal catalysts, various carbon-based, metal-free catalysts have been extensively studied because they have unique advantages for designated catalysis due to their tunable molecular structures, abundance and strong tolerance to acid/alkaline environments when used as alternative HER/OER/ORR catalysts. A rapidly growing field of metal-free catalysis based on carbon-based materials has developed, and a substantial amount of literature in both on the theoretical and experimental fields has been generated. Recent studies have revealed that graphene, [12] graphite, [13] vertically aligned nitrogen-doped carbon nanotubes (VA-NCNTs), [14] heteroatom-doped CNTs, [15] and nitrogen-doped graphene sheets [16] have excellent catalytic performance. The presence of N in N-doped graphene leads to more chemically active sites, a high density of defects and high electrochemical activity. Due to these enhanced electronic properties, N-doped catalysts in the C network are attractive for a wide range of applications, including as metal-free catalysts for HER/OER/ORR in fuel cell systems. Recently, carbon nitride-based catalysts (C_3N_4 and C_2N) with N-rich including both graphitic and pyridinic N moieties is a promising catalyst due to its competitiveness over a wide range of electrocatalyst processes, despite pure C_3N_4 and C_2N itself being inert with regard to HER/OER/ORR activity. Here, we attempted to enhance the catalytic activity of graphene, C_3N_4 and C_2N by introducing heteroatoms, which is an effective way to manipulate its electronic structure and electrochemical properties.

In this chapter, we will introduce metal-free bifunctional electrocatalysts of the heteroatom-doped graphenes (GXs, where G and X represent graphene and the heteroatom dopant) for HER [17] and the heteroatom-doped C_3N_4 (X_Y-C_3N_4s, where X and Y indicate the dopant and doping site on C_3N_4, respectively) for OER/ORR [18–20]. From the doping effect which shows better performance for HER/OER/ORR, we first present evidence that structural deformation and periodic lattice defects play the fundamental role in the HER activity of GXs by adjusting the electronic properties of graphene. We found that graphene doped with third row elements has higher HER activity with out-of-plane structural deformation compared to graphene doped with second row elements, in which graphene tends to maintain its planar structure. We systematically describe a structure-activity relationship in GXs for HER based on a thorough understanding of the effects of dopants, respectively. In addition, the third row elements-doped graphenes (GSi, GP and GS) show an interesting regularity described by a simple 3 N rule: GXs give outstanding HER activity with sustained metallic property when its primitive cell size has 3×3 N (N is integral) supercell size of pure graphene. Secondly, we describe not only the detailed OER/ORR mechanisms but also improved OER/ORR activity of C_3N_4 by introducing dopants such as P or S into the C_3N_4 matrix. Especially, we explore the causes of variation in HER/OER/ORR performance with respect to the type of dopant by comparing geometric and electronic structures of GXs and X_Y-C_3N_4s.

From these geometric and electronic structures, we demonstrated that GXs [17] and X_Y-C_3N_4 [18–20] show outstanding HER/OER/ORR activity with synergistic geometric and electronic effects, which coordinatively increase unsaturated sp^3-C via structural deformation and improve electrical conductance by modulating the electronic structure with extra electrons from dopants. Our theoretical investigations suggest that the synergistic effect between geometric and electronic factors plays an important role in HER/OER/ORR catalytic activities. It can be emphasized that there is a close correlation between the geometric/electronic structure and HER/OER/ORR catalytic activities. This understanding of the structure-activity relationship will give an insight into the development of new highly efficient electrocatalytic materials.

2. Theoretical background

2.1. Hydrogen evolution reaction

HER is a multistep process that takes place on the surface of catalyst, and there are two proposed mechanisms: Volmer-Heyrovsky and Volmer-Tafel. Both Volmer-Heyrovsky and Volmer-Tafel mechanisms describe the hydrogen atom adsorption and hydrogen molecule desorption reactions among (1) an initial state $2H^+ + 2e^-$, (2) an intermediate adsorbed state $H^* + H^+ + e^-$ or $2H^*$, and (3) a final product state $2H^+ + 2e^-$, where the $*$ and H^* denote the active site and adsorbed hydrogen atom on the surface of the catalyst, respectively. Because the initial and final states are equivalent at equilibrium reduction potential, U = 0, the Gibbs free energy of the intermediate state, $|\Delta G_{H^*}|$, has been considered as a major descriptor of the HER activity for a wide variety of catalysts. Therefore, the optimum value of $|\Delta G_{H^*}|$ should be zero for a spontaneous reaction without activation energy barrier. The Pt catalyst facilitates HER

with a low activation energy, $|\Delta G_{H^*}|$~0.09 eV [21]. In this work, we have considered the Volmer-Tafel mechanism to calculate the Gibbs free energy of the intermediate state, $\Delta G_{H^*}^{Volmer}(\theta_{H1^*})$, $\Delta G_{H^*}^{Volmer}(\theta_{H2^*})$, $\Delta G_{H^*}^{Heyrovsky}(\theta_{H1^*})$, and $\Delta G_{H^*}^{Tafel}(\theta_{H2^*})$ with different hydrogen coverage at the active sites, θ_{H1^*}, and θ_{H2^*}, as shown in **Figure 1**. The Gibbs free energy of the adsorbed hydrogen is calculated as:

$$\Delta G_{H^*} = \Delta E_{H^*} + \Delta E_{ZPE} - T\Delta S_H \tag{1}$$

where ΔE_{H^*} is hydrogen adsorption energy and ΔE_{ZPE} is the difference in zero point energy (ZPE) between the adsorbed state and the gas phase. ΔS_H refers to the entropy of adsorption of $1/2H_2$, which is the $\Delta S_H \simeq -1/2S_{H_2}^0$, where $S_{H_2}^0$ is the entropy of H_2 in the gas phase at STP. ZPE and entropic corrections, $\Delta E_{ZPE} - T\Delta S_H$ of the heteroatom-doped graphenes (GXs, where G and X represent graphene and the heteroatom dopant), are listed in **Table 1**. The hydrogen adsorption energy ΔE_{H^*} can be defined in two ways: the integral and differential H adsorption energy as a function of the H coverage in Eqs. (2) and (3), respectively.

The gas phase values were from reference 17, while the values for the adsorbed species were taken from DFT calculations. The same values for the adsorbed species for all the N X N models were used, as vibrational frequencies have been found to depend much less on the surface than the bond strength.

$$E_{H^*}^{int}(n) = 1/2[E(surf + nH^*) - E(surf)] - 1/2E(H_2) \tag{2}$$

$$E_{H^*}^{diff}(\theta_{H^*}) = \delta E_{H^*}^{int}(n)/\delta n = \left[E_{H^*}^{int}(n) - E_{H^*}^{int}(n-1)\right]/\Delta n \tag{3}$$

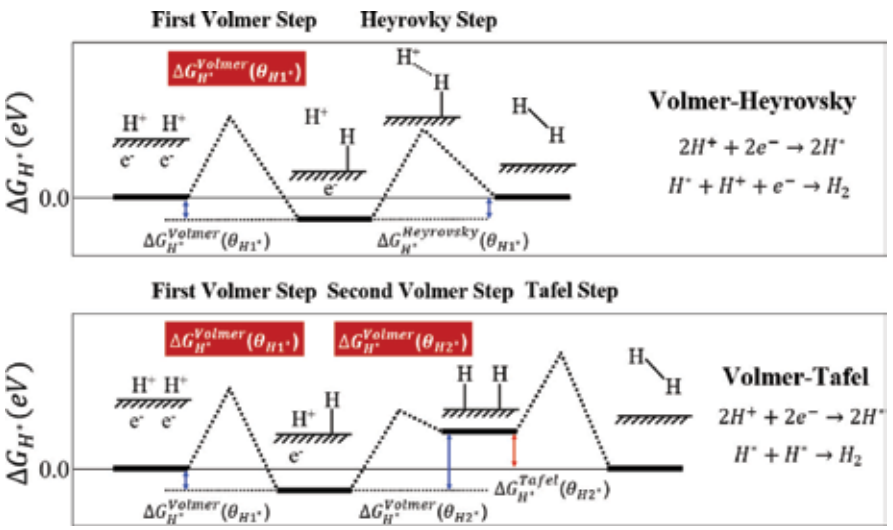

Figure 1. Schematic of Volmer-Heyrovsky and Volmer-Tafel mechanisms. $\Delta G_{H^*}^{Volmer}(\theta_{H1^*})$, $\Delta G_{H^*}^{Volmer}(\theta_{H2^*})$, $\Delta G_{H^*}^{Heyrovsky}(\theta_{H1^*})$, and $\Delta G_{H^*}^{Tafel}(\theta_{H2^*})$ are free energies of the first-, and second-Volmer steps, Hyrovsky and Tafel step, where θ_{H1^*}, and θ_{H2^*} indicate different hydrogen coverage of active sites.

eV	ZPE	TS	△ZPE	T△S	△ZPE- T△S
G-H*	0.25	—	0.11	−0.21	0.32
GB-H*	0.25	—	0.12	−0.21	0.32
GN-H*	0.29	—	0.16	−0.21	0.36
GP-H*	0.30	—	0.17	−0.21	0.37
GS-H*	0.31	—	0.18	−0.21	0.38
GSi-H*	0.30	—	0.17	−0.21	0.37
H_2	0.27	0.41	—	—	—

Table 1. Zero point energy (ZPE) and entropic (TS) correction for heteroatom doped-graphenes (G, GB, GN, GP, and GSi) at 298 K.

where n, H^* and θ_{H^*} refer to the number of hydrogen atoms, adsorbed hydrogen on the surface, and hydrogen coverage, respectively.

In contrast to the single hydrogen reaction of the Volmer step, two hydrogen atoms mediate the Tafel step. Therefore, we obtain the Gibbs free energy of the intermediate state during the Volmer and Tafel steps with the following equations to determine the different hydrogen coverages of active sites.

$$\Delta G_{H^*}^{Volmer} = \Delta E_{H^*}^{Volmer} + \Delta E_{ZPE} - T\Delta S \tag{4}$$

$$\Delta E_{H^*}^{Volmer} = E_{H^*}^{diff}(\theta_{H^*}) = [E_{H^*}^{ins}(n) - E_{H^*}^{ins}(n-1)]/\Delta)] \qquad \Delta n = 1 \tag{5}$$

$$\Delta G_{H^*}^{Tafel} = \Delta E_{H^*}^{Tafel} + \Delta E_{ZPE} - T\Delta S \tag{6}$$

$$\Delta E_{H^*}^{Tafel} = E_{H^*}^{diff}(\theta_{H^*}) = [E_{H^*}^{ins}(n-2) - E_{H^*}^{ins}(n)]/\Delta n) \qquad \Delta n = 2 \tag{7}$$

2.2. Oxygen evolution reaction and oxygen reduction reaction

2.2.1. Reaction pathways in alkaline media

The generally acceptable OER mechanism is the four-electron associative mechanism in alkaline media. The four elementary steps of OER mechanism are described as follows:

$$OH^- + * \rightarrow OH^* + e^- \tag{8}$$

$$OH^* + OH^- \rightarrow O^* + H_2O(l) + e^- \tag{9}$$

$$O^* + OH^- \rightarrow OOH^* + e^- \tag{10}$$

$$OOH^* + OH^- \rightarrow * + O_2(g) + H_2O(l) + e^- \tag{11}$$

where * represents the active site on the surface, *(l)* and *(g)* refer to liquid and gas phases, respectively, and O^*, OH^* and OOH^* are adsorbed intermediates.

In contrast to OER, ORR can proceed either by a two-step or four-step pathways depending on the relative stability of O^* and OOH^* intermediates generated after the adsorption of O_2 on the catalyst. The two-step pathway of ORR in alkaline environment is summarized using the following elementary steps,

$$O_2 + H_2O(l) + 2e^- \rightarrow O^* + 2OH^- \tag{12}$$

$$O^* + 2OH^- + H_2O(l) + 2e^- \rightarrow 4OH^- \tag{13}$$

whereas the four-step pathway has following elementary steps:

$$O_2 + H_2O(l) + e^- \rightarrow OOH^* + OH^- \tag{14}$$

$$OOH^* + e^- \rightarrow O^* + OH^- \tag{15}$$

$$O^* + H_2O(l) + e^- \rightarrow OH^* + OH^- \tag{16}$$

$$OH^* + e^- \rightarrow * + OH^- \tag{17}$$

Looking at the elementary reaction steps of ORR, both reaction pathways lead to the same final products as $4OH^-$ and the different intermediate states after the adsorption of O_2 on the catalyst, O^* in (Eq. (12)) and OOH^* in (Eq. (14)). Therefore, it is worth mentioning that the transformation step of O_2^* to O^* in (Eq. (12)) or O_2^* to OOH^* in (Eq. (14)) can be important index to determine the ORR pathway.

2.2.2. Derivation of the free energy relations

The free energy change of each elementary reaction of OER in alkaline media can be expressed as follows:

$$\Delta G_1 = G_{OH^*} + \mu_{e^-} - \left(\mu_{OH^-} + G_*\right) \tag{18}$$

$$\Delta G_2 = G_{O^*} + \mu_{H_2O(l)} + \mu_{e^-} - \left(G_{OH^*} + \mu_{OH^-}\right) \tag{19}$$

$$\Delta G_3 = G_{OOH^*} + \mu_{e^-} - \left(G_{O^*} + \mu_{OH^-}\right) \tag{20}$$

$$\Delta G_4 = G_* + \mu_{O_2} + \mu_{H_2O(l)} + \mu_{e^-} - \left(G_{OOH^*} + \mu_{OH^-}\right) \tag{21}$$

Therefore, the free energy change of each elementary reaction can be calculated using (1) the chemical potentials of hydroxide, electron, liquid water and oxygen molecule (μ_{OH^-}, μ_{e^-}, $\mu_{H_2O(l)}$ and μ_{O_2}) and (2) the free energies of each intermediate (G_{OH^*}, G_{O^*}, and G_{OOH^*}) on the surface of catalyst (*). In the following paragraph, we describe the theoretical method to calculate the free energy change of each elementary reaction of the proposed reaction path based on the relation between the standard electrode potential and the chemical potential of hydroxides and electrons in alkaline environment.

2.2.3. The chemical potentials of OH^-, e^-, H_2O, and O_2

In alkaline environment, the standard oxygen reduction reaction is described as follows:

$$O_2(g) + 2H_2O(l) + 4e^- \rightarrow 4OH^- \qquad E^0 = 0.402V \tag{22}$$

and the standard reduction potential (μ^0) is 0.402 V at T = 298.15 K. In terms of chemical potentials, the equations are expressed as follows:

$$\mu_{o_2(g)} + 2\mu_{H_2O(l)} + 4\mu_{e^-} = 4\mu_{OH^-} \tag{23}$$

$$\mu_{e^-} - \mu_{OH^-} = -1/4\left(\mu_{O_2(g)} + 2\mu_{H_2O(l)}\right) \tag{24}$$

The left side in (Eq. (24)), the chemical potentials of electron and hydroxide, could be derived further as follows:

$$\mu_{e^-} = \mu_e^0 - eU \tag{25}$$

$$\mu_{OH^-} = \mu_{OH}^0 + \kappa_B T ln a_{OH^-} \tag{26}$$

where eU represents the shift in electron energy when a bias is applied and μ_e^0, $\mu_{OH^-}^0$ represent the chemical potentials of electron and hydroxide at standard conditions ($a_{OH^-} = 1, T = 298.15K,$ and $eU = E^0 = 0.402V$). Therefore,

$$\mu_{e^-} - \mu_{OH^-} = (\mu_e^0 - eU) - \left(\mu_{OH}^0 + \kappa_B T ln a_{OH^-}\right) \tag{27}$$

$$\mu_{e^-} - \mu_{OH^-} = \mu_e^0 - \mu_{OH}^0 - eU = -1/4\left(\mu_{O_2(g)} + 2\mu_{H_2O(l)}\right) \tag{28}$$

at standard and equilibrium conditions $\left(a_{OH^-} = 1, T = 298.15K, \text{ and } eU = E^0 = 0.402V\right)$. In the case of the right side in Eq. (24), the chemical potentials of liquid water and oxygen molecule ($\mu_{H_2O(l)}$ and $\mu_{O_2(g)}$) can be calculated from the approximations proposed by Norskov et al., where the chemical potential of liquid water ($\mu_{H_2O(l)}$) is equal to the chemical potential of water in the gas phase ($\mu_{H_2O(g)}$), at T = 298.15 K and 0.035 bars.

$$\mu_{H_2O(l)} = \mu_{H_2O(g)} = E_{DFT}^{H_2O(g)} + ZPE_{H_2O(g)} - TS_{H_2O(g)}^0 \tag{29}$$

Moreover, the chemical potential of oxygen molecule ($\mu_{O_2(g)}$) is derived from the standard free energy change of the reaction:

$$1/2O_2(g) + H_2(g) \leftrightarrow H_2O(l) \tag{30}$$

Because the experimental standard free energy change is −2.46 eV, the equation can be written as:

$$G_{H_2O(l)}^0 - 1/2G_{O_2(g)}^0 - G_{H_2(g)}^0 = -2.46eV \tag{31}$$

Therefore, the chemical potential of oxygen molecule ($\mu_{O_2(g)}$) can be approximately calculated as follows:

$$\begin{aligned}\mu_{O_2(g)} = 4.92 + 2\left(E_{DFT}^{H_2O(g)} + ZPE_{H_2O(g)} - TS_{H_2O(g)}^{0}\right) \\ - 2\left(E_{DFT}^{H_2(g)} + ZPE_{H_2(g)} - TS_{H_2(g)}^{0}\right)\end{aligned} \tag{32}$$

Therefore, Eq. (24) can be written as:

$$\mu_{e^-} - \mu_{OH^-} - eU = -1/4\left(\mu_{O_2(g)} + 2\mu_{H_2O(g)}\right) \tag{33}$$

Finally, we can obtain $\mu_{e^-}^{0} - \mu_{OH^-}^{0} - eU$ value as 9.952 eV using the (Eq. (29)), (Eq. (32)) and (Eq. (33)) [20]. The enthalpy change (E_{DFT}), the zero-point energy correction (Δ_{ZPE}) calculated by the DFT calculations of vibrational frequencies, and entropy corrections (TS) are listed in **Table 2**.

Gas phase H_2O at 0.035 bar was used as the reference state because at this pressure gas phase H_2O is in equilibrium with liquid water at 300 K. The same values for the adsorbed species for all the models were used, as vibrational frequencies have been found to depend much less on the surface than the bond strength. We took the standard entropies from thermodynamic tables for gas phase molecules.

2.2.4. The free energies of each intermediate (G_{OH^*}, G_{O^*}, and G_{OOH^*}) on the surface of catalyst (*)

Step 1. $\boldsymbol{OH^- + * \rightarrow OH^* + e^-}$

The first step is the adsorption step of active site with a release of an electron:

$$\begin{aligned}\Delta G_1 &= G_{OH^*} + \mu_{e^-} - \left(\mu_{OH^-} + G_*\right) \\ &= \left(G_{OH^*} - G_*\right) + \left(\mu_{e^-}^{0} - \mu_{OH^-}^{0} - eU\right)\end{aligned} \tag{34}$$

where respectively and could be expressed by DFT energies:

Species	E (eV)	ZPE (eV)	TS (eV)
H_2O (0.035 bar)	−14.22	0.56	0.67
H_2	−6.76	0.27	0.41
O*	—	0.09	0.05
OH*	—	0.41	0.07
OOH*	—	0.46	0.16

Table 2. Total energies (E) of H_2O and H_2 and zero point energy (ZPE) corrections and entropic contributions (TS) to the free energies.

$$G_{OH^*} = E_{DFT}^{OH^*} + ZPE_{OH^*} - TS_{OH^*}^0 \tag{35}$$

$$G_* = G_{OH^*} \tag{36}$$

Replacing (Eq. (33)), (Eq. (35)) and (Eq. (36)) in (Eq. (34)) we get:

$$\begin{aligned} \Delta G_1 &= \left[\left(E_{DFT}^{OH^*} + ZPE - TS^0\right) - E_{DFT}^*\right] + \left(\mu_{e^-}^0 - \mu_{OH^-}^0 - eU\right) \\ &= \left[\left(E_{DFT}^{OH^*} + ZPE - TS^0\right) - E_{DFT}^*\right] + 9.952eV \end{aligned} \tag{37}$$

Step 2: $\boldsymbol{OH^* + OH^- \rightarrow O^* + H_2O(l) + e^-}$

The second step is oxidation of the OH^* species to O^* with release of water and an electron:

$$\begin{aligned} \Delta G_2 &= G_{O^*} + \mu_{H_2O(l)} + \mu_{e^-} - \left(G_{OH^*} + \mu_{OH^-}\right) \\ &= \left(G_{O^*} + \mu_{H_2O(l)} - G_{OH^*}\right) + \left(\mu_{e^-}^0 - \mu_{OH^-}^0 - eU\right) \end{aligned} \tag{38}$$

The relation for G_{O^*} in terms of DFT energies is similar to the relation for (Eq. (35)). Replacing again the same equations as in the case for the first step in (Eq. (38)) we get:

$$\Delta G_2 = \left[\left(E_{DFT}^{O^*} + E_{DFT}^{H_2O(g)}\right) - E_{DFT}^{OH^*} + \left(\Delta ZPE\text{-}T\Delta S^0\right)\right] + 9.952eV \tag{39}$$

Step 3: $\boldsymbol{O^* + OH^- \rightarrow OOH^* + e^-}$

The third step is represented by formation of the OOH^* on top of oxygen with a release of an electron:

$$\begin{aligned} \Delta G_3 &= G_{OOH^*} + \mu_{e^-} - \left(G_{O^*} + \mu_{OH^-}\right) \\ &= \left(G_{OOH^*} - G_{O^*}\right) + \left(\mu_{e^-}^0 - \mu_{OH^-}^0 - eU\right) \end{aligned} \tag{40}$$

The relation for G_{OOH^*} and G_{O^*} in terms of DFT energies is similar to the relation for (Eq. (35)). The same equations are replaced gradually in the (Eq. (40)) as follows:

$$\Delta G_3 = \left[E_{DFT}^{OOH^*} - E_{DFT}^{O^*} + \left(\Delta ZPE\text{-}T\Delta S^0\right)\right] + 9.952eV \tag{41}$$

Step 4: $\boldsymbol{OOH^* + OH^- \rightarrow * + O_2(g) + H_2O(l) + e^-}$

The last step is the evolution of oxygen molecule:

$$\begin{aligned} \Delta G_4 &= G_* + \mu_{O_2(g)} + \mu_{H_2O(l)} + \mu_{e^-} - \left(G_{OOH^*} + \mu_{OH^-}\right) \\ &= \left(G_* + \mu_{O_2(g)} + \mu_{H_2O(l)} - G_{OOH^*}\right) + \left(\mu_{e^-}^0 - \mu_{OH^-}^0 - eU\right) \end{aligned} \tag{42}$$

Therefore, we leave from the following equation:

$$\Delta G_4 = \left[E^*_{DFT} + \left(4.92 + 2\left(E^{H_2O(g)}_{DFT} - E^{H_2(g)}_{DFT}\right)\right) + E^{H_2O(g)}_{DFT}\right] - E^{OOH^*}_{DFT} + \left(\Delta ZPE\text{-}T\Delta S^0\right)] + 9.952eV \tag{43}$$

Finally, the summation of ΔG_1, ΔG_2, ΔG_3, and ΔG_4 should be 1.608 eV.

The reaction free energies of *O*, OH** and *OOH** species on the surface of catalyst are corrected by ZPE and TS. Moreover, the free energy relations of the ORR in alkaline media can also be explained in the same vein as the OER above mentioned [20].

2.2.5. Reaction pathways in acidic media

The generally acceptable OER mechanism is the four-electron associative mechanism in acidic media. The four elementary steps of OER mechanism are described as follows:

$$H_2O(l) + * \rightarrow OH^* + H^+ + e^- \tag{44}$$

$$OH^* \rightarrow O^* + H^+ + e^- \tag{45}$$

$$O^* + H_2O(l) \rightarrow OOH^* + H^+ + e^- \tag{46}$$

$$OOH^* \rightarrow * + O_2(g) + H^+ + e^- \tag{47}$$

where * represents the active site on the surface, (l) and (g) refer to liquid and gas phases, respectively, and O^*, OH^* and OOH^* are adsorbed intermediates. The ORR can proceed completely via a direct four-electron process in which $O_2(g)$ is reduced directly to water H_2O (g), without involvement of hydrogen peroxide. The ORR mechanism is summarized using the following elementary steps,

$$O_2(g) + H^+ + e^- \rightarrow OOH^* \tag{48}$$

$$OOH^* + H^+ + e^- \rightarrow O^* + H_2O(l) \tag{49}$$

$$O^* + H^+ + e^- \rightarrow OH^* \tag{50}$$

$$OH^* + H^+ + e^- \rightarrow * + H_2O(l) \tag{51}$$

Here, we took the OER reactions ((44)–(47)) to derive the thermochemistry of both OER/ORR, because the ORR reactions (Eqs. ((48)–(51)) are inversed from the OER reactions (Eqs. ((44)–(47)). The catalytic activity of the OER/ORR processes can be determined by examining the reaction free energies of the different elementary steps.

2.2.6. Derivation of the free energy relations

The free energy change of each elementary reaction of OER can be expressed as follows:

$$\Delta G_1 = G_{OH^*} + \mu_{H^+} + \mu_{e^-} - \left(\mu_{H_2O(l)} + G_*\right) \tag{52}$$

$$\Delta G_2 = G_{O^*} + \mu_{H^+} + \mu_{e^-} - (G_{OH^*}) \tag{53}$$

$$\Delta G_3 = G_{OOH^*} + \mu_{H^+} + \mu_{e^-} - \left(G_{O^*} + \mu_{H_2O(l)}\right) \tag{54}$$

$$\Delta G_3 = G_* + \mu_{O_2(g)} + \mu_{H^+} + \mu_{e^-} - (G_{OOH^*}) \tag{55}$$

Therefore, the free energy change of each elementary reaction can be calculated using (1) the chemical potentials of proton, electron, liquid water and oxygen molecule (μ_{H^+}, μ_{e^-}, $\mu_{H_2O(l)}$, and $\mu_{O_2(g)}$), and (2) the free energies of each intermediate (G_{OH^*}, G_{O^*}, and G_{OOH^*}) on the surface of catalyst (*). In the following paragraph, we describe the theoretical method to calculate the free energy change of each elementary reaction of the proposed reaction path based on the relation between the standard electrode potential and the chemical potential of protons and electrons in acidic environment.

2.2.7. The chemical potentials of H^+, and e^-

In acidic environment, the standard hydrogen electrode is based on the redox half-cell,

$$H^+(aq) + e^- \rightarrow 1/2H_2(g) \qquad E^0 = 0.00\ V \tag{56}$$

and the standard reduction potential (E^0) is 0.00 V at T = 298.15 K. In terms of chemical potentials, the equation is expressed as follows:

$$\mu_{H^+} + \mu_{e^-} = 1/2\mu_{H_2(g)} \tag{57}$$

In (Eq. (57)), the chemical potentials of proton, electron and hydrogen could be derived further as follows:

$$\mu_{H^+} = \mu^0_{H^+} - \kappa_B T ln a_{H^+} \tag{58}$$

$$\mu_{e^-} = \mu^0_{e^-} - eU \tag{59}$$

$$\mu_{H_2(g)} = \mu^0_{H_2} - \kappa_B T ln p_{H_2} \tag{60}$$

where eU represents the shift in electron energy when a bias is applied and $\mu^0_{e^-}$, $\mu^0_{H^+}$ represent the chemical potentials of electron and proton at standard conditions ($a_{H^+} = 1, p_{H_2} = 1bar, T = 298.15K$). Therefore,

$$\mu^0_{H^+} + \mu^0_{e^-} = 1/2\mu^0_{H_2(g)} \tag{61}$$

at standard and equilibrium conditions ($a_{H^+} = 1$, $p_{H_2} = 1bar$, $T = 298.15K$, and $eU - E^0 = 0.00V$). In the case of the right side in (Eq. (61)), we can define the standard chemical potential of hydrogen on the DFT scale from computational point of view:

$$\mu_{H_2}^0 = E_{DFT}^{H_2(g)} + ZPE_{H_2(g)} - TS_{H_2(g)}^0 \tag{62}$$

Another approximation is that for liquid water and oxygen molecule, $\mu_{H_2O(l)}$ and $\mu_{O_2(g)}$ can also be explained in the same vein as the OER in the alkaline media above mentioned.

2.2.8. The free energies of each intermediate (G_{OH^*}, G_{O^*}, and G_{OOH^*}) on the surface of catalyst (*)

Step 1: $H_2O(l) + * \rightarrow OH^* + H^+ + e$

The first step is the adsorption step of OH^* on active site with a release of a proton and an electron:

$$\begin{aligned} \Delta G_1 &= G_{OH^*} + \mu_{H^+} + \mu_{e^-} - \left(\mu_{H_2O(l)} + G_*\right) \\ &= \left(G_{OH^*} - \mu_{H_2O(l)} + G_*\right) + \left(\mu_{H^+}^0 + \mu_{e^-}^0 - eU\right) \end{aligned} \tag{63}$$

where G_{OH^*} and G_* are expressed by DFT energies:

$$G_{OH^*} = E_{DFT}^{OH^*} + ZPE_{OH^*} - TS_{OH}^0 \tag{64}$$

$$G_* = E_{DFT}^* \tag{65}$$

Replacing (Eq. (29)), (Eq. (62)), (Eq. (64)) and (Eq. (65)) in (Eq. (63)) we get:

$$\begin{aligned} \Delta G_1 &= \left[\left(E_{DFT}^{OH^*} - E_{DFT}^{H_2O(g)} - E_{DFT}^*\right) + \left(\Delta ZPE - T\Delta S^0\right)\right] \\ &\quad + \left(\mu_{H^+}^0 + \mu_{e^-}^0 - eU\right) \\ &= \left[\left(E_{DFT}^{OH^*} - E_{DFT}^{H_2O(g)} - E_{DFT}^*\right) + \left(\Delta ZPE - T\Delta S^0\right)\right] \\ &\quad + \left(1/2E_{DFT}^{H_2(g)} - eU\right) \end{aligned} \tag{66}$$

Step 2: $OH^* \rightarrow O^* + H^+ + e$

The second step is oxidation of the OH^* species to O^* with release of a proton and an electron:

$$\begin{aligned} \Delta G_2 &= G_{O^*} + \mu_{H^+} + \mu_{e^-} - G_{OH^*} \\ &= \left(G_{O^*} - G_{OH^*}\right) + \left(\mu_{H^+}^0 + \mu_{e^-}^0 - eU\right) \end{aligned} \tag{67}$$

The relation for G_{O^*} in terms of DFT energies is similar to the relation for (Eq. (64)). Replacing again the same equations as in the case for the first step in (Eq. (66)), we get:

$$\Delta G_2 = \left[\left(E_{DFT}^{O^*} - E_{DFT}^{OH^*}\right) + \left(\Delta ZPE - T\Delta S^0\right)\right] + \left(1/2E_{DFT}^{H_2(g)} - eU\right) \tag{68}$$

Step 3: $O^* \rightarrow OOH^* + H^+ + e^-$

The third step is represented by formation of the O^* on top of oxygen with a release of a proton and an electron:

$$\begin{aligned}\Delta G_3 &= G_{OOH^*} + \mu_{H^+} + \mu_{e^-} - G_{O^*} \\ &= (G_{OOH^*} - G_{O^*}) + \left(\mu^0_{H^+} + \mu^0_{e^-} - eU\right)\end{aligned} \tag{69}$$

The relation for $G_{(OOH^*)}$ and G_{O^*} in terms of DFT energies is similar to the relation for (Eq. (64)). The same equations are replaced gradually in the (Eq. (69)) as follows:

$$\Delta G_3 = \left[\left(E^{OOH^*}_{DFT} - E^{O^*}_{DFT}\right) + \left(\Delta ZPE\text{-}T\Delta S^0\right)\right] + \left(1/2E^{H_2(g)}_{DFT} - eU\right) \tag{70}$$

Step 4: $OOH^* \rightarrow * + O_2(g) + H^+ + e$

The last step is the evolution of oxygen molecule:

$$\begin{aligned}\Delta G_4 &= G_* + \mu_{O_2(g)} + \mu_{H^+} + \mu_{e^-} - G_{OOH^*} \\ &= \left(G_* + \mu_{O_2(g)} - G_{OOH^*}\right) + \left(\mu^0_{H^+} + \mu^0_{e^-} - eU\right)\end{aligned} \tag{71}$$

Therefore, we leave from the following equation:

$$\begin{aligned}\Delta G_4 = &\left[E^*_{DFT} + \left(4.92 + 2\left(E^{H_2O(g)}_{DFT} - E^{H_2(g)}_{DFT}\right)\right) + E^{OOH^*}_{DFT}\right] \\ &+ \left(\Delta ZPE - T\Delta S^0\right) + \left(1/2E^{H_2(g)}_{DFT} - eU\right)\end{aligned} \tag{72}$$

Finally, the summation of ΔG_1, ΔG_2, ΔG_3, and ΔG_4 should be 4.92 eV.

The reaction free energies of OH^*, O^* and OOH^* species on the surface of catalyst considered by ZPE and TS. Moreover, the free energy relations of the ORR in acidic media can also be explained in the same vein as the OER above mentioned.

2.3. Free energy diagram (FED) and Overpotential(η)

We can deduce an important parameter of electrocatalytic activity from the calculated ΔG, the magnitude of the potential-determining step (G^{HER} and $G^{OER/ORR}$) in consecutive reaction steps. This is the specific reaction step with the largest ΔG in the HER and OER/ORR elementary reaction steps, that is, the concluding step to achieve a downhill reaction in the free energy diagram (FED) with increasing potential N, as shown in **Figure 2** for HER and **Figure 3** for OER/ORR:

$$G^{HER} = max\left[\Delta G^0_1, \Delta G^0_2\right] \tag{73}$$

$$G^{OER/ORR} = max\left[\Delta G^0_1, \Delta G^0_2, \Delta G^0_3, \Delta G^0_4\right] \tag{74}$$

$$G^{ORR} = max\left[\Delta G^0_1, \Delta G^0_2\right] \tag{75}$$

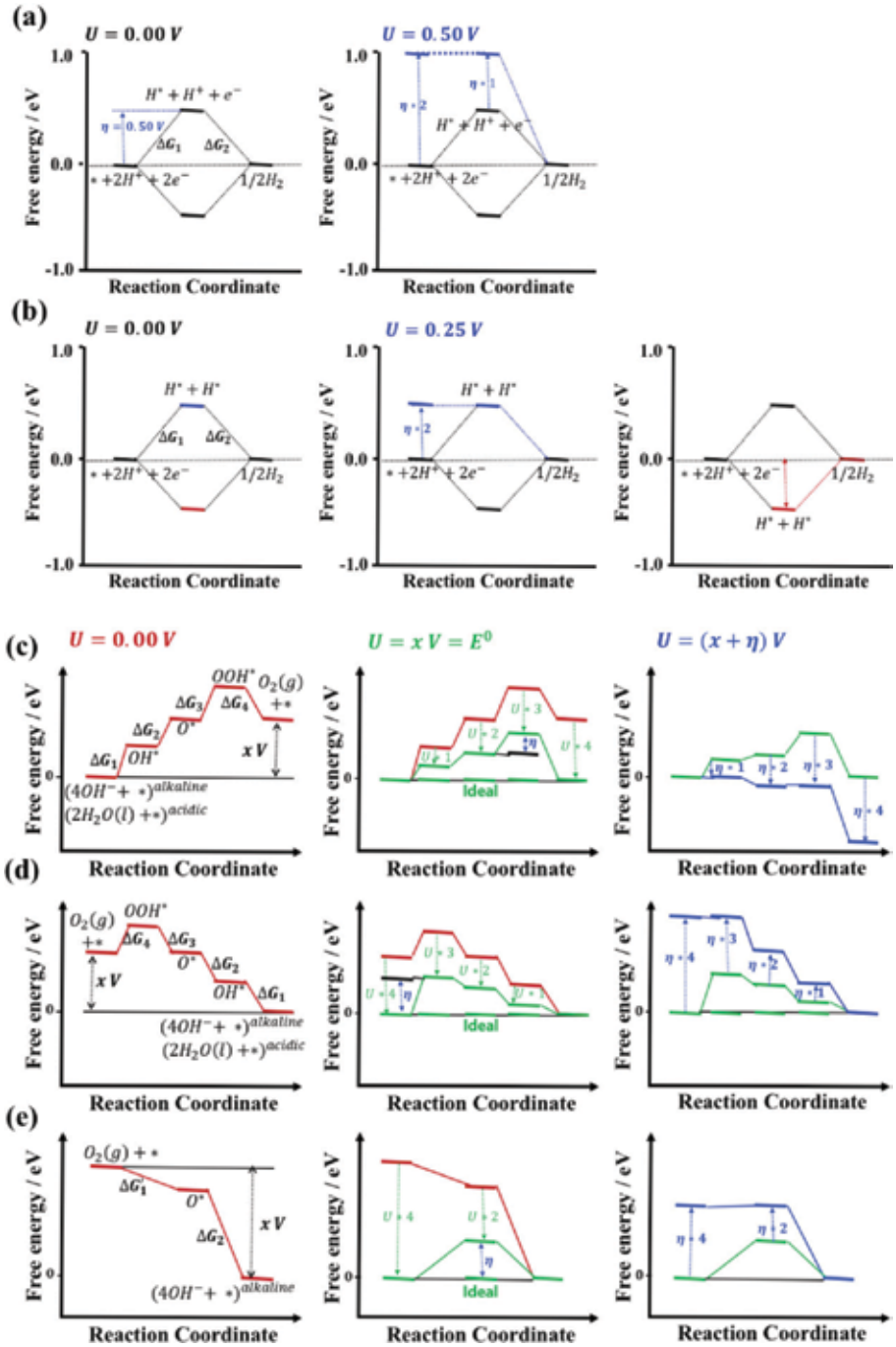

Figure 2. Free energy diagrams (FEDs) of (a) Volmer-Heyrovsky pathway and (b) Volmer-Tafel pathway for HER, and (c) four-step associative OER pathway, and (d) four-step ORR pathway in alkaline/acidic media, and (e) two-step ORR pathway in alkaline media at zero potential ($U = 0\ V$), at equilibrium reduction potential ($U = x\ V$) and at overpotential ($U = (x + \eta)\ V$). The x values indicate 0.402 V (alkaline) or 1.230 V (acidic).

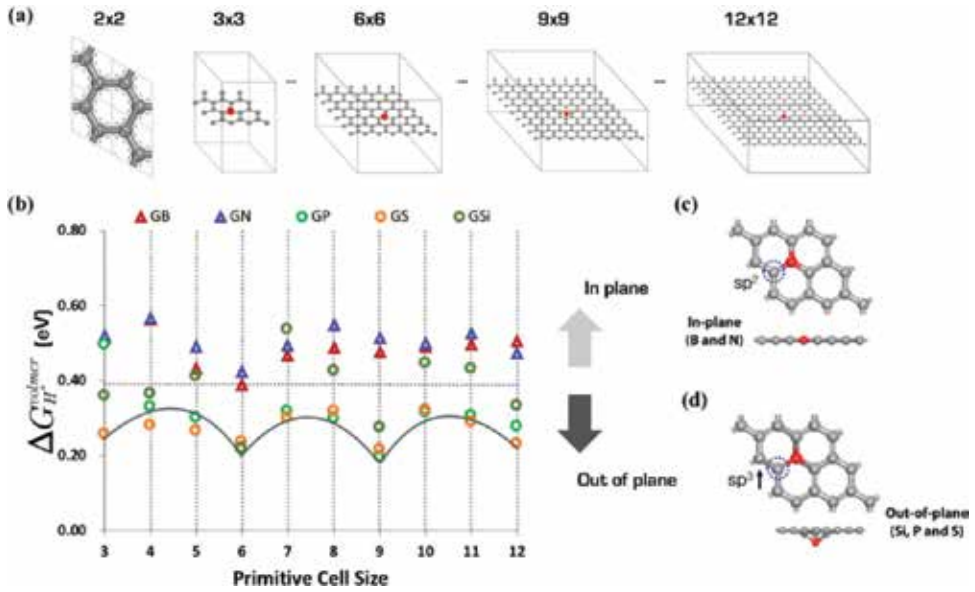

Figure 3. (a) Primitive cells of single heteroatom doped-graphene (GX, where G means graphene and X is B, N, Si, P, and S dopant) and (b) HER activities ΔG^{Volmer} of GX as a function of primitive cell size. Red mark indicates dopant. There are two different types of structures depending on dopant, (c) in-plane and (d) out-of-plane.

The theoretical overpotential at standard conditions is then given by (Eq. (76)) in acidic and alkaline conditions, respectively:

$$\eta^{HER} = \left(G^{HER}/e\right) - x\ V, \quad x = 0.000\ \ V \tag{76}$$

$$\eta^{OER/ORR} = \left(G^{OER/ORR}/e\right) - x\ V, \quad x = 1.230\ \ V\ (acidic),\ \text{and}\ 0.402\ \ V(alkaline) \tag{77}$$

In the case of HER pathways, the Volmer-Heyrovsky reaction is an electrochemical reaction involving electrons at all steps, as shown in **Figure 2(a)**. Therefore, when the external potential ($U = 0.50V$) is applied, the chemical potential of steps involving electrons shifts by the external potential ($U = 0.50V$), and the Volmer-Heyrovsky reaction changes from uphill to downhill reaction. In contrast to the Volmer-Heyrovsky reaction, the Volmer-Tafel reaction is an electrochemical reaction involving electrons only in the Volmer step, as shown in **Figure 2(b)**. Therefore, when the adsorption of hydrogen is unstable, the downhill reaction is possible by applying the external potential ($U = 0.25V$), but when the adsorption of hydrogen is stable, the reduction of H^+ is spontaneous reaction, and the desorption of H_2 in the Tafel step is the rate determining step. However, the desorption of H_2 is a thermodynamic reaction, which is not involved in electrons, not an electrochemical reaction. In the case of OER/ORR pathways, the theoretical overpotential ($\eta^{OEP/OPP}$) represents the relative stability of the intermediates between $(4OH^- + *)^{alkaline}$, $(2H_2O(l) + *)^{acidic}$ and $(O_2(g) + *)$, and vice versa, as shown in **Figure 2 (c)-(e)**. In addition, it can be calculated by applying standard density functional theory (DFT)

in combination with the computational standard hydrogen electrode (SHE) model. Because the equilibrium reduction potential is $U = 1.230\ V\ (acidic)$ and $0.402\ V(alkaline)$, the chemical potential difference between $(4OH^-)^{alkaline}$, $(2H_2O(l))^{acidic}$ and $O_2(g)$ should be 1.608 and 4.920 V, respectively. However, the actual catalytic behaviors deviate from the ideal case due to correlation with binding energies of the intermediates. Therefore, most catalysts require overpotential (η^{HER} and $\eta^{OER/ORR}$) in order to achieve an overall downhill reaction. Consequently, the η^{HER} and $\eta^{OER/ORR}$ the important indicators of catalytic activities of a catalyst, and the lower η^{HER} and $\eta^{OER/ORR}$ indicate a thermodynamically superior catalyst.

3. Structure-catalytic activity relationships

3.1. Heteroatom doped graphene (GX) for HER catalyst

Figure 3 shows a schematic of the heteroatom doped-graphene (GX, where G means graphene and X is B, N, Si, P, and S dopant) structures. We have used the second row elements (B and N) and the third row elements (Si, P, and S) in the periodic table in order to investigate the structural and electronic doping effects on HER activity because the third row elements are relatively larger than the second row elements and p- and n-type doping effects can be expected from the electron deficient B, and electron rich N, P, and S elements give in-plane and out-of-plane structures, respectively, due to the size of the dopants.

3.1.1. Structural and electronic doping effects on HER activity

On the atomic orbital hybridization characters of adjacent carbon atoms of dopant, the natural bond orbital (NBO) analysis show an increased p orbital contribution from sp^2 to sp^3 hybridization of carbons adjacent to the dopant due to structural deformation from in-plane to out-of-plane. Compared to sp^2-hybridized carbon, sp^3-hybridized carbons more readily form an extra a hydrogen atom without additional structural change. Therefore, in out-of-plane structures, the subsequent two hydrogen atoms prefer to bind to only sp^3 hybridized carbons adjacent to the dopant. However, in the case of in-plane structures having only sp^2-hybridized carbons, the first hydrogen atom should result in structural deformation to form sp^3-hybridized carbons. Therefore, the first hydrogen adsorption on the in-plane structure is less favorable than the reaction on out-of-plane structures. The second hydrogen atom can favorably bind to sp^3-hybridized second neighboring carbons of dopant. Consequently, structural deformation with dopants that are third row elements is associated with improved HER activity due to atomic orbital hybridization, as shown in **Figure 3(b)**. Looking at the electronic structures of GXs, p- and n-type doping effects are also expected from electron deficient and rich elements. In the case of in-plane GXs, electron deficient boron shifts its band structure up by withdrawing an electron from graphene, and electron rich nitrogen shifts its band structure down by donating an electron to graphene. Interestingly, in the case of out-of-plane GXs, electron rich phosphorous and sulfur dopant have no associated band shift. The origin of the flat band can be understood based on the localization of an extra electron onto the dopant site. In order to verify the relationship between geometric and electronic structures of GXs, we have

systematically changed the structures of GXs from in-plane to out-of-plane structures and vice versa. These calculations clearly show that dopant can produce n- and p-type doping states as well as a localized state depending on the structure of GXs induced by the type of dopants. When the out-of-plane (in-plane) deformation is applied in the in-plane (out-of-plane) GXs, band structures change from the p-type doping state (localized state) to the localized state (p-type doping state). Therefore, it is worth mentioning that the localized electronic states can be associated with physical regularity of HER activities on the out-of-plane GXs.

3.2. Heteroatom doped C_3N_4 (X_Y-C_3N_4) for OER/ORR bi-functional catalyst

In this work, we have systematically investigated a metal-free bifunctional electrocatalyst of heteroatom-doped carbon nitride (X_Y-C_3N_4, where X and Y indicate the dopant and doping site on C_3N_4, respectively) for oxygen evolution and oxygen reduction reactions (OER and ORR) in alkaline media, considering the possible reaction pathways based on the Eley-Rideal (ER) mechanism as well as the doping effects on electrocatalytic activity. Moreover, we determined that the relative stability of O^* and OOH^* intermediates was a key factor determining the ORR pathway; accordingly, ORR follows a two-step reaction pathway governed by O^* rather than a four-step reaction pathway governed by OOH^*. Firstly, we calculated relative E_f and the most stable structures of heteroatom-doped C_3N_4 structures, X_Y-C_3N_4, where X = P, S, or PS and Y = C or N [18, 20]. By considering the E_f (formation energy) results as well as the various doping sites, we determined the most stable X_Y-C_3N_4 structures, P_{CA}-C_3N_4, P_{NB}-C_3N_4, S_{CB}-C_3N_4, S_{NB}-C_3N_4, $P_{CA}S_{CB}$-C_3N_4, $P_{NA}S_{NB}$-C_3N_4, and $P_{CA}S_{NB}$-C_3N_4, for the investigation of OER/ORR bifunctional electrocatalytic activities and their reaction mechanisms in alkaline media.

3.2.1. OER and ORR catalytic activity on X_Y-C_3N_4

Figure 4 (a) and **(c)** show the volcano plot of OER and ORR in alkaline media at all possible active sites on X_Y-C_3N_4, which represents the apparent catalytic activity, respectively. This theoretical analysis reveals that the P_CS_C-C_3N_4 structure has minimum η^{OER} (0.42 V) and η^{ORR} (0.27 V). The $\eta^{OER/ORR}$ value of P_CS_C-C_3N_4 is comparable to those of the best conventional catalysts (∼0.42 V for OER on RuO_2 and ∼0.45 V for ORR on Pt). Most elementary steps in OER have an uphill reaction at 0.00 V and at equilibrium potential of 0.402 V. Analyzing the FED at the equilibrium potential of 0.402 V, we can define the rate determination step as the formation of OOH^* from O^* on P_CS_C-C_3N_4, as shown in **Figure 4 (b)**. Therefore, the ΔGat the rate determination step, 0.42 V, become the η^{OER} for facilitating the OER as a spontaneously downhill reaction. By applying the increased electrode potential of 0.82 V, all elementary reactions can be downhill reactions for spontaneous OER. In the case of the ORR, we considered the O_2 adsorption free energy (ΔG_{O2}*) and η^{ORR} are highly correlated to determine ORR activity. If the O_2 adsorption reaction is very difficult to achieve as an initiation step in ORR, that material cannot have ORR activity, even though it can have a possibility to have a very small η^{ORR}. Therefore, we defined a new indicator of ORR activity as figure of merit (FOM), which is defined by $FOM = -(\eta^{ORR} + \Delta G_{O2}^*)$. Using FOM, we constructed a volcano plot of ORR at all possible active sites on X_Y-C_3N_4 in order to compare the ORR catalytic activity, as shown in **Figure 4 (c)**, where the P_CS_C-C_3N_4 structure have minimum η^{ORR} of 0.27 V.

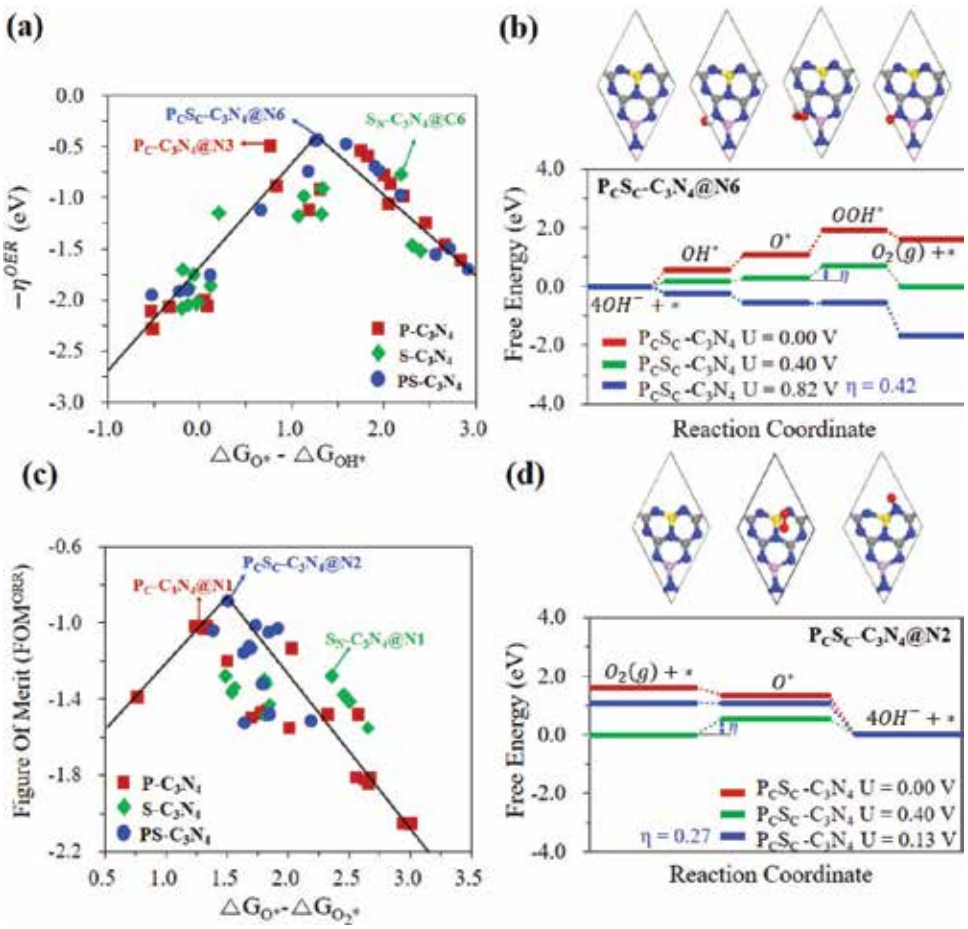

Figure 4. The volcano plots of (a) OER and (c) ORR at all possible active sites on X_Y-C_3N_4 and the free energy diagrams (FEDs) of P_CS_C-C_3N_4 structure having the best catalytic activity.

3.2.2. Structural and electronic doping effects on OER/ORR activity

The synergistic effect of P, S co-doping can be explained based on the geometric and electronic effects of heteroatoms [17–20]. Considering the atomic size of heteroatoms, the relatively larger S and P dopants can cause structural deformation of X_Y-C_3N_4, which improves the OER and ORR activity by enhancing the stability of intermediates with increasing p orbital character of active sites adjacent to the dopant from sp^2 to sp^3 hybridization. Compared to sp^2 hybridized orbitals on pure C_3N_4, sp^3 character of active sites on X_Y-C_3N_4 is more suitable for forming chemical bonds with intermediate species. Therefore, in out-of-plane structures, the intermediates prefer to bind to sp^3-hybridized active sites. Moreover, to verify the relationship between geometric and electronic structures of X_Y-C_3N_4, we intentionally changed the structures of X_Y-C_3N_4 from in-plane to out-of-plane to increase the activity for binding intermediate species by increasing the sp^3 character of active sites on X_Y-C_3N_4. We investigated density of state (DOS) of pure C_3N_4 and X_Y-C_3N_4 (X = P, S, or PS and Y = N) to determine at what condition the OER/ORR exhibit outstanding performance [18, 20]. It can be expected that

electron-rich heteroatom doping will induce electronic structure changes from a non-metallic doping effect to a metallic doping effect due to a downward band shift. As a result, P_CS_C-C_3N_4 shows the best OER/ORR activity by maintaining a metallic property despite the presence of out-of-plane deformation. Consequently, it can be emphasized that there is a close correlation between the electronic/geometric structure and OER/ORR catalytic activities, and the best bifunctional OER/ORR catalytic activity of P,S co-doped P_CS_C-C_3N_4 is attributed to a synergistic effect between the electronic and geometric effects.

4. Conclusion

We have systematically investigated the detailed mechanisms of HER/OER/ORR and the synergistic effect between geometric and electronic factors plays an important role in HER/OER/ORR catalytic activities of GXs and X_Y-C_3N_4. In this work, we demonstrated that the HER/OER/ORR activity of GXs and X_Y-C_3N_4 can be modulated by structural and electronic factors, including structural deformation with dopants. These structural and electronic factors enhance adsorbent binding strength during the reactions in HER/OER/ORR by generating sp^3-hybridized atoms and facilitating charge transfer between adsorbents and GXs/X_Y-C_3N_4 as metallic properties. Additionally, we re-evaluated the generally accepted ER mechanism of OER/ORR by comparing the stability of intermediates governing the reactions, where we found that the OER/ORR respectively follows four-step and two-step reaction pathway. We also elucidated the importance of the O_2 adsorption free energy (ΔG_{O2}*) in ORR activity. Considering the ΔG_{O2}* with a *FOM*, $FOM = -(\eta^{ORR} + \Delta G_{O2}*)$, we successfully represented the ORR activity of X_Y-C_3N_4. We believe that the understanding of the detailed mechanism as well as the relationship of structure-electrocatalytic activity of the HER/OER/ORR can facilitate development of new electrocatalytic materials.

Acknowledgements

This research was supported by grants from the Basic Science Research Program through the National Research Foundation of Korea (NRF) funded by the Ministry of Science, ICT, and Future Planning (NRF-2018R1A2B6006320). This work was also supported by the Supercomputing Center/Korea Institute of Science and Technology Information with supercomputing resources including technical support (KSC-2017-C3-0032).

Author details

Chi Ho Lee[1] and Sang Uck Lee[1,2]*

*Address all correspondence to: sulee@hanyang.ac.kr

1 Bionano Technology, Hanyang University, Ansan, Korea

2 Chemical and Molecular Engineering, Hanyang University, Ansan, Korea

References

[1] Jiao Y, Zheng Y, Jaroniecb M, Qiao SZ. Chemical Society Reviews. 2015;**44**:2060-2086. DOI: 10.1039/c4cs00470a

[2] Chuangang H, Dai L. Angewandte Chemie, International Edition. 2016;**55**:11736-11758. DOI: 10.1002/anie.201509982

[3] Shinagawa T, Garcia-Esparza AT, Takanabe K. Scientific Reports. **5**:13801. DOI: 10.1038/srep13801

[4] Yi C, Jiang SP. Progress in Natural Science: Materials International. 2015;**25**:545-553. DOI: 10.1016/j.pnsc.2015.11.008

[5] Li J, Zheng G. Advancement of Science. 2017;**4**:1600380. DOI: 10.1002/advs.201600380

[6] Zhang P, Xiao BB, Hou XL, Zhu YF, Jiang Q. Scientific Reports. 2014;**4**:3821. DOI: 10.1038/srep03821

[7] Keith JA, Jerkiewicz G, Jacob T. Chemphyschem. 2010;**11**(13):2779-2794. DOI: 10.1002/cphc.201000286

[8] Dai L, Xue Y, Qu L, Choi HJ, Baek JB. Chemical Reviews. 2015;**115**(11):4823-4892. DOI: 10.1021/cr5003563

[9] Fabbri E, Habereder A, Waltar K, Kotz R. Catalysis Science & Technology. 2014;**4**(11):3800-3821. DOI: 10.1039/C4CY00669K

[10] Reier T, Oezaslan M, Strasser P. ACS Catalysis. 2012;**2**(8):1765-1772. DOI: 10.1021/cs3003098

[11] Lim DH, Wilcox J. Journal of Physical Chemistry C. 2012;**116**(5):3653-3660. DOI: 10.1021/jp210796e

[12] Li YF, Li M, Jiang LQ, Lin L, Cui LL, He XQ. Physical Chemistry Chemical Physics. 2014;**16**(42):23196-23205. DOI: 10.1039/C4CP02528H

[13] Sidik RA, Anderson AB, Subramanian NP, Kumaraguru SP, Popov BN. The Journal of Physical Chemistry. B. 2006;**110**(4):1787-1793. DOI: 10.1021/jp055150g

[14] Gong KP, Du F, Xia ZH, Durstock M, Dai LM. Science. 2009;**323**(5915):760-764. DOI: 10.1126/science.1168049

[15] Yang LJ, Jiang SJ, Zhao Y, Zhu L, Chen S, Wang XZ, Wu Q, Ma J, Ma YW, Hu Z. Angewantde Chemie International Edition. 2011;**50**(31):7132-7135. DOI: 10.1002/anie.201101287

[16] Li MT, Zhang LP, Xu Q, Niu JB, Xia ZH. Journal of Catalysis. 2014;**314**:66-72. DOI: 10.1016/j.jcat.2014.03.011

[17] Lee CH, Jun B, Lee SU. RSC Advances. 2017;**7**(43):27033-27039. DOI: 10.1039/C7RA04115B

[18] Shinde SS, Lee CH, Sami A, Kim DH, Lee SU, Lee JH. ACS Nano. 2017;**11**:347-357. DOI: 10.1021/acsnano.6b05914

[19] Shinde SS, Lee CH, Yu JY, Kim DH, Lee SU, Lee JH. ACS Nano. 2018;**12**:596-608. DOI: 10.1021/acsnano.7b07473

[20] Lee CH, Jun B, Lee SU. ACS Sustainable Chemistry & Engineering. 2018;**6**:4973-4980. DOI: 10.1021/acssuschemeng.7b04608

[21] Norskov JK, Bligaard T, Logadottir A, Kitchin JR, Chen JG, Pandelov S, Stimming U. Journal of the Electrochemical Society. 2005;**152**:J23-J26. DOI: 10.1149/1.1856988

Chapter 2

Oxygen Reduction Reaction

Lindiwe Khotseng

Additional information is available at the end of the chapter

http://dx.doi.org/10.5772/intechopen.79098

Abstract

In this chapter, the oxygen reduction reaction (ORR), which is one of the most important reactions in energy conversion systems such as fuel cells, including its reaction kinetics, is presented. Recent developments in electrocatalysts for ORR in fuel cells, including low and non-Pt electrocatalysts, metal oxides, transition metal macrocycles and chalgogenides, are discussed. Understanding of the interdependence of size, shape and activity of the electrocatalysts is evaluated. The recent development of ORR electrocatalysts with novel nanostructures is also reported. The mechanism catalysed by these electrocatalysts is presented. Finally, the perspectives of future trends for ORR are discussed.

Keywords: oxygen reduction reaction, electrocatalysts, reaction kinetics, mechanism, novel nanostructures, polymer membrane fuel cells

1. Introduction

Oxygen reduction reaction (ORR) has been the subject of extensive investigation over the last century [1]. This is largely because ORR is of major importance to energy conversion, in particular in the field of fuel cells and metal-air batteries [1–3]. ORR is the most important cathodic process in polymer electrolyte membrane fuel cells (PEMFCs) [4]. Among all catalysts evaluated, Pt is still the best catalyst for ORR. The major obstacle with Pt is that it belongs to the platinum group of metals, which are rare metals, hence too expensive for feasible commercialisation of fuel cells. This has led to more research being conducted in an effort to find alternate electrocatalysts that can be used.

Oxygen reduction in aqueous solutions occurs mainly through two different pathways: either a four-electron reduction pathway from O_2 to H_2O or a two-electron pathway from O_2 to H_2O_2. The most accepted mechanism of ORR was first proposed by Damjanovic et al. [5, 6]

and later modified by Wroblowa et al. [7], making it easier to understand the complicated reaction pathway of oxygen on the metal surface. They suggest that ORR proceeds along two parallel reaction pathways with rates that are comparable. In PEMFCs, a four-electron transfer is preferred.

The ORR is alkaline media versus reversible hydrogen electrode (RHE) at 25°, and its thermodynamic potentials at standard conditions are presented as follows [3, 8, 9]:

$$O_2 + 2H_2O + 4e^- \rightarrow 4OH^- \quad E^\circ = 0.401 \ V \tag{1}$$

The pathway involving the hydrogen peroxide is expressed as follows [10]:

$$O_2 + H_2O + 2e^- \rightarrow HO_2^- + OH^- \quad E^\circ = 0.080 \ V \tag{2}$$

$$HO_2^- + H_2O + 2e^- \rightarrow 3OH^- \quad E^\circ = 0.880 \ V \tag{3}$$

The ORR is acidic media versus RHE at 25°, and its thermodynamic potentials at standard conditions are presented as follows:

Direct four-electron reduction:

$$O_2 + 4H^+ + 4e^- \rightarrow 2H_2O \quad E^\circ = 1.230 \ V \tag{4}$$

Indirect reduction:

$$O_2 + 2H^+ + 2e^- \rightarrow H_2O_2 \quad E^\circ = 0.680 \ V \tag{5}$$

$$H_2O_2 + 2H^+ + 2e^- \rightarrow 2H_2O \quad E^\circ = 1.776 \ V \tag{6a}$$

Or chemical decomposition:

$$2H_2O_2 \rightarrow 2H_2O + O_2 \quad E^\circ = 1.776 \ V \tag{6b}$$

2. Kinetics of ORR

It is desirable for the ORR to occur at potentials close to thermodynamic potentials as much as possible. For the thermodynamic potentials to be obtained, the charge transfer kinetics of the ORR must be quick. It has been reported that the kinetics of fuel cells at cathode are slow, hence show over-potential η as in Eq. (7) [3, 11]:

$$\eta = E - E_{eq} \tag{7}$$

E is the resultant potential and E_{eq} is the equilibrium potential.

http://dx.doi.org/10.5772/intechopen.79098

The difference between E and E_{eq} is called polarisation.

There are three distinct types of polarisation expressed in Eq. (8):

$$\eta = \eta_{act} + \eta_{conc} + iR \tag{8}$$

η_{act} is the activation over-potential, a function describing the charge transfer kinetics of an electrochemical reaction. η_{act} is always present and mostly dominant at small polarisation currents.

η_{conc} is the concentration over-potential, a function describing the mass transport limitations associated with electrochemical processes. η_{conc} is predominant at larger polarisation currents.

iR is the ohmic drop. This function takes into account the electrolytic resistivity of an environment when the anodic and cathodic elements of a corrosion reaction are separated by this environment while still electrically coupled.

The graph in **Figure 1** depicts a polarisation curve showing the electrochemical efficiency of a fuel cell.

The expression relating the over-potential, η, and the net current is known as the Butler-Volmer equation and is given as follows [13]:

$$i = i_o \left\{ \exp\left(\beta \frac{nF}{RT} \eta\right) - \exp\left(-[1-\beta] \frac{nF}{RT} \eta\right) \right\} \tag{9}$$

where i is the ORR current density, i_o is the exchange current density, n is the number of electrons transferred in the rate-determining step, β is the transfer coefficient, β is the

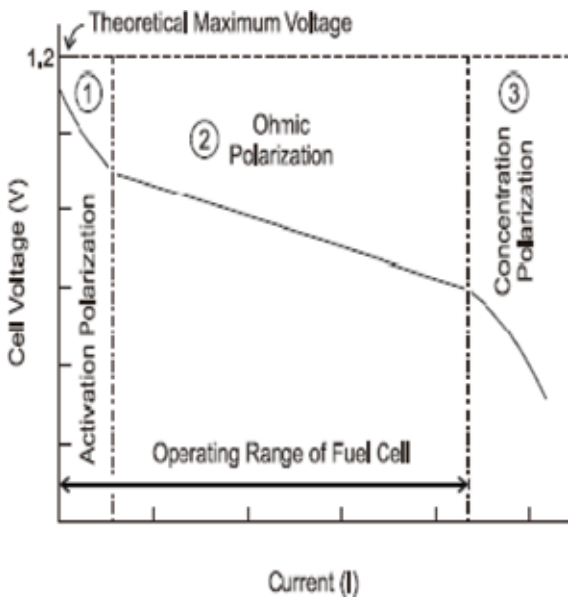

Figure 1. The polarisation curve shows the electrochemical efficiency of the PEMFC at any operating current [12].

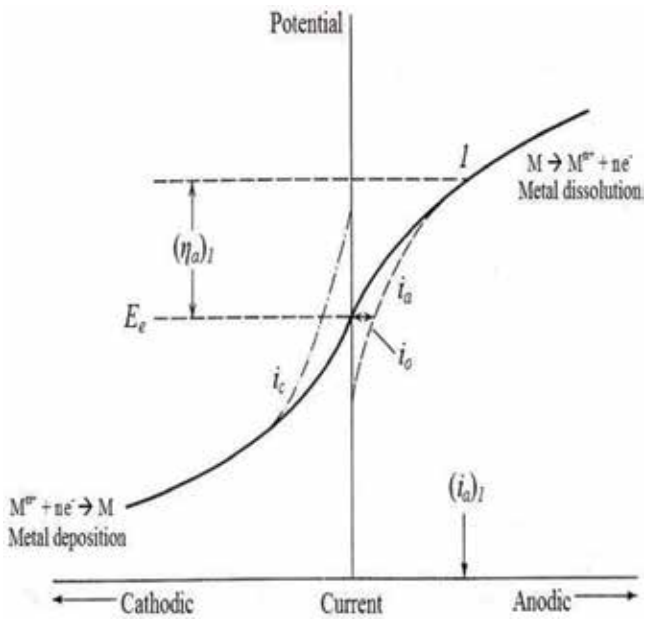

Figure 2. Current-potential relationship of a metal dissolution ($M \rightarrow M^{n+}$)/deposition ($M^{n+} \rightarrow M$) process [13].

over-potential of ORR, *F* is the Faraday constant, *R* is the gas constant and *T* is the temperature in K. The first term in the Butler-Volmer equation represents the anodic reaction/metal dissolution, while the second term represents the cathodic reaction/metal deposition. A plot of the Butler-Volmer equation gives the polarisation curve as shown in **Figure 2**.

There are two limitations in the Butler-Volmer equation.

1. A low over-potential region, also known as polarisation resistance/charge transfer resistance, where the Butler-Volmer equation simplifies to [13]

$$i = i_c = i_o \exp\left\{(1-\beta)\frac{nF}{RT}\eta\right\} \tag{10}$$

$$\eta_c = b_c \log\left(\frac{ic}{io}\right) \tag{11}$$

$$b_c = -2.303\ \frac{RT}{(1-\beta)nF} \tag{12}$$

2. At high over-potentials region, the Butler-Volmer equation simplifies to Tafel equation

$$i_a = i_o \exp\left(\beta\frac{nF}{RT}\eta\right) \tag{13}$$

$$\eta_a = b_a \log\left(\frac{ia}{io}\right) \tag{14}$$

$$b_a = 2.303\ \frac{RT}{\beta nF} \tag{15}$$

A plot of η versus log i_c also known as the Tafel plot and gives a linear relationship, with slope $2.303\frac{RT}{\beta nF}$, known as the Tafel slope and the intercept yielding the i_o. The Tafel slope gives the information about the mechanism of the ORR. The higher the Tafel slope, the faster the over-potential increases with current density. With a low Tafel slope, the electrochemical reaction is able to obtain a high current density, at low over-potential. For ORR, two Tafel slopes, 60 mV dec^{-1} and 120 mV dec^{-1}, respectively, are obtained, depending on the potential range and the electrode material used.

3. Electrocatalysts for ORR

The kinetics of the ORR at the cathode are very important, as they are the factors for the performance of PEMFCs [14, 15]. There are several issues that need to be addressed, including slow reaction kinetics at the cathode, which are due to highly irreversible ORR, and fuel crossover in the cathode, which causes a mixed potential, leading to potential loss and 25% reduction in efficiency, hence reducing the ORR performance [16–19]. An electrocatalyst is used to induce a four-electron reduction of O_2 to water by utilising the protons that permeate from the anode. Pt is the electrocatalyst that is currently used for ORR reactions, as it is the only commercially available catalyst with sensible activity and stability for PEMFCs, although it offers limited commercialisation of fuel cells due to its limited availability and high cost [4, 20]. It is also reported that Pt still shows over-potentials of over 400 mV from the equilibrium reversible potentials (1.19 V at 80°C) [21]. These high potentials result in the formation of adsorbed species on a platinum surface that restrain the ORR and hence result in performance loss [2]. Considerable research has been conducted to try to (1) reduce the costs of fuel cells, which is one of the stumbling blocks in fuel cell commercialisation using low-cost non-Pt catalysts such as supported platinum group metals Pd, Ir and Ru; (2) improve the electrocatalytic activity of the cathode catalyst, which includes using bimetallic alloy catalysts, transition metal macrocyanides, transition metal chalcogenides and metal oxides in order to improve the ORR kinetics on the new catalyst; and (3) fabricate Pt with novel nanostructures such as nanotubes, graphene and carbon nanofibres (CNFs), as it is known that supports may significantly affect the performance of the catalyst. However, these efforts are still in the research stage, as their activity and stability are still lower than that of the Pt catalyst.

3.1. Single-metal catalyst

Other noble metals, such as Pd, Ag, Rh, Ir and Ru, have also been used as cathode materials for ORR [22]. Among these, Pd, which has the same electron configuration and lattice constant as Pt, as they belong to the same row in the periodic table, showed the most improved ORR towards alcohol in an alkaline medium, while it is reported to be inactive in an acid medium [4, 23]. It has been showed that Pd/C is less sensitive to alcohol contamination compared to Pt/C, hence more tolerant to alcohol crossover [16, 24, 25]. However, when comparing the ORR activity of Pd/C to Pt/C, the former has less activity and high potentials of amount 0.8 V versus NHE, hence less stability, which prevents its replacement as the preferred ORR catalyst over Pt/C [26]. The noble metals in terms of ORR activity follow the trend: Pt > Pd > Ir > Rh [27]. Wang [18] reports that Ru can undergo a four-electron reduction reaction. Ag is reported

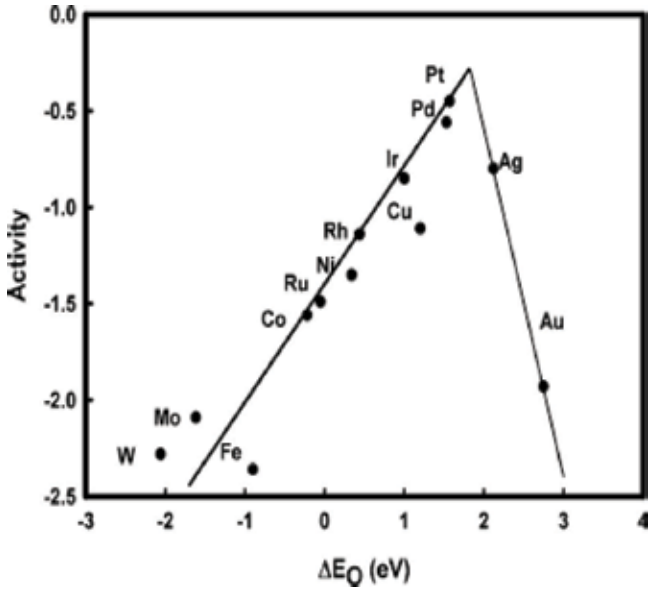

Figure 3. Oxygen reduction activities as a function of oxygen-binding energy [27].

to show less electrocatalytic activity towards ORR compared to Pt, but is more stable than Pt cathodes during long-term operations [4].

There are several metals other than noble metals that were also evaluated as cathode catalysts for ORR. **Figure 3** shows a comparison of the activities of various catalysts as a function of binding energy. These catalysts showed less catalytic activity towards ORR compared to Pt, with less electrochemical stability [28].

3.2. Bimetallic-alloyed catalysts

Transition metals such as Fe, Ni, Co and Cr have been extensively studied due to their improved ORR electrocatalytic activity as alloys for Pt in the presence of a support [17, 28]. Yuan et al. [17] prepared PtFe/C using the impregnation method. Current densities of PtFe/C for ORR in methanol were higher (78.6 mA cm^{-2}) than in Pt/C (65.0 mA cm^{-2}), but was lower in methanol-free solutions, indicating that PtFe/C is a better methanol-tolerant catalyst compared to Pt/C. In terms of power density, the PtFe/C showed an improvement of 20–30% compared to Pt/C [17]. Other researchers [29, 30] also reported better performance of PtFe/C for ORR. Yang et al. [31] report on PtNi/C prepared via the carbonyl complex route an improved mass and specific activity of PtNi/C compared to Pt/C with an improved electrocatalytic activity towards ORR. Pt-Bi/C showed improved methanol tolerance for ORR compared to Pt/C [3]. Remona and Phani [32] synthesised PtBi/C by micro-emulsion. The PtBi/C displayed a higher methanol tolerance compared to mass activity (1.5 times higher) for ORR compared to Pt/C. The high ORR activity of PtBi/C was due to distortion (internal stress) of three Pt sites by Bi.

The effect of Pd on Pt catalysts has been reported by various researchers [33–36], who all reported an improved electrocatalytic activity towards ORR. The improved electrocatalytic activity of Pt alloys has been ascribed to geometric effect, namely a decreased Pt-Pt bond distance, the dissolution of more oxidisable alloying components, a change in surface structure and electronic effect, that is, an increase in Pt d-band vacancy [31, 37]. Other noble metals (Au, Ir, Rh and Ru) were also studied as Pt alloys. PtAu/CNT (carbon nanotubes) was reported to show an improved electrocatalytic activity in an alkaline membrane compared to Pt/CNT [38–40]. Pd-Pt alloy had the highest electrocatalytic activity towards ORR compared to other Pt-alloyed noble metals. Fu et al. [41] report on an improved ORR electrocatalytic activity and a larger diffusion-limiting current density compared to commercial Pd black. The improvement of Pt with noble metals (Pd, Ag and Au) is attributed to these metals having a fully occupied d-orbital. The d-orbital coupling effect between metals decreases the Gibbs free energy for the electron-free steps in ORR, resulting in improved ORR kinetics [37].

Binary Pd catalysts (Cu, Ni, Fe, Co, W and Mo) have been identified as promising cathode catalysts for ORR with an improved electrocatalytic activity and stability compared to Pd alone due to changes in Pd-Pd bond length, modification of the electron configuration and change of surface species and compositions [4, 25]. Kim et al. [42] used PdSn/C as a cathode for direct methanol fuel cells. Their results exhibited a high performance in high methanol concentrations compared to commercial Pt/C. Wang [18] reports on PdCo catalysts tested for ORR. The results showed improved activities towards ORR, with PdCo improvement only observed when less than 20% Co was used. Meng et al. [4] report on PdFe, PdCu, PdAg and PdCo, which all showed an improved electrocatalytic activity compared to Pd alone. In the presence of alcohol, the binary Pd catalysts showed an improved electrocatalytic performance for ORR compared to Pt.

Although bimetallic catalysts (Pt with Fe, Ni, Co, etc.) have shown improvement in the performance of the ORR compared to Pt [27], the lack of preparation methods to control large synthesis has limited its use in commercial devices [33]. In addition, the dissolution of transition metals alloyed in the Pt-M catalyst is a major drawback, because these transition metals are electrochemically soluble at a potential range between 0.3 and 1.0 V versus NHE in acidic media [43].

One possible way to overcome the dissolution of transition metals and improve stability of catalysts is by preparing multi-component catalysts (three and more electrocatalyst alloys). The multi-component catalysts are able to shift the d-band centre by a strain effect (caused by the lattice mismatch in the multi-component system) and lower the adsorption energy of surface oxygenated intermediates, thereby enhancing the surface catalytic activity.

Tiwari et al. [37] report on various multi-component catalysts that have been synthesised over the years with either Pt or Pd, including PtTiM (M = Co, Cr, Cu, Fe, Mn, Mo, Ni, Pd, Ta, V, W and Za), PtCuCo, $PtCoSe_2$, PtIrCo, PdFePt, PtCuCoNi, PdSnPt and PdCoPt. From the multi-component catalysts, they reported an improved electrocatalytic activity towards ORR compared to pure Pt and the possibility of reducing the costs of the electrocatalysts for PEMFCs.

More research is also done on trying to improve the kinetics of Pt catalysts through the development of new and the optimisation of existing synthesis methods that can control the shape and surface structure of the electrocatalyst in order to improve its performance [8, 33, 44, 45]. There has been contracting reports on particle size and specific activity. Some researchers report a decrease in specific activity with a decrease in particle size, while other researchers report an increase in specific activity with a decrease in particle size. The discrepancy may be the result of different electrocatalysts with different shapes and degree of agglomeration [46]. It has been reported that metallic nanostructures with different shapes display unique chemical and physical properties [47]. Significant progress has been made for size-controlled spherical nanostructures, but only limited progress has been made with non-spherical nanostructures, which are reported to show more improved ORR electrocatalytic activity for fuel cells compared to spherical-shaped electrocatalysts, the reason being that the highly symmetric face-centred cubic crystal structure of Pt-based catalysts makes it not easy to obtain a non-spherical shape, which involves a competition over the desire to minimise the surface energy through the formation of thermodynamically stable spherical shapes. Hao et al. [48] report that cubic Pd nanocrystals exhibit better performance in methanol compared to the spherical Pd catalyst of a similar size. The improvement was attributed to cubic nanocrystals that contain a more electroactive surface area compared to its spherical counterpart. It has also been reported that Pt electrocatalysts with a tetrahedral shape showed much improved reaction kinetics compared to the spherical Pt nanoparticles. It has been reported that low-index crystal planes give poor electrocatalytic properties, while high-index planes give a high electrocatalytic activity and stability [47, 49]. Pt nanocubes have been reported to have much improved specific activity for ORR compared to commercial Pt catalysts (spherical) [47, 50]. Kuai et al. [50] report on uniform, high-yield icosahedral Ag and Au nanoparticles prepared using a hydrothermal system in the presence of polyvinylpyrrolidone and ammonia. The prepared Au and Ag nanoparticles showed an improved ORR electrocatalytic activity and excellent stability compared to spherical Pt/C nanoparticles.

The form or shape of the electrocatalysts depends on the synthesis method and the various parameters used. **Figure 4** shows the formation of various forms of Pt nanocubes using different strategies based on the polyol method [47]. The formation of Pt tubes can be obtained through two different routes, either galvanic displacement or using selected templates [47]. Researchers have synthesised metal nanoparticles with various shapes [32].

Researchers are reporting an improved electrocatalytic activity of ORR using various synthesis methods focusing on surface structure. Lim et al. [14] report on the synthesis of Pt/C using the modified polyol method using ethylene glycol as the reducing agent. The prepared catalyst had the highest mass activity, which was 1.7 times higher than the commercial Pt/C [14]. The improvement was attributed to small and uniform particle size and better dispersion. Adonisi et al. [51] report on various Pt-based catalysts synthesised using the Bonnemann method. Some of those catalysts showed an improved ORR electrocatalytic activity compared to commercial Pt/C. **Figure 5** shows a graph depicting 20% Pt/C commercial compared to 20% Pt/C synthesised catalysts using the Bonnemann method. From the graph, it can be observed that the 20% Pt/C commercial catalyst was found at lower current densities than the prepared 20% Pt/C catalyst. The mass activities of the 20% Pt/C commercial and 20% Pt/C prepared catalysts were found to be 12.6 and 15.8 A/g, respectively, and the specific activities were

http://dx.doi.org/10.5772/intechopen.79098

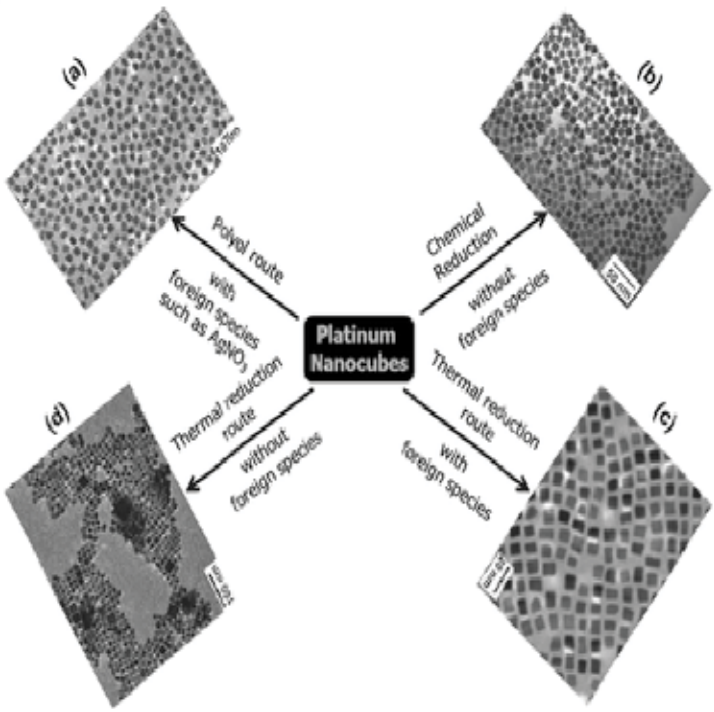

Figure 4. Different routes for the synthesis of Pt nanocubes along with their electron micrographs [47].

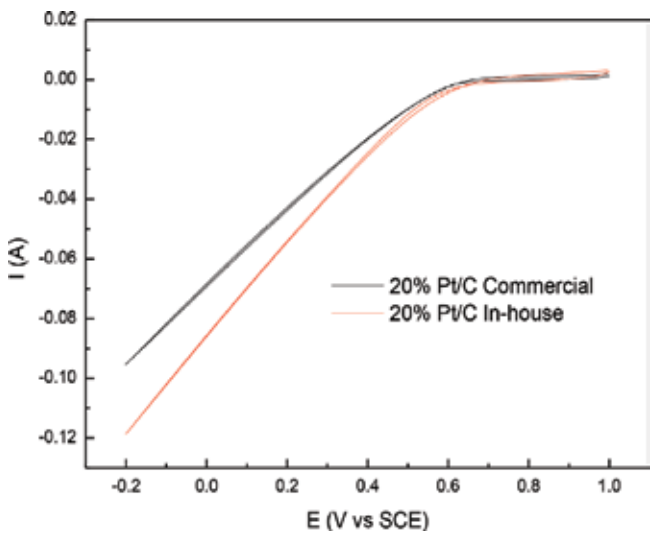

Figure 5. Cyclic voltammograms for ORR of 20% Pt/C commercial and prepared electrocatalysts in O_2-saturated 0.5 M H2SO4 at a scan rate of 20 mV [51].

found to be 0.060 and 0.063 A cm^{-2}, respectively. This improvement was attributed to the particle size of the prepared catalysts, which was smaller than the particle size for the commercial Pt/C catalyst.

Post-treatment after synthesis has been reported to change the physicochemical properties of the electrocatalysts. Heat treatment is considered as one of the important and sometimes necessary steps to improve the activity of the catalysts [52]. Heat treatment involves heating the catalyst under inert (N_2, Ar or He) or reducing H_2 atmosphere in the temperature range of 80–900°C for 1–4 h [52]. The benefit of heat treatment is the removal of impurities resulting from the preparation stages, allowing uniform dispersion and stable distribution of the catalyst on the support, thereby improving the electrocatalytic activity of the prepared catalyst. It has been determined that the electrocatalytic reduction of oxygen on the catalyst can be influenced by the particle size and surface structure, and hence treatment can have an effect on ORR activity and stability by altering the surface structure of the catalyst [32]. Various researchers have worked on heat treatment of mono and bimetallic catalysts for ORR [50]. They all concluded that heat treatment improves alloying of the catalysts, which decreases the Pt-Pt distance and hence d-band vacancy of the Pt and thus improves the electroactivity of the catalyst [53]. Jeyabharathi et al. [54] report on improved methanol tolerance of PtSn/C after heat treatment, while the ORR activity remained intact. Sarkar et al. report on PdW synthesised using thermal composition followed by annealing at 800°C with an improved electrocatalytic activity for ORR and catalyst durability with an improved methanol tolerance compared to Pt [32].

3.3. Transition metal macrocycles and chalgogenides

Transition metals such as macrocycles and chalgogenides have been used as ORR catalysts since the 1960s due to their inactivity towards the oxidation of methanol [55]. Other than noble metals, they are the most-studied electrocatalysts for oxygen reduction. The study of ruthenium chalgogenides Ru_xSe_y and Pt for ORR has shown that the performance of Ru_xSe_y is slightly weaker than Pt and that the difference was their behaviour in the presence or absence of methanol. Under these conditions, the electroactivity of Ru_xSe_y is not changed, while for Pt, the potential shifts to the negative direction (120–150 mV). A similar behaviour was observed when Ru_xSe_y was embedded in a polymetric matrix, such as polyaniline. RuSM (M = Rh, Re, Mo, etc.) when used as catalysts, methanol oxidation on the cathode was suppressed or avoided leading to a reduced mixed potential. The results confirm that the chalgogenide of Ru is insensitive to methanol, in contrast to the Pt catalyst [56]. The main concern with this approach was the low power output due to low activity of these catalysts for ORR, compared to the Pt catalyst [17]. Cobalt and iron phthalocyanide are the most-studied transition metals as centres for macrocycling rings as catalysts for ORR in fuel cells [56, 57]. These ORR catalysts have shown that a number of metal chelates will chemisorb oxygen [58]. A fuel cell with an iron phthalocyanide cathode can only be stable for up to 10 h [17], but has shown improved activity towards ORR in alkaline media [44]. Zagal et al. [59] report that when Fe chelates with N_4, a four-electron ORR occurs. Co phthalocyanide has demonstrated similar ORR kinetics as commercial Pt/C, as it also leads to a four-electron process per oxygen molecule, that is, to water, but at lower potentials (0.25 and −0.25 versus RHE) [44, 56]. However, these compounds are not completely stable under strong acid conditions [17, 56]. They decompose via hydrolysis in the electrolyte and attack the macrocyanide via peroxide, causing poor performance and stability [58, 60, 61]. Transition metal chalgogenides are more stable and show an improved electrocatalytic activity at temperatures above 800°C.

3.4. Metal oxides

Another route to stabilising nanoparticles is the development of metal oxide composite supports. Metal oxides such as IrO_2, NiO, CeO_2, ZrO_2, TiO_2 and SnO_2 have also been studied as ORR catalysts in basic acidic media [62–66]. Nanoparticles on metal oxides are not able to improve the electrocatalytic activity due to their limited electron conductivity, but are reported to have excellent corrosion resistance in various electrolyte media [66, 67]. Researchers use metal oxides in combination with carbon supports that have desirable properties such as a high surface area and a high electric conductivity. The metal oxides combined with carbon supports are reported to improve the stability and the electrocatalytic activity of the electrode material. Carbon surfaces are functionalised before they are used as supports for catalysts in order to improve their surface properties, but the disadvantage of functionalisation is that it accelerates the degradation process of the support material. The presence of the metal oxide delays the corrosion process. Montero-Ocampo et al. [68] report on $PtTiO_2$ and $PtTiO_2$/CNT synthesised using metal organic chemical vapour deposition. The $PtTiO_2$/CNT was more electrocatalytically active compared to $PtTiO_2$, while good stability was observed for both $PtTiO_2$ and $PtTiO_2$/CNT that was provided by the TiO_2 support. This was attributed to the high conductivity of CNT compared to TiO_2, which has limited electron conductivity. Pt/TiO_2/C showed improvement in activity and thermal stability for ORR compared to Pt/C [69]. Khotseng et al. [70] compared the activity for PtRu/TiO_2 to commercial PtRu/C and Pt/C. They reported a high electroactive surface area and activity of commercial Pt/C and PtRu/C compared to PtRu/TiO_2 towards ORR. When durability studies were performed for the same catalysts, the PtRu/TiO_2 recorded a loss of 29% compared to Pt/C and PtRu/C, which recorded a loss of 64 and 32%, respectively. Li et al. [71] reported an improved oxygen reduction activity, a better durability and a higher methanol tolerance capability in alkaline solution compared to Pt/C.

Most metal oxides were found to be unstable in acidic media. To overcome this instability, conducting polymer polypyrrole (Ppy) was used against the dissolution of metal oxides. During synthesis, the metal oxides were sandwiched between the Ppy layers. Through this research, an improved electrochemical stability of the metal oxides was achieved [18]. Singh et al. [72] report on $CoFe_2O_4$ oxides sandwiched between Ppy layers. A high electrocatalytic activity towards ORR at high cathodic potentials was obtained with stability in acidic media [72].

3.5. Novel nanostructures with electrocatalysts

Although Pt-based catalysts have been widely studied due to their high current density and low over-potential, when used as cathode catalysts, their activity is lowered due to slow reaction kinetics. More research is required to try to improve the catalyst activity. One of the focus areas is looking into loading Pt nanostructures with a high activity on the surface of supporting materials with (1) low cost, (2) good electrical conductivity, (3) strong catalyst-support interaction that is influenced by its surface functionalities to limit the possible deactivation of the electrocatalyst and allow for efficient charge transport, (4) large surface area and (5) good resistance to corrosion to allow high stability [8, 22, 24, 73–75]. Carbon black (CB) is the most-used support for Pt and Pt alloy catalysts. CB is thermochemically unstable and hence suffers from corrosion, leading to performance degradation and durability issues and high potential

[66, 76]. Nanostructured carbon materials, for example, mesoporous carbon, CNFs, CNTs and graphene, have been studied extensively as support materials for electrocatalysts, as they have been identified as some of the most promising materials for PEMFCs due to their high chemical stabilities, high electric conductivities and improved mass transport capabilities [32, 77].

CNTs are attractive support materials in fuel cell applications and are by far the most-explored carbon nanostructures as catalyst supports in fuel cells due to their excellent mechanical strength, a high surface area and a high electric conductivity and because they have reported to show an improved catalytic activity [22, 32, 78] compared to CB. The carbon surface is functionalised to provide oxygen-binding groups for the growth of metal catalyst ions [79]. CNTs can be single-walled (SWCNT) or multi-walled (MWCNT), depending on the structure. Both SWCNT and MWCNT have been used as support materials to disperse the electrocatalyst and have been reported to show an enhanced electrocatalytic activity towards ORR. SWCNTs have unique electrical and electronic properties, a wide electrochemical stability and high surface areas [9]. When compared to commercial Pt/C (from ETEK) in acidic media, the SWCNT showed an improved electrocatalytic activity performance, with the negative shift of onset potential by 10 mV compared to Pt/C, whose onset potential moved to a higher potential by 15 mV [15, 73]. Jukk et al. [80] report on Pd/MWCNT having an enhanced electrocatalytic activity compared to Pd/C for ORR. Wang et al. [81] reported on Pt/MWCNT, which showed an improved electrocatalytic activity for ORR compared to Pt/C. Khotseng et al. [70] compared PtRu/MWCNT with commercial Pt/C, PtRu/C and prepared PtRu/TiO_2 and PtRu/MoO_2. From **Figure 6** and **Table 1**, it is observed that PtRu/MWCNT has the highest mass and specific activity at 0.9 V compared to commercial Pt/C, PtRu/C and prepared PtRu/TiO_2 PtRu/MoO_2 with the highest current density towards ORR.

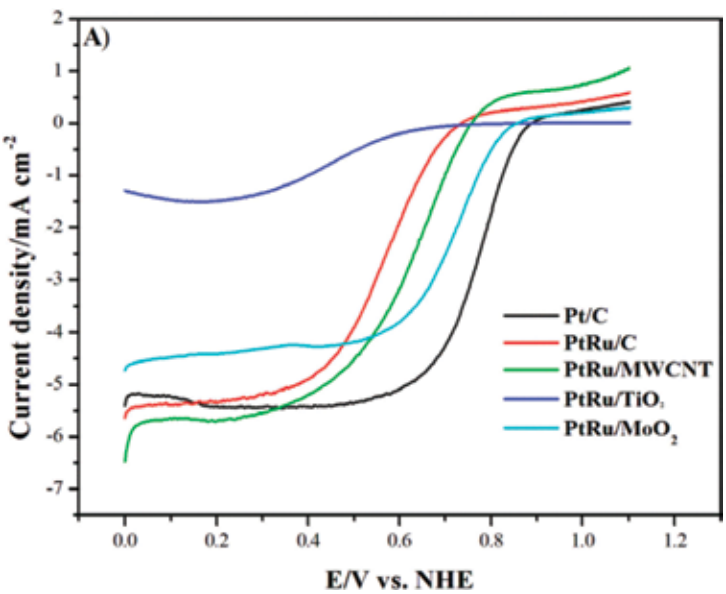

Figure 6. ORR polarisation curves of PtRu/MWCNT PtRu/MWCNT compared to Pt/C, PtRu/C PtRu/TiO_2 and PtRu/MoO_2 commercial catalysts in O_2-saturated 0.1 M $HClO_4$ at 20 m V/s and 1600 rpm [70].

	ORR catalytic activity at 0.9 V	
Catalyst	**MA (mA mg^{-1})**	**SA (mA cm^{-2})**
Pt/C	85.85	0.188
PtRu/C	463	1.66
PtRu/MWCNT	35.6×10^3	111
PtRu/TiO_2	18.94	1.04
PtRu/MoO_2	997	17.82

Table 1. Studying the activity of electrocatalysts towards ORR in comparison with commercial Pt/C, PtRu/C and PtRu/TiO_2.

The two main functionalities are oxygen, namely carboxyl (—COOH), hydroxyl (—OH) and carbonyl (—C=O), and nitrogen groups. Modified CNTs with nitrogen functional groups have been reported to show a much improved electrocatalytic activity towards ORR through forming thermally stable structures during heat treatment [82, 83]. Nitrogen is known to efficiently create defects on carbon materials, which might increase the edge plane exposure and thus improve the ORR activity [29]. Ghosh and Raj [84] report on an improved electrocatalytic activity towards ORR for N-doped CNTs. Wang et al. [85] report on a sponge-like nitrogen containing carbon with a high electrocatalytic ORR activity compared to commercial Pt/C with a considerably higher methanol tolerance. One distinct advantage offered by CNTs is their high resistance towards corrosion compared to CB, and hence they have an enhanced electrochemical stability compared to CB [66, 84].

CNFs have been reported to show an improved electrocatalytic activity towards ORR compared to CB [66]. Yang et al. [86] report on an improved electrocatalytic activity for ORR for Pd/CNF. The biggest difference between CNTs and CNFs is their exposure of active edge planes. For CNTs, the basal planes are exposed, while for CNFs, edge planes are exposed [66].

Graphene and graphene oxide (GRO) have also been investigated as another support material for electrocatalysts in fuel cells due to their high electron transfer rate, a large surface area and a high conductivity [64]. When compared to CNTs, they have a higher surface area and a similar electric conductivity for electrochemical applications and can also be produced at a lower cost compared to CNTs [21]. In graphene, both basal and edge planes interact with the electrocatalysts, while for CNTs, only basal planes are exposed [66]. A surface built up only of basal planes is said to have a homogeneous surface, while a surface built up of both basal and edge planes is said to have a heterogeneous surface. Heterogeneous surfaces are reported to better stabilise the metal in a highly dispersed state. It has been reported that Pd/GRO shows a better ORR activity and forms a four-electron oxygen-reduction process compared to Pt [87–89]. N-doped graphene has been reported to show an improved electrocatalytic activity towards ORR compared to graphene in acidic and alkaline media [90]. Lu et al. [91] report a superior electrocatalytic activity of N-GRO compared to GRO. The fast electron transfer rate of graphene can particularly facilitate ORR much quicker in fuel cells [66].

Other nanostructured carbon supports such as mesoporous carbon, carbon nanocoils and carbon aerogel have also been used as support material for cathode catalysts and have been reported to show an improved ORR electrocatalytic activity [76].

Although carbon supports have been reported to show an improved ORR electrocatalytic activity, carbon oxidation or corrosion due to the presence of O_2 and/or high electrode potential has been identified as one of the major causes of failure for PEMFC degradation [67]. Non-carbon supports such as electrically conducting polymers, for example, polyaniline, Ppy and mesoporous silica, have also been used as supports to improve the stability of the electrode materials. Shurma and Pollet [66] and Wang et al. [67] report on various non-carbon supports for electrocatalysts for fuel cells. However, it is reported that with non-carbon supports, no major breakthrough has been achieved as yet [66].

3.6. Anion exchange membranes

ORR is also studied in alkaline media using anion exchange membranes (AEMs) [92]. The significant reason for the change in electrolyte membrane from acid to alkaline is the improved electrokinetics of ORR in alkaline [93]. Pd is emerging as an alternative catalyst compared to Pt in alkaline. It is reported that more ORR catalysts are available for alkaline solutions compared to acidic solutions, due to excessive corrosion in acidic media. Pt/C in basic media is said to enhance ORR towards alcohol [94, 95], while non-Pt catalysts also showed an improved ORR when employed. In addition, in alkaline media, Pt/C is more tolerant to alcohol crossover due to its inactivity in alcohol oxidation reaction. Pd alloys are reported to be comparable or slightly better than Pt/C [4]. Kim et al. reported on PdSn using anion exchange membrane (AEM) which showed an improved ORR electrocatalytic activity with a high methanol tolerance compared to commercial Pt/C tested in proton exchange membrane [42]. He and Cairns [96] report on various electrocatalysts for ORR in AEM.

4. Mechanisms for ORR in the presence of an electrocatalyst

Oxygen reduction on Pt is one of the most extensively studied mechanisms [3]. It involves a multi-electron process with a number of elementary steps, involving different reaction intermediates. The mechanism can be shown schematically as follows [97] (**Figure 7**).

From the mechanism, only two products are observed with ORR on Pt, either H_2O, which can directly form through a four-electron reduction with the rate constant k_1, or adsorbed hydrogen peroxide ($H_2O_{2,\ ads}$), which is through a two-electron process with the rate constant k_2, which can be reduced further by another two-electron process to form water with rate

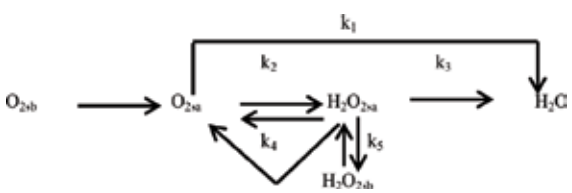

Figure 7. A simplified schematic pathway of oxygen reduction reaction for both acidic and alkaline media [7].

constant k_3, or be chemically decomposed on the electrode surface (k_4), or be desorbed in the electrolyte solution (k_5). For ORR in fuel cells, the direct four-electron process is required.

Oxygen reduction on a Pt catalyst in acid media occurs via dissociative adsorption of O_2 followed by the protonation of the adsorbed species, with the former being the rate-determining step [55].

The main steps in the mechanism of ORR are given subsequently. One is known as dissociative mechanism for a low current density range and the other associative mechanism for a high current density range:

Dissociative mechanism:

$$1/2O_2 + Pt \rightarrow PtO \tag{16}$$

$$PtO + H^+ + e^- \rightarrow Pt - OH \tag{17}$$

$$Pt - OH + H^+ + e^- \rightarrow H_2O + Pt \tag{18}$$

In this mechanism, no H_2O_2 is formed. On the Pt surface, the O_2 adsorption breaks the O—O bond and forms adsorbed atomic O with further gain of two electrons, in the two consecutive steps, forming H_2O. Because there is no adsorption of O_2 on the surface, no H_2O_2 can be formed. This mechanism can be considered as the direct four-electron reduction reaction.

Associative mechanism:

$$O_2 + 2Pt \rightarrow Pt_2O_2 \tag{19}$$

$$Pt_2O_2 + H^+ + e^- \rightarrow Pt_2 - O_2H \tag{20}$$

$$Pt_2 - O_2H \rightarrow Pt - OH + Pt - O \tag{21}$$

$$Pt - OH + Pt - O + H^+ + e^- \rightarrow Pt - OH + Pt - OH \tag{22}$$

$$Pt - OH + Pt - OH + 2H^+ + 2e^- \rightarrow 2Pt + 2H_2O \tag{23}$$

In this mechanism, no H_2O_2 is involved as well. Because there is adsorbed O_2 on the surface, O—O may not be broken down in the following steps, resulting in the formation of H_2O_2, which can be reduced further to form water.

Pt shows two Tafel slope regions. At a high potential, low current density (>0.8 V), the electrode surface is a mixture of Pt and PtO with the Tafel slope of 60 mV dec^{-1} and the reaction order 0.5 with respect to pH in alkaline media. The fractional reaction order was represented in terms of the first electrochemical step as a rate-determining step under the Temkin isotherm, that is, the adsorption of reaction intermediates O_{ads}, OH_{ads} and HO_{2ads} [98, 99].

The rate expression under Temkin conditions of adsorption is

$$j = k\,[O_2]\,[H^+]^{½} \exp[-\eta F/RT] = 374\,k\,[O_2]\,[OH^-]^{½} \exp[-\eta F/RT] \tag{24}$$

where k is the rate constant and η is the over-potential.

At a low potential, high current density (<0.8 V), the electrode surface is a pure Pt with the Tafel slope of 120 mV dec^{-1} and the reaction order 0 with respect to pH in alkaline media, with H_2O as the reacting species. The adsorption of intermediate species to a Langmuir isotherm under Temkin conditions no longer holds.

The rate expression under Langmuir conditions is

$$j = k\,[O_2]\,\exp\,[-\beta\,\eta F/RT] \tag{25}$$

where β is the symmetry factor.

The reaction is of the first order with respect to O_2 in solutions. It was found that the H_2O_2 formed was greater in an alkaline solution than in an acidic one [4, 94]. In alkaline solutions, about 80% of the reduction current is through the direct reduction and the other current forms H_2O_2, which leads to a complicated mechanism.

Various models representing the adsorbed states of oxygen are represented in **Figure 8**.

Figure 8(a) is known as the bridge model. It is a 2:2 complex of metal oxygen where the bonding arises from the interaction between the d-orbital on the metal with a Π* and Π orbital combination on O_2 [101]. This gives rise to a singlet or a triplet nature of di-oxygen orbitals

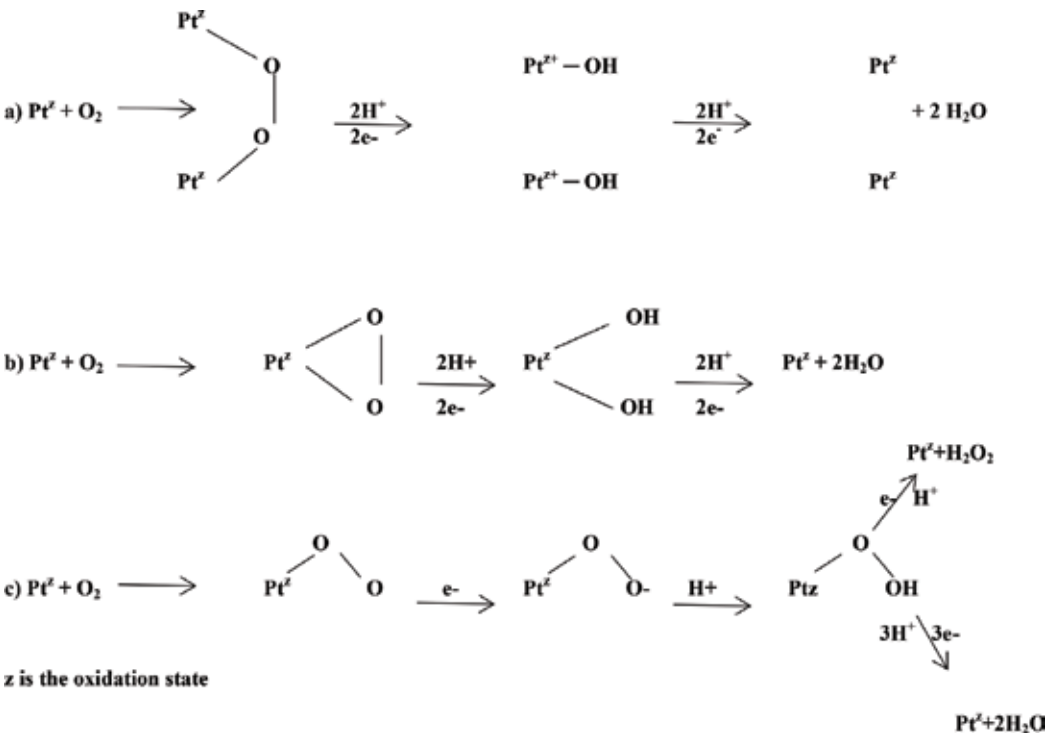

Figure 8. Oxygen reduction on Pt from the (a) bridge model, (b) Griffiths model and (c) Pauling model [100].

and determines the bridge or a transmode of interaction of di-oxygen with the metal [101]. **Figure 8(b)** is known as the Griffiths model. It is a 2:1 metal-di-oxygen complex structure, which involves a side on the interaction of oxygen with metal. This type of bonding can be viewed as rising from two contributions: (1) σ-type bonding is formed by overlapping between the Π orbitals of oxygen and the d_z^2 orbitals on the metal; (2) Π back-bond interaction between the metal d Π orbitals and partially occupied Π* antibonding orbital on O_2 arises [102]. **Figure 8(c)** is known as the Pauling model. It is a 1:1 metal-oxygen complex structure, which is an end-on interaction of O_2 with metal. In this model, the σ bond is formed by the donation of electron density from the σ-rich orbital of di-oxygen to the acceptor d_z^2 orbital on the metal. The metal's two d-orbitals, namely d_{xz} and d_{yz}, then interact with the Π* orbitals of di-oxygen, with the corresponding charge transfer from the metal to the O_2 molecule. The Griffiths and Pauling models are the preferred models due to the donating abilities of the filled Π and σ orbitals of the di-oxygen molecule, respectively [103].

5. Conclusion

ORR has a huge role to play in fuel cell development. Comparing the ORR electrocatalytic activity of Pt with other single metals, Pt shows the most improved electrocatalytic activity, but its large-scale applications are limited by its high cost and scarcity. The addition of a second metal to a metal electrocatalyst decreases its particle size (large surface area), which leads to an increased lattice strain and hence an increased electrocatalytic activity [28]. It has been concluded that multi-component catalysts improve ORR activity, although it is not conclusive on which multi-catalyst shows the most improved ORR activity, as various researchers report on different multi-component catalysts as the most improved. Although improvement has been obtained, the Pt loading required is still too high to produce PEMFCs at commercially viable prices [22]. The transition metal phthalocyanine is offering reasonable performance as an ORR catalyst, although it suffers from lack of long-term stability.

The challenge remaining is optimising the synthesis method in order to control the shape and the surface structure of especially non-spherical electrocatalysts, which are reported to show the most improved ORR electrocatalytic activity with most stable electrocatalysts, while they contribute to the lowering of Pt usage and hence cost reduction of the PEMFC.

Catalyst support is one of the critical components in improving the electrocatalytic activity of PEMFCs, as they are responsible for parameters that govern the performance of the fuel cell, that is, particle size, catalyst dispersion and stability [8]. Comparison of the carbon supports, CNTs and graphene supports provides considerable advantages concerning mass and charge transport. The disadvantage of using these supports is the costs [25]. In addition, the deposition, distribution and crystallite size of metal nanoparticles are affected by the synthesis method and oxidation treatment of carbon supports.

Using an alkaline medium, Pt-free nanoparticles can be used as electrocatalysts for fuel cells, with a reduced alcohol crossover, an improved ORR kinetics and limited risks of corrosion.

Recently, research has been focused on using AEMs. The main advantage of using AEM fuel cells over PEMFCs is that it allows for the use of less expensive, Pt-free electrocatalysts. AEM fuel cells promise to solve the cost barriers of PEMFCs.

Acknowledgements

I thank ESKOM (TESP), NRF (THUTHUKA), Ithemba Labs, Physics Department (UWC), Chemical Engineering Department (UCT) and Chemistry Department (UWC).

Conflict of interest

I have no conflict of interest to declare.

Nomenclature

AEM	anion exchange membrane
CB	carbon black
CNF	carbon nanofibre
CNT	carbon nanotube
GRO	graphene oxide
MWCNT	multi-walled carbon nanotube
NHE	normal hydrogen electrode
ORR	oxygen reduction reaction
PEMFC	polymer electrolyte membrane fuel cell
Ppy	polypyrrole
RHE	reversible hydrogen electrode
SWCNT	single-walled carbon nanotube

Author details

Lindiwe Khotseng

Address all correspondence to: lkhotseng@uwc.ac.za

Department of Chemistry, University of the Western Cape, South Africa

References

[1] Liu B, Bard AJ. Scanning electrochemical microscopy. 45. Study of the kinetics of oxygen reduction on platinum with potential programming on tip. Journal of Physical Chemistry B. 2002;**106**(49):12801-12806. DOI: 10.1021/jp026824f

[2] Song C, Zhang J. Electrocatalytic oxygen reduction reaction. In: Zhang J, editor. PEM Fuel Cell Electrocatalyst: Fundamentals and Applications. London: Springer; 2008. pp. 89-134. DOI: 10.1007/978-1-84800-936-3

[3] Raghuveer V, Kumar K, Viswanathan B. Nanocrystalline lead ruthenium pyrochlore as oxygen reduction electrode. Indian Journal of Engineering and Material Science. 2002;**9**:137-140

[4] Meng H, Zeng D, Xie F. Pd based electrocatalysts for proton exchange membrane fuel cells. Catalysts. 2015;**5**:1221-1274. DOI: 10.3390/cata5031221

[5] Damjanovic A, Genshaw MA, Bockris JOM. The mechanism of oxygen reduction at platinum in alkaline solutions with special reference to H_2O_2. Journal of the Electrochemical Society. 1967;**114**:1107-1112. DOI: 10.1149/1.2426425

[6] Damjanovic A, Sepa DB, Vojnovic MV. New evidence supports the proposed mechanism of O_2 reduction at oxide free platinum-electrodes. Electrochimica Acta. 1979;**24**:87-89. DOI: 10.1016/0013-4686(79)87013-9

[7] Wroblowa HS, Pan YC, Razumney G. Electro-reduction of oxygen: A new mechanistic criterion. Journal of Electroanalytical Chemistry. 1976;**69**(2):195-201. DOI: 10.1016/S0022-0728(76)80250-1

[8] Ozoemena KI. Nanostructured platinum free electrocatalysts in alkaline direct alcohol fuel cells: Catalyst design, principles and applications. RCS Advances. 2016;**6**:89523-89549. DOI: 10.1039/C6RA15057H

[9] Yuan XZ, Song C, Wang H, Zhang J. EIS diagnosis for PEM fuel cell performance. In: Electrochemical Impedance Spectroscopy in PEM Fuel Cells: Fundamentals and Applications. London: Springer; 2010. pp. 193-262. DOI: 10.1007/978-1-84882-845-2

[10] Roquet L, Belgsir EM, Lèger JM, Lamy C. Kinetics and mechanisms of the electrocatalytic oxidation of glycerol as investigated by chromatographic analysis of the reaction products: Potential and pH effects. Electrochimica Acta. 1994;**39**:237-2394. DOI: 10.1016/0013-4686(94)E0190-Y

[11] Corrosion: Impact, Principles and Practical Solutions. What is Overpotential [Internet]. 1999. Available from: http://corrosion-doctors.org/Corrosion-Kinetics/Overpotential-definition.htm [Accessed: 2018-01-6]

[12] Fuel Cell Technology. Hydrogen Fuel Cell Engines and Related Technologies [Internet]. 2001. Available from: https://energy.gov/sites/prod/files/2014/03/f9/fcm00r0.pdf [Accessed: 2018-12-28]

[13] Corrosion for Engineers. Corrosion current. [Internet]. 2005. Available from: https://canteach.candu.org/Content%20Library/20053213.pdf [Accessed: 2018-01-6]

[14] Lim B, Kim JW, Hwang SJ, Yoo SJ, Cho EA, Lim TH, Kim SK. Fabrication and characterization of high activity Pt/C electrocatalysts for oxygen reduction. Bulletin of the Korean Chemical Society. 2010;**31**(6):1577-1582. DOI: 10.5012/bkcs.2010.31.6.1577

[15] Kongkanand A, Kuwabata S, Girishkumar G, Kamat P. Single wall carbon nanotubes supported platinum nanoparticles with improved electrocatalytic activity for oxygen reduction reaction. Langmuir. 2006;**22**(5):2392-2398. DOI: 10.1021/la052122g

[16] Yu EH, Kremer U, Scott UK. Principles and materials aspects of direct alkaline alcohol fuel cells. Energies. 2010;**3**:1499-1528. DOI: 10.3390/en3081499

[17] Yuan W, Scott K, Cheng H. Fabrication and evaluation of Pt-Fe alloys as methanol tolerant cathode materials for direct methanol fuel cells. Journal of Power Sources. 2006;**163**:323-329. DOI: 10.1016/j.jpowsour.2006.09.005

[18] Wang B. Recent developments of non-platinum catalysts for oxygen reduction reaction. Journal of Power Sources. 2005;**152**. DOI: 1-15. DOI: 10.1016/j.jpowsour.2005.05.098

[19] Modibedi RM, Mathe MK, Motsoeneng RG, Khotseng L, Ozoemena KI, Louw EK. Electrodeposition of Pd on carbon paper and Ni foam via surface limited redox replacement reaction for oxygen reduction reaction. Electrochimica Acta. 2014;**128**:406-411. DOI: 10.1016/j.electacta.2013.11.062

[20] Wang XM, Wang ME, Zhou DD, Xia YY. Structural design and facile synthesis of a highly efficient catalyst for formic acid electro-oxidation. Physical Chemistry Chemical Physics. 2011;**13**:13594-13597. DOI: 10.1039/C1CP21680E

[21] Thompsett D. Catalysts for proton exchange membrane fuel cell. In: Hoogers G, editor. Fuel Cell Technology Handbook. Taylor & Francis Group: CRC Press LLC; 2003. p. 6.1-6.23

[22] Choi HJ, Jung SM, Seo JM, Chang DW, Dai L, Baek JB. Graphene for energy conversion and storage in fuel cells and supercapacitors. Nano. 2012;**1**:534-551. DOI: 10.1016/j.nanoen.2012.05.001

[23] Nishanth KG, Sridhar P, Pitchumani S, Shukla AK. Carbon supported Pt-Pd alloy as methanol-tolerant-oxygen-reduction electrocatalyst for DMFC. ECS Transactions. 2010;**28**(23):273-281. DOI: 10.1149/1.3502358

[24] Motsoeneng RG, Modibedi RM, Mathe MK, Khotseng L, Ozoemena KI. The synthesis of PdPt/carbon paper via surface limited redox replacement reactions for oxygen reduction reaction. International Journal of Hydrogen Energy. 2015;**40**:16734-16744. DOI: org/10.1016/j.ijhydene.2015.08.060

[25] Li W, Zhao X, Manthiram A. Room temperature synthesis of Pd/C cathode catalysts with superior performance of direct methanol fuel cell. Journal of Materials Chemistry A. 2014;**2**:3468-3476. DOI: 10.1039/C3TA14193D

[26] Antolini E. Effect of structural characteristics of binary palladium-cobalt fuel cell catalysts on the activity for oxygen reduction. ChemPlusChem. 2014;**79**:765-775. DOI: 10.1002/cplu.201402034

[27] Norskov JK, Rossmeis L, Logadotir A, Lindqvist L, Kitchin JR, Bligaard T. Origin of the overpotential for oxygen reduction at a fuel cell cathode. Journal of Physical Chemistry B. 2004;**108**:17886-17892. DOI: 10.1021/jp047349j

[28] Antolini E. Palladium in fuel cell catalysis. Energy and Environmental Science. 2009;**2**:915-931. DOI: 10.1039/B820837A

[29] Li W, Xin Q, Yan Y. Nanostructured Pt-Fe/C cathode catalysts for direct methanol fuel cell: The effect of catalyst composition. International Journal of Hydrogen Energy. 2010;**35**:25-30. DOI: 10.1016/j.ijhydene.2010.01.013

[30] Zhang Z, Li M, Wu Z, Li W. Ultra-thin PtFe-nanowires as durable electrocatalysts for fuel cells. Nanotechnology. 2011;**22**:15602 (5 pp). DOI: 10.1088/0957-4484/22/1/015602

[31] Yang H, Vogel W, Lamy C, Alonso-Vante N. Structure and electrocatalytic activity of carbon supported Pt-Ni alloy nanoparticles toward the oxygen reduction reaction. Journal of Physical Chemistry B. 2004;**108**(30):11024-11034. DOI: 10.1021/jp049034

[32] Remona AM, Phani KLN. Study of methanol tolerant oxygen reduction reaction at Pt/Bi/C bimetallic nanostructured catalysts. Fuel Cells. 2011;**11**(3):385-393. DOI: 10.1002/fuce.201000082

[33] Lim B, Jiang M, Camargo PHC, Cho EC, Tao J, Lu X, Zhu Y, Xia Y. Pd-Pt bimetallic nanodendrites with high activity for oxygen reduction. Science. 2009;**324**:1302-1305. DOI: 10.1126/science.1170377

[34] Paulus UA, Wokaun A, Scherer GG, Schmidt TJ, Stamenkovic V, Markovic NM, Ross PN. Oxygen reduction on high surface area Pt based alloy catalysts in comparison to well defined smooth bulk alloy electrodes. Electrochimica Acta. 2002;**47**(22-23):3787-3798. DOI: 10.1016/S0013-4686(02)00349-3

[35] Zhang J, Vukmirovic MB, Klie R, Sasaki K, Adzic RR. Platinum monolayer electrocatalysts for O_2 reduction: Pt monolayer on Pd (111) and on carbon supported Pd nanoparticles. Journal of Physical Chemistry B. 2004;**108**:10955-10964. DOI: 10.1021/jp0379953

[36] Chang SH, Su WN, Yeh MH, Pan CJ, Yu LK, Liu DG, Lee JF, Hwang BJ. Structural and electronic effects of carbon supported Pt_xPd_{x-1} nanoparticles on the electrocatalytic activity of the oxygen reduction reaction and on methanol tolerance. Chemistry—A European Journal. 2010;**16**(36):11064-11071. DOI: 10.1002/chem.201000458

[37] Tiwari JN, Tiwari RN, Singh G, Kim KS. Review: Recent progress in the development of anode and cathode catalysts for direct methanol fuel cells. Nano Energy. 2013;**2**(5):553-578. DOI: 10.1016/j.nanoen.2013.06.009

[38] Xu JB, Zhao TS, Li YS, Yang WW. Synthesis and characterization of the Au modified Pd cathode catalyst for alkaline direct ethanol fuel cells. International Journal of Hydrogen Energy. 2010;**35**:9693-9700. DOI: 10.1016/j.ijhydene.2010.06.074

[39] Xu JB, Zhao TS, Yang WW, Shen SY. Effect of surface composition of Pt-Au alloy cathode catalyst on the performance of direct methanol fuel cells. International Journal of Hydrogen Energy. 2010;**35**:8699-8706. DOI: 10.1016/j.ijhydene.2010.05.008

[40] Kim Y, Hong JW, Lee YW, Kim M, Kim D, Yun WS, Han SW. Synthesis of AuPt heteronanostructures with enhanced electrocatalytic activity toward oxygen reduction. Angewandte Chemie International Edition. 2010;**49**:10197-10201. DOI: 10.1002/anie.201005839

[41] Fu G, Liu Z, Chen Y, Lin J, Tang Y, Lu T. Synthesis and electrocatalytic activity of Au@Pd core shell nanothorns for the oxygen reduction reaction. Nano Research. 2014;**7**(8):1205-1214. DOI: 10.1021/jp9119588

[42] Kim J, Momma T, Osaka T. Cell performance of Pd-Sn catalysts in passive direct methanol alkaline fuel cell using anion exchange membrane. Journal of Power Sources. 2009;**189**:999-1002. DOI: 10.1016/j.jpowsour.2008.12.108

[43] Stassi AD, Urso C, Baglio V, Di Blasi A, Antonucci V, Arico AS. Electrocatalytic behaviour for oxygen reduction reaction of small nanostructured crystalline bimetallic Pt-M supported catalysts. Journal of Applied Electrochemistry. 2006;**36**:1143-1149. DOI: 0.1007/s10800-006-9197-9

[44] Elzing A, Van der Putten A, Visscher W, Barendrecht E. The cathodic reduction of oxygen at cobalt phthalocyanine. Influence of electrode preparation on electrocatalysis. Journal of Electroanalytical Chemistry. 1986;**200**:313-322. DOI: 10.1016/0022-0728(86)90063-X

[45] Greeley J, Stephens IEL, Bondarenk AS, Johansson TP, Hansen HA, Jaramillo TF, Rossmeis J, Chorkendorff I, Norskov JK. Alloys of platinum and early transition metals as oxygen reduction electroctrocatalysts. Nature Chemistry. 2009;**1**:552-556. DOI: 10.1038/nchem.367

[46] Shao M, Peles A, Shoemaker K. Electrocatalysis on platinum nanoparticles: Size effect on oxygen reduction reaction activity. Nano. 2011;**11**:3714-3719. DOI: 10.1021/nl2017459

[47] Subhramannia M, Pillai VK. Shape dependent electrocatalytic activity of Pt nanostructures. Journal of Materials Chemistry. 2008;**18**:5858-5870. DOI: 10.1039/B811149A

[48] Hao D, Xue-Zhao S, Cheng-Min S, Chao H, Chuan X, Chen L, Yuan T, Deng-Ke W, Hong-Jun G. Synthesis on monodisperse palladium nanocubes and their catalytic activity for methanol electro-oxidation. Chinese Physics B. 2010;**19**:106104 (5pp). DOI: 10.1088/1674-1056/19/10/106104

[49] Narayanan R, El-Sayed MA. Shape dependent catalytic activity of platinum nanoparticles in colloidal solution. Nano Letters. 2004;**4**:1343-1348. DOI: 10.1021/nl0495256

[50] Kuai L, Geng B, Wang S, Zhao Y, Luo Y, Jiang H. Silver and gold icosahedra one-pot water-based synthesis and their superior performance in the electrocatalysis for oxygen reduction reactions in alkaline media. Chemistry—A European Journal. 2011;**17**:3482-3489. DOI: 10.1002/chem.201002949

[51] Adonisi T. Electrochemical characterization of platinum based catalysts for fuel cell applications [thesis]. Bellville: University of the Western Cape; 2012

[52] Bezerra CWB, Zhang L, Marques ALB, Zhang J. A review of heat treatment effect on activity and stability of PEM fuel cells for oxygen reduction reaction. Journal of Power Sources. 2007;**173**:891-908. DOI: 10.1016/j.jpowsour.2007.08.028

[53] Koh S, Strasser P. Electrocatalysis on bimetallic surfaces modifying catalytic reactivity of oxygen reduction by voltammetric surface dealloying. Journal of the American Chemical Society. 2007;**129**:12624-12625. DOI: 10.1021/ja0742784

[54] Jeyabharathi C, Venkateshkumar P, Mathiyasaru J, Phani KLN. Platinum-tin bimetallic nanoparticles for methanol tolerant oxygen-reduction activity. Electrochimica Acta. 2008;**54**(2):448-454. DOI: /10.1016/j.electacta.2008.07.053

[55] Easton EB. Chemical modification of fuel cell catalysts and electrochemistry of proton exchange membrane fuel cell electrode [thesis]. St. John's: Memorial University of Newfoundland; 2003

[56] Lamy A, Lima V, LeRhun F, Delime C, Coutanceau C, Leger JM. Recent advances in the development of direct alcohol fuel cells (DAFC). Journal of Power Sources. 2002;**105**: 283-296. DOI: 10.1016/S0378-7753(01)00954-5

[57] Martin LG. Synthesis and characterization of Pt-Sn/C cathode catalysts via polyol reduction method for use in direct methanol fuel cell [thesis]. Bellville: University of the Western Cape; 2013

[58] Jahnke H, Schonbron M, Zimmerman G. Organic dyestuffs as catalysts for fuel cells. In: Boschke FL, editor. Physical and Chemical Applications of Dye Stuff. 61. Berlin: Springer-Verlag; 1976. pp. 133-181. DOI: 10.1007/BFb0046059

[59] Zagal J, Bindra P, Yeager E. A mechanistic study of O_2 reduction on water soluble phthalocyanines adsorbed on graphite electrodes. Journal of the Electrochemical Society. 1980;**127**:1506-15017. DOI: 10.1149/1.2129940

[60] Lefèvre M, Proietti E, Jaouen F, Dodelet JP. Iron based catalysts with improved oxygen reduction activity in polymer electrolyte fuel cells. Science. 2009;**324**:71-74. DOI: 10.1126/science.1170051

[61] Zhong HX, Zhang HM, Liu G, Liang YM, Hu JW, Yi BL. A novel non-noble electrocatalyst for oxygen reduction in proton exchange membrane fuel cells. Electrochemistry Communications. 2006;**8**:707-712. DOI: 10.1016/j.jpowsour.2006.11.080

[62] Matsuki K, Kamada H. Oxygen reduction electrocatalysis on some manganese oxides. Electrochimica Acta. 1986;**31**:13-18. DOI: 10.1016/0013-4686(86)80054-8

[63] Chang CC, Wen TC, Tien HJ. Kinetics of oxygen reduction at oxide derived Pd electrodes in alkaline solution. Electrochimica Acta. 1997;**42**:557-565. DOI: 10.1016/S0013-4686(96)00195-8

[64] Vago ER, Calvo EJ. Oxygen electro-reduction on iron oxide electrodes: iii. Heterogenous catalytic H_2O_2 decomposition. Journal of Electroanalytical Chemistry. 1995;**388**:161-165. DOI: 10.1016/0022-0728(95)03860-J

[65] Kim J, Ishihara A, Mitsushima S, Kamiya N, Ota K. Catalytic activity of titanium oxide for oxygen reduction reaction as a non-platinum catalyst for PEFC. Electrochimica Acta. 2007;**52**:2492-2497. DOI: 10.1016/j.electacta.2006.08.059

[66] Shurma S, Pollet BG. Review: Support materials for PEMFC and DMFC electrocatalysts. Journal of Power Sources. 2012;**208**:96-119. DOI: 10.1016/j.jpowsour.2012.02.011

[67] Wang YJ, Wilkinson DP, Zhang J. Review: Noncarbon support materials for polymer electrolyte membrane fuel cell electrocatalysts. Chemical Reviews. 2011;**111**(12): 7625-7651. DOI: 10.1021/cr100060r

[68] Montero-Ocampo C, Garcia JRV, Estrada EA. Comparison of TiO_2 and TiO_2-CNT as cathode catalyst supports for ORR. International Journal of Electrochemical Science. 2013;**8**:12780-11280

[69] Ruiz-Camacho B, Valenzuela MA, Alonso-Vante N. The effect of metal oxide-carbon support on electrocatalysts for fuel cell reactions. World Journal of Engineering. 2002:973-974

[70] Khotseng L, Bangisa B, Modibedi M, Linkov V. Electrochemical evaluation of Pt based binary catalysts on various supports for direct methanol fuel cells. Electrocatalysis. 2016;**7**:1-12. DOI: DOI 10.1007/s12678-015-0282-x

[71] Li J, Zhou H, Zhuo H, Wei Z, Zhuang G, Zhong X, Deng S, Lia X, Wang J. Oxygen vacancies on TiO2 promoted the activity and stability of supported Pd nanoparticles for the oxygen reduction reaction. Journal of Materials Chemistry A. 2018;**6**:2264-2272. DOI: 10.1039/C7TA09831F

[72] Singh RN, Lal B, Malyiya M. Electrocatalytic activity of electrodeposited composite pf polypyrrole and $CoFe_2O_4$ nanoparticles towards oxygen reduction reaction. Electrochimica Acta. 2004;**49**:4605-4612. DOI: 10.1016/j.electacta.2004.05.015

[73] Usgaocar AR, Chong Harold MH, De Groot CH. Modulation of carbon nanotube metal contacts in gaseous hydrogen environment. Journal of Nanoscience. 2014:1-7. DOI: 10.1155/2014/404519

[74] Villiers D, Sun SH, Serventi AM, Dodelet JP, Dsilets S. Characterization of Pt nanoparticles deposited onto carbon nanotubes grown on carbon paper and evaluation of this electrode for the reduction of oxygen. Journal of Physical Chemistry B. 2006;**110**(51):25916-25925. DOI: 10.1021/jp065923g

[75] Khotseng L. Electrocatalysts for direct methanol fuel cells. In: Merhandez R, Dunning C, editors. Direct Methanol Fuel Cells: Applications, Performance and Technology. Hauppauge: Nova Science Publishers; 2017. pp. 1-50

[76] Yaldagard M, Jahanshahi M, Seghatoleslami N. Carbonaceous nanostructured support materials for low temperature fuel cell electrocatalysts. World Journal of Nanoscience and Engineering. 2013;**3**:121-153. DOI: 10.4236/wjnse.2013.34017

[77] Li D, Lv H, Kang Y, Markovic NM, Vojislav R. Progress in the development of oxygen reduction reaction catalysts for low-temperature fuel cells. Annual Review of Chemical Biomolecular Engineering. 2016;**7**:509-532. DOI: 10.1146/annurev-chembioeng-080615-034526

[78] Xing Y. Synthesis and electrochemical characterization of uniformly dispersed high loading of Pt nanoparticles on sonochemically treated carbon nanotubes. Journal of Physical Chemistry B. 2004;**108**(51):19255-19259. DOI: 10.1021/jp046697i

[79] Sevjidsuren G, Zils S, Kaserer S, Wolz A, Ettingshausen F, Dixon D, Schoekel A, Roth C, Altantsog P, Sangaa D, Ganzorig CH. Effect of different support morphologies and Pt particle sizes in electrocatalysts for fuel cell application. Hindawi Publishing Cooparation, Journal of Nanomaterials. 2010:Article ID 852786 (9 pp). DOI: 10.1155/2010/0852786

[80] Jukk K, Alexeyeva N, Johans C, Kontturi K, Tammeveski K. Oxygen reduction on Pd nanoparticle/multi-walled carbon nanotube composites. Journal of Electroanalytical Chemistry. 2012;**666**:67-75. DOI: doi.org/10.1016/j.jelechem.2011.12.003

[81] Wang S, Jiang SP, White TJ, Guo J, Wang X. Electrocatalytic activity and interconnectivity of Pt nanoparticles on multi-walled carbon nanotubes for fuel cells. Journal of Physical Chemistry C. 2009;**113**:18935-18945. DOI: 10.1021/jp906923z

[82] Nagaiah TC, Kundu S, Bron M, Muhler M, Schumann W. Nitrogen doped carbon nanotubes as a cathode catalyst for the oxygen reduction reaction in alkaline medium. Electrochemistry Communications. 2010;**12**:338-341. DOI: 10.1016/j.elecom.2009.12.021

[83] Gong K, Du F, Xia Z, Durstock M, Dai L. Nitrogen doped carbon nanotube arrays with high electrocatalytic activity for oxygen reduction. Science. 2009;**323**:760-763. DOI: 10.1126/science.1168049

[84] Ghosh S, Raj CR. Facile in situ synthesis of multiwall carbon nanotube supported flower-like Pt nanostructures: An efficient electrocatalyst for fuel cell application. Journal of Physical Chemistry C. 2010;**114**:10843-10849. DOI: 10.1021/jp100551e

[85] Wang H, Wang W, Key J, Ji S, Ma Y, Khotseng L, Lv W, Wang R. Sponge like carbon containing nitrogen and iron provides a non-precious oxygen reduction catalyst. Journal of Solid State Electrochemistry. 2005;**19**(4):1181-1186. DOI: 10.1007/s1000

[86] Yang W, Yang S, Guo J, Sun G, Xin Q. Comparison of CNF and XC-72 carbon supported platinum catalysts for direct methanol fuel cell. Carbon. 2007;**45**(2):397-401. DOI: 10.1016/j.carbon.2006.09.003

[87] Goth K, Kawabata K, Fujii E, Morishige K, Kinumoto T, Miyazaki Y, Ishida H. The use of graphite oxide to produce mesoporous carbon supporting Pt, Ru or Pd nanoparticles. Carbon. 2009;**47**(8):2120-2124. DOI: 10.1016/j.carbon.2009.03.052

[88] Du SF, Lu YX, Steinberger-Wilckens R. PtPd nanowire arrays supported on reduced graphene oxide as advanced electrocatalysts for methanol oxidation. Carbon. 2014;**79**:346-353. DOI: 10.1016/j.carbon.2009.03.052

[89] Kou R, Shao YY, Wang J, Wu H, Liu J, Akasay IA, Lin Y. Enhanced activity and stability of Pt catalysts on functionalized graphene sheets for electrocatalytic oxygen reduction. Electrochemistry Communications. 2009;**11**:954-957. DOI: 10.1016/j.elecom.2009.02.033

[90] Osmieria L, Pezzolatob L, Specchia S. Recent trends on the application of PGM-free catalysts at the cathode of anion exchange membrane fuel cells. Current Opinion in Electrochemistry. 2018;**4**:9-25. DOI: 10.1016/j.coelec.2018.05.011

[91] Lu ZJ, Xu MW, Bao SJ, Tan K, Chai H, Ji CC, Chang Q, Cai CJ. Facile preparation of nitrogen-doped reduced graphene oxide as a meta-free catalyst for oxygen reduction reaction. Journal of Materials Science. 2013;**48**(23):8101-8107. DOI: 10.1007/s10853-013-7622-0

[92] Jurzinsky T, Cremers C, Jung F, Pinkwart K, Tubke J. Development of materials for anion exchange membrane direct alcohol fuel cells. International Journal of Hydrogen Energy. 2015;**40**(35):11569-11576. DOI: 10.1016/j.ijhydene.2015.02.056

[93] Rivera LM, Gonzalo G, Pastor E. Novel graphene materials for the oxygen reduction reaction. Current Opinion in Electrochemistry. 2018;**18**:23-29. DOI: 10.1016/j.coelec.2018.05.009

[94] Damjanovic A, Genshaw MA, Bockris JOM. The role of hydrogen peroxide in oxygen reduction at platinum in H_2SO_4 solution. Journal of the Electrochemical Society. 1967;**114**:466-472. DOI: 10.1149/1.2426629

[95] Maa L, He H, Hsu A, Chen R. PdRu/C catalysts for ethanol oxidation in anion-exchange membrane direct fuel cells. Journal of Power Sources. 2013;**241**:696-702. DOI: 10.1016/j.jpowsour.2013.04.051

[96] He Q, Cairns J. Review: Recent progress in electrocatalysts for oxygen reduction suitable for alkaline anion exchange membrane fuel cells. Journal of the Electrochemical Society. 2015;**162**(14):F1504-F1539. DOI: 10.1149/2.0551514jes

[97] Hsueh LK, Gonzalez ER, Srinivasan S, Chin DT. Effects of phosphoric acid on oxygen reduction kinetics at platinum. Journal of the Electrochemical Society. 1984;**131**(4):823-828. DOI: 10.1149/1.2115707

[98] Damjanovic A, Brusci V. Electrode kinetics of oxygen reduction on oxide-free platinum electrodes. Electrochimica Acta. 17;**12**:615-628. DOI: 10.1016/0013-4686(67)85030-8

[99] Liang ZX, Zhao TS, Xu JB, Zhu LD. Mechanism study of ethanol oxidation reaction on palladium in alkaline media. Electrochimica Acta. 2009;**54**:2203-2208. DOI: 10.1016/j.electacta.2008.10.034

[100] Toda T, Igarashi H, Uchida H, Watanabe M. Role of electronic property of Pt and Pt alloys on electrocatalytic reduction of oxygen. Journal of the Electrochemical Society. 1998;**145**(12):4185-4188. DOI: 10.1149/1.1838934

[101] Tatsumi K, Hoffman R. Metalloporphyrins with unusual geometries. 1. Mono-, di-, tri atom-bridged porphyrin dimers. Journal of the American Chemical Society. 1981;**103**:3328-3341. DOI: 10.1021/ja00402a018

[102] Griffith JS. On the magnetic properties of some haemoglobin complexes. Proceedings of the Royal Society of London. 1956;**A235**:23-36. DOI: 10.1098/rspa.1956.0062

[103] Pauling L. Nature of the iron-oxygen bond in oxyhaemoglobin. Nature. 1964;**203**:182-183. DOI: 10.1038/203182b0

Chapter 3

Active Sites Derived from Heteroatom Doping in Carbon Materials for Oxygen Reduction Reaction

Winston Duo Wu and Dan Xu

Additional information is available at the end of the chapter

http://dx.doi.org/10.5772/intechopen.77048

Abstract

The oxygen reduction reaction (ORR) is a key cathode reaction in fuel cells. Due to the sluggish kinetics of the ORR, various kinds of catalysts have been developed to compensate for the shortcomings of the cathode reaction. Carbon materials are considered ideal cathode catalysts. In particular, heteroatom doping is essential to achieve an excellent ORR activity. Interestingly, doping trace amounts of metals in carbon materials plays an important role in enhancing the electrocatalytic activities. This chapter describes the recent advancements with regard to heteroatom-doped carbons and discusses the active sites decorated in the carbon matrix in terms of their configurations and contents, as well as their effectiveness in boosting the ORR performance. Furthermore, trace metal residues and metal-free catalysts for the ORR are clarified.

Keywords: oxygen reduction reaction, trace metal residues, active sites, heteroatom doping

1. Introduction

Owing to the limited supply of fossil fuels and increasing number of environmental crises, sustainable energy conversion and storage devices such as fuel cells and metal-air batteries have attracted significant attention [1]. The oxygen reduction reaction (ORR) is a key cathode reaction in such systems [2–4]. The sluggish kinetics of the ORR at the cathode owing to a higher overpotential than in the anode limits the wide commercialization of these devices. Currently, only the state-of-the-art platinum/carbon black catalyst (Pt/C) has been widely used in practical applications of proton exchange membrane (PEM) fuel cells [5]. Unfortunately, the scarcity and high cost of Pt and the poor durability limits the wide commercialization of

these devices. Therefore, the development of low-cost and highly efficient catalysts for the ORR has become a "hot topic".

Earlier studies have focused on tuning the surface structure [6–8] and electronic structure [9] of Pt as well as the electrocatalyst supports [10, 11] to achieve optimum ORR activity by using the least amount of Pt. In addition, various kinds of catalysts, including transition metals and their alloys, transition metal oxides/nitrides/sulfides, as well as mixed-valence metal oxides [12, 13], carbon-based metal-free catalysts [14], and others have been developed to promote the sluggish kinetics of the ORR at the cathode. Among the catalysts studied, heteroatom-doped carbon materials are considered ideal cathode catalysts due to the high surface area, good electrical conductivity, and densely distributed active sites. Presently, carbon black (CB) [15], graphene [16, 17], carbon nanotubes (CNTs) [17, 18], and porous carbon [19] are used as support materials in carbon-based electrocatalysts. Although topological defects contribute to the intrinsic activity of nanocarbon catalysts, various kinds of active sites have been created in nanocarbon catalysts to further enhance their activity [20, 21]. For example, transition metals such as Fe, Co, Ni, Cu, Zn, and Mn display fairly strong adsorption toward oxygen in the ORR, which can enhance the ORR efficiency and performance [22, 23]. Furthermore, metal-free catalysts have also become an intriguing research area. Non-metal heteroatoms, such as N, S, B, and P, in carbon materials can serve as active sites for the ORR. The heteroatoms can alter the electronic distribution of the carbon framework and effectively increase the defects in the carbon structure, contributing to O_2 adsorption and O—O bond breaking during the ORR catalytic reaction and concurrently promoting the catalytic performance of the carbon materials. Although the individual roles of different atoms and their synergistic effects in facilitating the ORR activity are still under debate, numerous achievements have been made toward the rational design and synthesis of carbon materials with a high surface area, high electrical conductivity, and multiple heteroatom doping to achieve extraordinary ORR activities.

In fact, the ORR activity and durability of heteroatom-doped carbon even outperform those of commercially available Pt-based catalysts. Here, we aim to assemble a review of the significant scientific progress in the design and synthesis of carbon-based electrocatalysts. We discuss the activity of different doping sites to provide an understanding of the mode of heteroatom doping and the role of heteroatoms in ORR, especially their content effects in ORR.

2. Active sites in the ORR

The ORR proceeds through two pathways—partial reduction and full reduction—and involves a two-electron pathway and a four-electron pathway, respectively. The four-electron route is highly preferred due to its high efficiency in fuel cell technology. The transformation of O_2 to OOH* is the first step in this route and is also a rate-determining step. The highly active catalytic centers must be favorable to enhance the binding energy between the oxygen intermediates and the catalyst surface but weak enough that the oxygen intermediates dissociate from the catalyst surface to prevent poisoning the catalyst. Therefore, goals for designing an ORR catalyst with high efficiency are to tune the adsorption energies of the

http://dx.doi.org/10.5772/intechopen.77048

oxygen intermediates and modify the charge/spin distribution of the catalyst. Although, there is strong controversy about the role of active sites and mechanisms, the heteroatoms, even the edges and defects that can function as active sites for the ORR.

2.1. Pt-based active sites

Decreasing the loading amount of Pt and Pt-based materials to enhance the performances of fuel cells is a wise choice. A series of Pt-based catalysts were prepared. For example, Xia et al. reported the synthesis of Pt—Ag alloy nanocages (**Figure 1**) [6]. Due to the ligand effects from the electronegative Ag atoms, the O_2 transition state can be stabilized, demonstrating a high specific activity toward oxygen reduction compared with that of the state-of-the-art commercial Pt/C catalyst. Furthermore, hollow Pt—M (M = Ni, Co) nanoparticle-decorated graphene was designed as an electrocatalyst for the ORR. Due to the hollow interior, the amount of buried nonfunctional precious metal atoms decreased and hence enhanced the electrocatalytic activity and durability toward the ORR [7]. Based on the same mechanism, a hollow structure of a Pt catalyst was also reported by Li and co-workers. The obtained icosahedral Pt-enriched nanocages demonstrated a superior ORR activity [24]. In addition, Pt nanoparticles stabilized by a graphitic step-edge and combined with the effect of nanoscale confinement showed high electrochemical stability outperforming that of a commercial Pt/C [25]. Interestingly, Adzic and co-workers used titanium nickel binary nitride as a support and then several layers of Pt atoms were deposited on the robust support. The obtained catalyst exhibited high mass activity and specific activity compared with the commercial Pt/C catalyst; this result was mainly due to the synergistic effect of Ni doping and the strong interaction between the Pt layer and the support [10]. Mukerjee and co-workers designed a Pt/NbO_x/C system as an ORR catalyst and demonstrated that the Pt—O interactions improved the ORR activity [26]. Ultrathin Rh-doped Pt nanowires synthesized by Zeng and co-workers achieved remarkable activity and durability toward the ORR due to the doping of the Rh atoms and high utilization efficiency of the Pt atoms [27]. Furthermore, Pt_3Ni nanowires also showed extraordinary activity and stability toward the ORR [8].

All in all, despite numerous progresses made in exploring novel type of ORR catalyst, the state-of-the-art Pt/C catalysts still dominate. Pt-based multimetallic catalysts with various

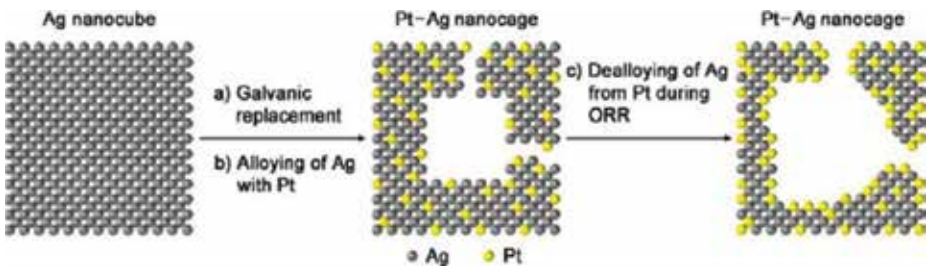

Figure 1. Schematic illustration depicting the major steps involved in the formation of Pt—Ag nanocages with high ORR activity: (a, b) alloying of Ag with Pt to generate Pt—Ag nanocages during the galvanic replacement reaction between Ag and a Pt(II) precursor and (c) dealloying of Ag from Pt during the accelerated durability test [6].

finely tuned morphologies will represent a promising research area of ORR catalyst, due to the scarcity of Pt and the unsatisfactory long-term stability.

2.2. Non-noble metal-based active sites

The search for Pt-free alternative catalysts with excellent ORR performance has attracted much attention. Accordingly, extensive efforts have been directed toward the design and synthesis of nonprecious metal-based catalysts for potential applications in fuel cells. Particularly, the co-doping of transition metals and non-metal heteroatoms have also been extensively studied due to their combined advantages. Fe—N—C catalysts have been broadly studied. Atomically dispersed Fe [28], Fe—N_x [29, 30], Fe_3C [31, 32], and Fe_3O_4 [33] are all considered ORR active sites. Dong and co-workers demonstrated that atomically dispersed Fe (1–2 wt%) played a pivotal role in promoting the ORR performance [28]. Joo et al. prepared a catalyst consisting of Fe—N_x and Fe—Fe_3C@C species (Fe content of 6.3 wt%) [31]. The experimental results indicated that the Fe—N_x sites played a dominant role in promoting the ORR via a 4-electron pathway, whereas the Fe—Fe_3C@C sites played an auxiliary role. The authors also prepared a CNT/porphyrinic carbon (PC) catalyst with densely distributed active Fe—N_x sites (**Figure 2**). The Fe contents of the CNT/PC were 2.9 wt%. This catalyst showed very high ORR activity in both alkaline and acidic media [32]. Xia and co-workers prepared Fe_3O_4 nanoparticles encapsulated in hollow core-shell structured N-doped carbon spheres. The obtained catalyst exhibited an excellent catalytic performance toward the ORR [33].

In addition to Fe—N—C catalysts, S-doped Fe—N—C catalysts have also been systematically studied. For example, Wang and co-workers found that iron sulfides/nitrogen and sulfur dual-doped mesoporous graphitic carbon spheres demonstrated excellent electrocatalytic activities toward the ORR in alkaline and acidic media. The remarkable catalytic performance was ascribed to the iron sulfide nanocrystals with an iron content of 5.9 wt% [34]. Similarly, multi-source-derived S—Fe/N/C with the atom contents of Fe 1.38% has been reported by Wang and co-workers. Five types of Fe were detected: Fe, FeS, FeN, FeC, and Fe_3O_4. Although the nature of the active sites was uncertain for the Fe/N/C, the S—Fe/N/C catalyst showed a highly efficient ORR activity [35, 36].

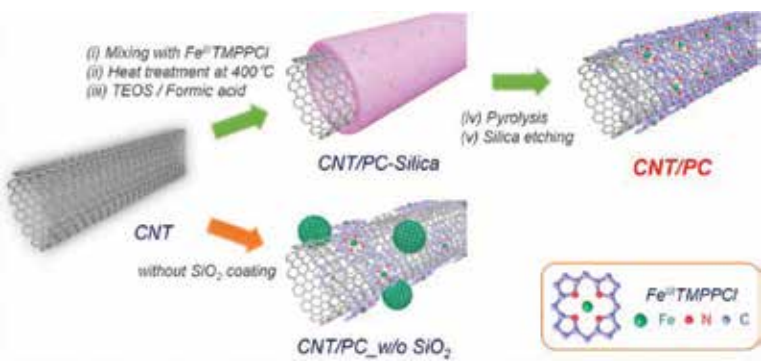

Figure 2. Synthetic scheme for the preparation of CNT/PC catalysts [32].

http://dx.doi.org/10.5772/intechopen.77048

Other earth-abundant non-noble metal-based electrocatalysts are also emerging as a new generation of low-cost and high-performance alternatives [37–44]. For example, the ORR electrocatalyst properties of Cu, N-co-doped hierarchical porous carbon with a copper content of 2.67 wt% were almost equal to those of a commercial Pt/C catalyst [37]. CoO_x nanoparticles@B, an N-decorated graphene hybrid material, was prepared by Wu and co-workers. Abundant Co—N—C active sites and high electron transfer capacity made this hybrid active in the ORR in an alkaline medium [39]. Recently, Deng and co-workers prepared Co_3O_4/Co-decorated porous graphene derived from waste paper (**Figure 3**) [40]. In this work, the cobalt(II)acetate-1,10-phenanthroline complex was selected as a precursor of both the catalyst and etcher; the control of the feed ratio of the complex, as well as the pyrolysis temperature and chemical compositions (Co_3O_4/Co) of the active sites could be finely tuned. This cost-efficient and green catalyst exhibited an efficient ORR activity with a performance comparable to that of a Pt/C catalyst due to the synergistic catalytic effects between Co_3O_4 and graphene combined with the hierarchical porous structure of the matrix. Lee and co-workers designed a nickel-containing nanoreactor (Ni@N-CNCs) [42]. Ni particles were encapsulated in N-decorated carbon nanocapsules. X-ray photoelectron spectroscopy (XPS) analysis showed the formation of N—C and Ni—N bonds in the nanoreactor and these two types of active sites significantly improved the catalytic activity. In addition, a nanoconfined effect improved the reaction rate. The electron transfer number of Ni@N-CNCs reached nearly 4.0 comparable to that of Pt/C. Successively, a manganese corrole complex [43] and ZnN_x/C catalysts [44] were explored as efficient ORR catalysts.

Additionally, bimetallic catalysts are promising candidates for the ORR. You and co-workers synthesized Fe_3C/tungsten carbide/graphitic carbon in which the Fe_3C acted as the active

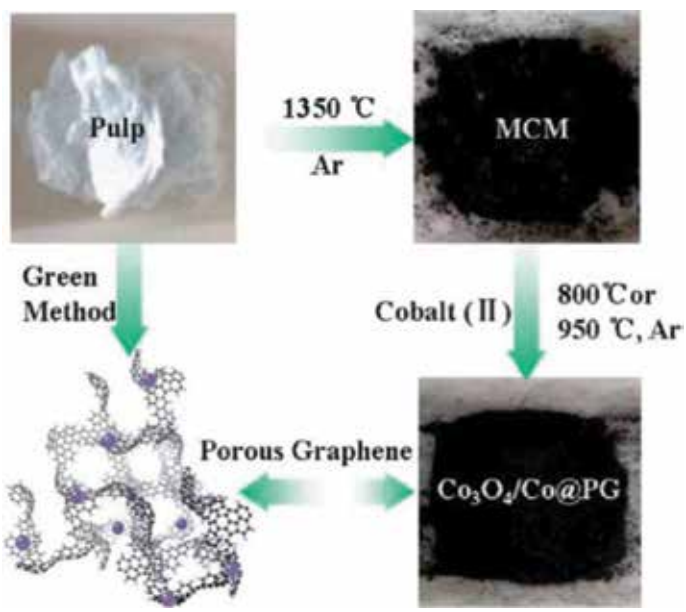

Figure 3. Schematic procedure for the preparation of functional porous graphene (Co_3O_4/Co@PG) from waste paper (MCM stands for microporous carbonaceous material and PG stands for porous graphene) [40].

sites. Meanwhile, graphitic layers and tungsten carbide nanoparticles can improve the surface chemical stability of the Fe_3C phase. The nanocomposite demonstrated high ORR efficiency via a four-electron pathway in a pH-neutral electrolyte [45]. Xu and co-workers used transition-metal spinels as a descriptor to identify the active sites in $MnCo_2O_4$ for catalyzing the ORR. Mn cations played an important role in the ORR because of the Mn valence in the octahedral sites [46]. Moreover, PdCo bimetallic nanoparticle (~8 wt%)-decorated N-doped porous carbon was fabricated by Yamauchi and co-workers. Due to the existence of the PdCo nanoparticles, the O—O bonds can be easily broken. More importantly, the three-dimensional ordered porous structure disperses the PdCo nanoparticles uniformly in the matrix. Therefore, this composite exhibited similar electrocatalytic activity to that of commercial Pt/C in alkaline media [47]. One step beyond is to further dope metal into the bimetallic catalysts. A cathode catalyst composed of a conformal film of the $PrNi_{0.5}Mn_{0.5}O_3$ and exsoluted PrO_x nanoparticles was designed by Liu and co-workers. Oxygen-vacancy-rich surfaces of the catalyst facilitated the electron transfer and hence dramatically enhanced the ORR kinetics and durability [48].

Now, the non-noble metal-based ORR catalysts have received more concern, due to their low cost and earth abundance. Although the deep insights of the active sites are not clear, non-noble metal-based ORR catalyst can outperform the catalytic performance of Pt/C. However, most synthetic strategies involved the random mixing of carbon precursors and dopants, followed by pyrolysis. Therefore, it is hard to tune the porous structures and the distribution of active sites. Future research should focus on the control of the morphology, composition, and active sites of the non-noble metal-based catalysts in high precision.

2.3. N-, S-, B-, and P-based active sites

Along with great progress made in metal-based catalysts, metal-free catalysts have attracted significant attention. Due to their high catalytic performance, long-term stability, and durability, electronegative N-doped carbon materials have been broadly studied. Pyridinic-N and graphitic-N were found to be the most highly active sites for the ORR. It is still under debate which configuration contributes more to the ORR. In fact, it is difficult to determine the role of a single N-type because high-temperature pyrolysis tends to introduce a mixture of N types. Surprisingly, synthetic strategies favorable for obtaining specific types of C—N bonding have been developed [49, 50]. Specifically, Zhang and co-workers prepared pyridinic-N dominated graphene aerogels by the etching effect of NH_3. The authors found that a long annealing time at 900°C was favorable for obtaining pyridinic-N. An N content of up to 12.2 at% with 90.4% pyridinic nitrogen has been achieved [51]. Furthermore, g-C_3N_4 is an ideal nitrogen dopant with an N content of 57.1 at%. A series of studies have been reported using g-C_3N_4 as both the template and nitrogen source [52–54]. Yan and co-workers reported a facile strategy for the synthesis of nitrogen-doped porous carbon with an N content of 10.49 at% [53]. Polypyrrole was used as the carbon and heteroatom sources and g-C_3N_4 acted as a sacrificial template and nitrogen sources. The XPS spectra of N 1 s indicated the existence of pyridinic-N, pyrrolic-N, graphitic-N, and oxidized-N. Due to the high specific surface area and N content as well as massive edges and defects, the obtained porous carbon exhibited excellent ORR activity. In addition, nitrogen-doped carbon nanoparticle–carbon nanofiber composites prepared by Ishizaki and co-workers demonstrated long-term durability and high tolerance to methanol. This can be attributed to the high conductivity of the carbon nanofibers and the largely

exposed active sites [55]. Task-specific tubular nanoporous polycarbazole-derived N-doped carbon nanotubes [56] and highly pyridinic nitrogen (up to 14.9 wt%)-doped ultra-hollow carbon frameworks [57] have also been reported. The design of carbon structures with multi-component active centers can in principle enhance the ORR activity. Two-dimensional N- and S-co-doped graphitic sheets with abundant interfacial active sites showed catalytic activity comparable to that of the commercial Pt/C [58]. In addition, N- and P-co-doped porous carbon networks showed high activities and excellent durability for ORR [59]. More interestingly, an N- and S-doped carbon nanofiber network coated with N- and P-doped carbon nanoparticles showed superior ORR performance due to the integration of N, S, and P in the carbon hybrid [60]. Zhi and co-workers studied the ORR activity of B-, P-, and S-doped g-C_3N_4. The XPS results suggested the formation of B—N, P—N, and S—C bonds. The experimental results indicated that S- and P-doping enhanced the electrocatalytic performance of ORR, whereas B-doping deactivated the ORR process. The authors proposed that B, S, and P atoms are active sites in the ORR with the catalytic activity trend of S-doped > P-doped > g-C_3N_4 > B-doped g-C_3N_4 [61].

Now, metal-free catalysts, commonly decorated with N, B, P, or S, have emerged as promising catalysts in ORR, due to the high methanol tolerance and excellent long-term stability. In fact, design and synthesis of metal-free catalysts with satisfactory ORR performance in pH-universal electrolyte is still a challenge.

2.4. Trace metal-based active sites

It has been reported that metallic impurities within sp^2 carbon nanomaterials may dominate the electrochemistry of the materials [62, 63]. Jiang and co-workers prepared sulfur, trace nitrogen, and iron co-doped porous carbon foams with an Fe content of 0.27 at%. They proposed that C—S moieties and the synergistic effect of sulfur, the trace amount of nitrogen, and iron contributed to the efficient electrocatalytic properties [64]. Wang and co-workers decorated Pd_3V bimetallic alloy nanoparticles with Pt (Pt to Pd nominal atomic ratio at 1:30). With the exposure of more active sites of the Pt, the obtained catalyst showed high catalytic activity and stability in the ORR with a 30-mV positive half-wave potential ($E_{1/2}$) comparable to that of commercial Pt/C [65]. Surprisingly, the presence of trace Au (Au/Pt atomic ratio = 0.0005) can significantly enhance the ORR durability of a PtCu alloy [66]. Similarly, incorporating trace amounts of gold (Au:Pd = 1:100) in Pd_6CoCu nanocatalysts can markedly improve the durability of the ORR (**Figure 4**). Synchrotron X-ray absorption spectroscopy showed that gold replaced cobalt and copper on the surface and in the interior of the nanoparticles. This study developed a new strategy for enhancing the stability of fuel-cell catalysts [67].

Impressively, Schuhmann and co-workers systematically investigated the influence of trace metal residues on the ORR activity. They prepared a metal-free catalyst and then deliberately incorporated metal precursors into the catalyst. The experimental results indicated that the addition of Fe with 0.05 wt% to the metal-free catalyst significantly improved its ORR activity [68]. Pumera and co-workers found that a Mn content of 0.0018 wt% in graphene was sufficient to enhance the electrocatalytic properties toward the ORR. In addition, they claimed that the elemental analysis of the metal contents should be provided to prove that the catalyst is"metal-free" [69]. Recently, we prepared a catalyst for the ORR derived from *Gentiana scabra*

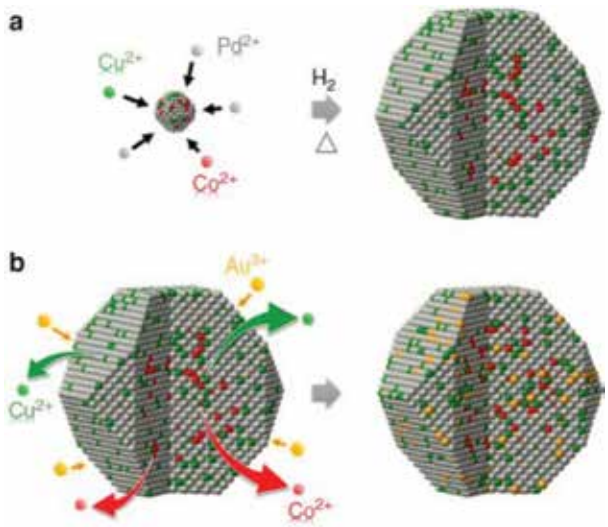

Figure 4. Schematic illustration of the formation of Pd_6CoCu/C (a) and Au-Pd_6CoCu/C (b) [67].

Bunge (natural biomass) (**Figure 5**). Notably, the obtained catalyst showed an enhanced ORR activity compared with other biomass-derived carbon materials [70]. This could be partly due to the presence of intrinsic Fe species (about 744 mg kg^{-1}). Fe not only facilitates the formation of catalytically active N—C sites but also increases the graphitization degree of carbon. Another possible reason is that trace levels of Fe residues (0.07 wt%) in carbon can dramatically enhance the ORR properties.

In fact, controversy still exists over whether metal ions can function as active sites or just facilitate the formation of active sites. An understanding of active sites has been gained from experimental data and theoretical calculations [71]. An in situ poisoning experiment confirmed the existence of a metal-centered active site. For example, in the presence of CN^-, the redox couple of Co(III)/Co(II) dramatically changed because CN^- coordinated with the transition metal in the axial position. The blocking effect prevented the interaction of O_2 with the transition metal and hence reduced the electrocatalytic activity [72]. Similarly, H_2S has also been used in an in situ poisoning experiment. A significant deactivation of Fe—N—C catalysts for ORR was observed after the H_2S treatment due to the formation of Fe—S bonds. In addition, the XPS characterization indicated the existence of Fe—S type bonds. These results showed that Fe was indeed active sites in catalyzing ORR [73].

The experimental results indeed proved that trace metal residues enhanced the ORR activity. Here comes the question: "How metal-free are metal-free catalysts?" [68]. Pumera and coworkers investigate the electrochemical response of carbon nanotubes with different metallic impurities. They found that 100 ppm of Fe impurities (close to the detection limit) still dominated the electrochemical behavior of a CNT sample [74]. Therefore, definitive proof of metal-free catalysts is necessary. In addition, we highly suggest that there is no need to argue whether trace metal residue promotes the ORR activity. The abovementioned results clarify this.

http://dx.doi.org/10.5772/intechopen.77048

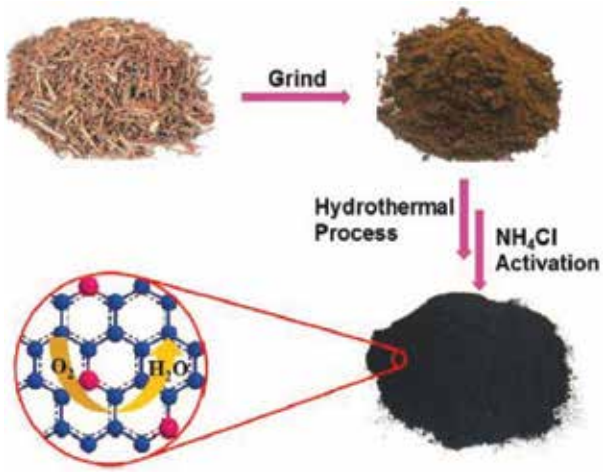

Figure 5. Schematic procedure for the synthesis of heteroatom doped porous carbon materials derived from Gentiana scabra Bunge [70].

Trace metal as active sites in ORR depending more on the nanostructure of carbon matrix. It is time to take the step forward toward exploration of ORR electrocatalyst with uniform open cavities and ordering distribution of the trace metal.

3. Conclusion(s)

Cathode catalysts meet the criteria of promising ORR performance, high stability, high durability, and low cost and are highly desirable for automotive applications. The development of novel strategies for the rational design and synthesis of catalysts for meeting these performance goals is very important. Furthermore, it is significantly important to develop a theoretical and experiment-based in-depth understanding of the nature of active sites together with the underlying mechanism of the ORR. Close attention should be paid to catalysts with high ORR activities under alkaline, acidic, and neutral conditions.

Metal atoms, metal alloys, metal oxide/nitride/sulfide nanoparticles, non-metal heteroatoms (e.g., N, S, B, and P), and even topological defects and edges of the carbon support can serve as potential active sites. Assisted by theoretical calculations, the catalytic mechanism of the ORR can be easily predicted; thus, the rational design and synthesis of catalysts become more efficient. In addition, the composition, size, dispersion, morphology, and structure of the nanoparticles, the contents of the heteroatoms, as well as the nanostructure of the carbon support are probably influential in the ORR. Therefore, the precise control of the structure, electronic state, and density of the active sites at the atomistic level are favorable for achieving an optimum ORR performance. Probing the role of trace metals in the ORR further guides future research activities, thereby reducing the cost and dramatically improving the ORR performance.

For practical applications, the reduction in the cost of electrocatalyst is an important factor. Future studies should focus on the design and synthesis of platinum group metal (PGM)-free cathode catalysts achieving high efficiency and durability along with low costs. The 2020 target for PGM-free catalyst activity proposed by the Department of Energy (DOE) is to achieve 0.044 A/cm^2 @ 0.9 $V_{IR\text{-}free}$ and a durability of 5000 h [75]. Overall, a bright future awaits for cathode catalysts.

Acknowledgements

This work was supported by the National Nature Science Foundation of China (no. 21603156), Jiangsu Province Science Foundation for Youths (no. BK20170331).

Acronyms and abbreviations

ORR	Oxygen reduction reaction
PEM	Proton exchange membrane
Pt/C	Platinum/carbon black catalyst
CB	Carbon black
CNT	Carbon nanotube
XPS	X-ray photoelectron spectroscopy

Author details

Winston Duo Wu and Dan Xu*

*Address all correspondence to: dxu@suda.edu.cn

Jiangsu Key Laboratory of Advanced Functional Polymer Design and Application, Department of Polymer Science and Engineering, College of Chemistry, Chemical Engineering and Materials Science, Soochow University, Suzhou, China

References

[1] Shao MH, Chang QW, Dodelet JP, Chenitz R. Recent advances in Electrocatalysts for oxygen reduction reaction. Chemical Reviews. 2016;**116**:3594-3657. DOI: 10.1021/acs.chemrev.5b00462

[2] Qiao M, Tang C, Tanase LC, Teodorescu CM, Chen CM, Zhang Q, Titirici MM. Oxygenophilic ionic liquids promote the oxygen reduction reaction in Pt-free carbon electrocatalysts. Materials Horizons. 2017;**4**:895-899. DOI: 10.1039/c7mh00298j

[3] Zagal JH, Koper MTM. Reactivity descriptors for the activity of molecular MN4 catalysts for the oxygen reduction reaction. Angewandte Chemie, International Edition. 2016;**55**:14510-14521. DOI: 10.1002/anie.201604311

[4] Zhang GR, Munoz M, Etzold BJM. Accelerating oxygen-reduction catalysts through preventing poisoning with non-reactive species by using hydrophobic ionic liquids. Angewandte Chemie, International Edition. 2016;**55**:2257-2261. DOI: 10.1002/anie.201508338

[5] Sui S, Wang XY, Zhou XT, Suc YH, Riffatc S, Liu CJ. A comprehensive review of Pt electrocatalysts for oxygen reduction reaction: Nanostructure, activity, mechanism and carbon support in PEM fuel cells. Journal of Materials Chemistry A. 2017;**5**:1808-1825. DOI: 10.1039/c6ta08580f

[6] Yang X, Roling LT, Vara M, Elnabawy AO, Zhao M, Hood ZD, Bao SX, Mavrikakis M, Xia Y. Synthesis and characterization of Pt−Ag alloy nanocages with enhanced activity and durability toward oxygen reduction. Nano Letters. 2016;**16**:6644-6649. DOI: 10.1021/acs.nanolett.6b03395

[7] Zhou YZ, Yang J, Zhu CZ, Du D, Cheng XN, Yen CH, Wai CM, Lin YH. Newly designed graphene cellular monolith functionalized with hollow Pt-M (M = Ni, Co) nanoparticles as the electrocatalyst for oxygen reduction reaction. ACS Applied Materials & Interfaces. 2016;**8**:25863-25874. DOI: 10.1021/acsami.6b04963

[8] Jiang KZ, Shao Q, Zhao DD, Bu LZ, Guo J, Huang XQ. Phase and composition tuning of 1D platinum-nickel nanostructures for highly efficient electrocatalysis. Advanced Functional Materials. 2017;**27**:1700830. DOI: 10.1002/adfm.201700830

[9] Jia QY, Ghoshal S, Li JK, Liang WT, Meng GN, Che HY, Zhang SM, Mad ZF, Mukerjee S. Metal and metal oxide interactions and their catalytic consequences for oxygen reduction reaction. Journal of the American Chemical Society. 2017;**139**:7893-7903. DOI: 10.1021/jacs.7b02378

[10] Tian XL, Luo JM, Nan HX, Zou HB, Chen R, Shu T, Li XH, Li YW, Song HY, Liao SJ, Adzic RR. Transition metal nitride coated with atomic layers of Pt as a low-cost, highly stable electrocatalyst for the oxygen reduction reaction. Journal of the American Chemical Society. 2016;**138**:1575-1583. DOI: 10.1021/jacs.5b11364

[11] Du L, Du CY, Chen GY, Kong FP, Yin GP, Wang Y. Metal-organic coordination networks: Prussian blue and its synergy with Pt nanoparticles to enhance oxygen reduction kinetics. ACS Applied Materials & Interfaces. 2016;**8**:15250-15257. DOI: 10.1021/acsami.6b02630

[12] Tong XL, Chen S, Guo CX, Xia XH, Guo XY. Mesoporous $NiCo_2O_4$ nanoplates on three-dimensional graphene foam as an efficient electrocatalyst for the oxygen reduction

reaction. ACS Applied Materials & Interfaces. 2016;**8**:28274-28282. DOI: 10.1021/acsami.5b10044

[13] Xia Z, An L, Chen P, Xia D. Non-Pt nanostructured catalysts for oxygen reduction reaction: Synthesis, catalytic activity and its key factors. Advanced Energy Materials. 2016;**1600458**:1-29. DOI: 10.1002/aenm.201600458

[14] Paraknowitsch JP, Thomas A. Doping carbons beyond nitrogen: An overview of advanced heteroatom doped carbons with boron, sulphur and phosphorus for energy applications. Energy & Environmental Science. 2013;**6**:2839-2855. DOI: 10.1039/c3ee41444b

[15] Perivoliotis DK, Tagmatarchis N. Recent advancements in metal-based hybrid electrocatalysts supported on graphene and related 2D materials for the oxygen reduction reaction. Carbon. 2017;**118**:493-510. DOI: 10.1016/j.carbon.2017.03.073

[16] Hu PG, Liu K, Deming CP, Chen SW. Multifunctional graphene-based nanostructures for efficient electrocatalytic reduction of oxygen. Journal of Chemical Technology and Biotechnology. 2015;**90**:2132-2151. DOI: 10.1002/jctb.4797

[17] Lee WJ, Maiti UN, Lee JM, Lim J, Han TH, Kim SO. Nitrogen-doped carbon nanotubes and graphene composite structures for energy and catalytic applications. Chemical Communications. 2014;**50**:6818-6830. DOI: 10.1039/c4cc00146j

[18] He YF, Gehrig D, Zhang F, Lu CB, Zhang C, Cai M, Wang YY, Laquai F, Zhuang XD, Feng XL. Highly efficient electrocatalysts for oxygen reduction reaction based on 1D ternary doped porous carbons derived from carbon nanotube directed conjugated microporous polymers. Advanced Functional Materials. 2016;**26**:8255-8265. DOI: 10.1002/adfm.201603693

[19] Zhu CZ, Li H, Fu SF, Du D, Lin YH. Highly efficient nonprecious metal catalysts towards oxygen reduction reaction based on three-dimensional porous carbon nanostructures. Chemical Society Reviews. 2016;**45**:517-531. DOI: 10.1039/c5cs00670h

[20] Tang C, Wang HF, Chen X, Li BQ, Hou TZ, Zhang BS, Zhang Q, Titirici MM, Wei F. Topological defects in metal-free nanocarbon for oxygen electrocatalysis. Advanced Materials. 2016;**28**:6845-6851. DOI: 10.1002/adma.201601406

[21] Tang C, Zhang Q. Nanocarbon for oxygen reduction electrocatalysis: Dopants, edges, and defects. Advanced Materials. 2017;**29**:1604103. DOI: 10.1002/adma.201604103

[22] Suna T, Tian BB, Lu J, Su CL. Recent advances of Fe (or co)/N/C electrocatalysts for oxygen reduction reaction in polymer electrolyte membrane fuel cells. Journal of Materials Chemistry A. 2017;**5**:18933-18950. DOI: 10.1039/c7ta04915c

[23] Fu SF, Zhu CZ, Song JH, Du D, Lin YH. Metal-organic framework-derived non-precious metal nanocatalysts for oxygen reduction reaction. Advanced Energy Materials. 2017;**7**:1700363. DOI: 10.1002/aenm.201700363

[24] He DS, He DP, Wang J, Lin Y, Yin PQ, Hong X, Wu YE, Li YD. Ultrathin icosahedral Pt-enriched nanocage with excellent oxygen reduction reaction activity. Journal of the American Chemical Society. 2016;**138**:1494-1497. DOI: 10.1021/jacs.5b12530

[25] Gimenez-Lopez MC, Kurtoglu A, Walsh DA, Khlobystov AN. Extremely stable platinum-amorphous carbon electrocatalyst within hollow graphitized carbon nanofibers for the oxygen reduction reaction. Advanced Materials. 2016;**28**:9103-9108. DOI: 10.1002/adma.201602485

[26] Jia QY, Ghoshal S, Li JK, Liang WT, Meng GN, Che HY, Zhang SM, Ma ZF, Mukerjee S. Metal and metal oxide interactions and their catalytic consequences for oxygen reduction reaction. Journal of the American Chemical Society. 2017;**139**:7893-7903. DOI: 10.1021/jacs.7b02378

[27] Huang HW, Li K, Chen Z, Luo LH, Gu YQ, Zhang DY, Ma C, Si R, Yang JL, Peng ZM, Zeng J. Achieving remarkable activity and durability toward oxygen reduction reaction based on ultrathin Rh-doped Pt nanowires. Journal of the American Chemical Society. 2017;**139**:8152-8159. DOI: 10.1021/jacs.7b01036

[28] Wang BW, Wang XX, Zou JX, Yan YC, Xie SH, Hu GZ, Li YG, Dong AG. Simple-cubic carbon frameworks with atomically dispersed iron dopants toward high-efficiency oxygen reduction. Nano Letters. 2017;**17**:2003-2009. DOI: 10.1021/acs.nanolett.7b00004

[29] Ren SB, Wang J, Xia XH. Highly efficient oxygen reduction electrocatalyst derived from a new three-dimensional polyporphyrin. ACS Applied Materials & Interfaces. 2016;**8**:25875-25880. DOI: 10.1021/acsami.6b05560

[30] Chen PZ, Zhou TP, Xing LL, Xu K, Tong Y, Xie H, Zhang LD, Yan WS, Chu WS, Wu CZ, Xie Y. Atomically dispersed iron–nitrogen species as electrocatalysts for bifunctional oxygen evolution and reduction reactions. Angewandte Chemie, International Edition. 2017;**56**:610-614. DOI: 10.1002/anie.201610119

[31] Kim JH, Sa YJ, Jeong HY, Joo SH. Roles of Fe−Nx and Fe−Fe_3C@C species in Fe−N/C electrocatalysts for oxygen reduction reaction. ACS Applied Materials & Interfaces. 2017;**9**:9567-9575. DOI: 10.1021/acsami.6b13417

[32] Sa YJ, Seo DJ, Woo JW, Lim JT, Cheon JY, Yang SY, Lee JM, Kang DW, Shin TJ, Shin HS, Jeong HY, Kim CS, Kim MG, Kim TY, Joo SH. A general approach to preferential formation of active Fe−Nx sites in Fe−N/C electrocatalysts for efficient oxygen reduction reaction. Journal of the American Chemical Society. 2016;**138**:15046-15056. DOI: 10.1021/jacs.6b09470

[33] Wang HT, Wang W, Xu YY, Dong S, Xiao JW, Wang F, Liu HF, Xia BY. Hollow nitrogen-doped carbon spheres with Fe_3O_4 nanoparticles encapsulated as a highly active oxygen-reduction catalyst. ACS Applied Materials & Interfaces. 2017;**9**:10610-10617. DOI: 10.1021/acsami.6b15392

[34] Xiao JW, Xia YT, Hu CC, Xi JGB, Wang S. Raisin bread-like iron sulfides/nitrogen and sulfur dual-doped mesoporous graphitic carbon spheres: A promising electrocatalyst for the oxygen reduction reaction in alkaline and acidic media. Journal of Materials Chemistry A. 2017;**5**:11114-11123. DOI: 10.1039/c7ta02096a

[35] Hu K, Tao L, Liu DD, Huo J, Wang SY. Sulfur-doped Fe/N/C nanosheets as highly efficient electrocatalysts for oxygen reduction reaction. ACS Applied Materials & Interfaces. 2016;**8**:19379-19385. DOI: 10.1021/acsami.6b02078

[36] Zhang JW, Xu D, Wang CC, Guo JG, Yan F. Rational design of $Fe_{1-x}S/Fe_3O_4$/nitrogen and sulfur-doped porous carbon with enhanced oxygen reduction reaction catalytic activity. Advanced Materials Interfaces. 2018;**5**:1701641. DOI: 10.1002/admi.201701641

[37] Yu HY, Fisher A, Cheng DJ, Cao DP. Cu,N-codoped hierarchical porous carbons as electrocatalysts for oxygen reduction reaction. ACS Applied Materials & Interfaces. 2016;**8**:21431-21439. DOI: 10.1021/acsami.6b04189

[38] Volosskiy B, Fei HL, Zhao Z, Lee S, Li MF, Lin ZY, Papandrea B, Wang C, Huang Y, Duan XF. Tuning the catalytic activity of a metal-organic framework derived copper and nitrogen co-doped carbon composite for oxygen reduction reaction. ACS Applied Materials & Interfaces. 2016;**8**:26769-26774. DOI: 10.1021/acsami.6b08320

[39] Tong Y, Chen PZ, Zhou TP, Xu K, Chu WS, Wu CZ, Xie Y. A bifunctional hybrid electrocatalyst for oxygen reduction and evolution: Cobalt oxide nanoparticles strongly coupled to B,N-decorated graphene. Angewandte Chemie, International Edition. 2017;**56**:1-6. DOI: 10.1002/anie.201702430

[40] Xu D, Xie Y, Song YJ, Deng WQ. A green and facile method toward synthesis of waste paper-derived 3D functional porous graphene via in situ activation of cobalt(II). Journal of Materials Chemistry A. 2015;**3**:16072-16078. DOI: 10.1039/c5ta03220b

[41] Yin PQ, Yao T, Wu Y, Zheng LR, Lin Y, Liu W, Ju HX, Zhu JF, Hong X, Deng ZX, Zhou G, Wei SQ, Li YD. Single cobalt atoms with precise N-coordination as superior oxygen reduction reaction catalysts. Angewandte Chemie, International Edition. 2016;**55**:10800-10805. DOI: 10.1002/anie.201604802

[42] Li B, Nam H, Zhao J, Chang J, Lingappan N, Yao F, Lee TH, Lee YH. Nanoreactor of nickel-containing carbon–shells as oxygen reduction catalyst. Advanced Materials. 2017;**29**:1605083. DOI: 10.1002/adma.201605083

[43] Schöfberger W, Faschinger F, Chattopadhyay S, Bhakta S, Mondal B, Elemans JAAW, Müllegger S, Tebi S, Koch R, Klappenberger F, Paszkiewicz M, Barth JV, Rauls E, Aldahhak H, Schmidt WG, Dey A. A bifunctional electrocatalyst for oxygen evolution and oxygen reduction reactions in water. Angewandte Chemie, International Edition. 2016;**55**:2350-2355. DOI: 10.1002/anie.201508404

[44] Song P, Luo M, Liu XZ, Xing W, Xu WL, Jiang Z, Gu L. Zn single atom catalyst for highly efficient oxygen reduction reaction. Advanced Functional Materials. 2017;**27**:1700802. DOI: 10.1002/adfm.201700802

[45] Ma M, You SJ, Wang W, Liu GS, Qi DP, Chen XD, Qu JH, Ren NQ. Biomass-derived porous fe_3c/tungsten carbide/graphitic carbon nanocomposite for efficient electrocatalysis of oxygen reduction. ACS Applied Materials & Interfaces. 2016;**8**:32307-32316. DOI: 10.1021/acsami.6b10804

[46] Wei C, Feng ZX, Scherer GG, Barber J, Shao-Horn Y, Xu ZJ. Cations in octahedral sites: A descriptor for oxygen electrocatalysis on transition-metal spinels. Advanced Materials. 2017;**29**:1606800. DOI: 10.1002/adma.201606800

[47] Xue HR, Tang J, Gong H, Guo H, Fan XL, Wang T, He JP, Yamauchi Y. Fabrication of PdCo bimetallic nanoparticles anchored on three-dimensional ordered N-doped porous carbon as an efficient catalyst for oxygen reduction reaction. ACS Applied Materials & Interfaces. 2016;**8**:20766-20771. DOI: 10.1021/acsami.6b05856

[48] Chen Y, Chen Y, Ding D, Ding Y, Choi YM, Zhang L, Yoo S, Chen DC, deGlee B, Xu H, Lu QY, Zhao B, Vardar GL, Wang JY, Bluhm H, Crumlin EJ, Yang CH, Liu J, Yildiz B, Liu ML. A robust and active hybrid catalyst for facile oxygen reduction in solid oxide fuel cells. Energy & Environmental Science. 2017;**10**:964-971. DOI: 10.1039/c6ee03656b

[49] He B, Ren ZJ, Qi CZ, Yan SK, Wang ZH. Synthesis of nitrogen-doped monolayer graphene with high transparent and n-type electrical properties. Journal of Materials Chemistry C. 2015;**3**:6172-6177. DOI: 10.1039/C5TC01046B

[50] Li OL, Chiba S, Wada Y, Panomsuwan G, Ishizaki T. Synthesis of graphitic-N and amino-N in nitrogendoped carbon via a solution plasma process and exploration of their synergic effect for advanced oxygen reduction reaction. Journal of Materials Chemistry A. 2017;**5**:2073-2082. DOI: 10.1039/c6ta08962c

[51] Cui XY, Yang SB, Yan XX, Leng JG, Shuang S, Ajayan PM, Zhang ZJ. Pyridinic-nitrogen-dominated graphene aerogels with Fe-N-C coordination for highly efficient oxygen reduction reaction. Advanced Functional Materials. 2016;**26**:5708-5717. DOI: 10.1002/adfm.201601492

[52] Yu HJ, Shang L, Bian T, Shi R, Waterhouse GIN, Zhao YF, Zhou C, Wu LZ, Tung CH, Zhang T. Nitrogen-doped porous carbon nanosheets templated from g-C_3N_4 as metal-free electrocatalysts for efficient oxygen reduction reaction. Advanced Materials. 2016;**28**:5080-5086. DOI: 10.1002/adma.201600398

[53] Li Q, Xu D, Guo JN, Ou X, Yan F. Protonated g-C_3N_4@polypyrrole derived N-doped porous carbon for supercapacitors and oxygen electrocatalysis. Carbon. 2017;**124**:599-610. DOI: 10.1016/j.carbon.2017.09.029

[54] Li Q, Xu D, Ou X, Yan F. Nitrogen-doped graphitic porous carbon nanosheets derived from in situ formed g-C_3N_4 templates for the oxygen reduction reaction. Chemistry, an Asian Journal. 2017;**12**:1816-1823. DOI: 10.1002/asia.201700586

[55] Panomsuwan G, Saito N, Ishizaki T. Nitrogen-doped carbon nanoparticle–carbon nanofiber composite as an efficient metal-free cathode catalyst for oxygen reduction reaction. ACS Applied Materials & Interfaces. 2016;**8**:6962-6971. DOI: 10.1021/acsami.5b10493

[56] Zhu X, Zhu YH, Tian CC, Jin T, Yang XJ, Jin XB, Li CZ, Wang HL, Liu HL, Dai S. Pyrolysis of conjugated nanoporous polycarbazoles to mesoporous N-doped carbon nanotubes as efficient electrocatalysts for the oxygen reduction reaction. Journal of Materials Chemistry A. 2017;**5**:4507-4512. DOI: 10.1039/c6ta09604b

[57] He B, Liu F, Yan S. Temperature-directed growth of highly pyridinic nitrogen doped, graphitized, ultra-hollow carbon frameworks as an efficient electrocatalyst for the oxygen reduction reaction. Journal of Materials Chemistry A. 2017;**5**:18064-18070. DOI: 10.1039/c7ta04685e

[58] Hu CG, Dai LM. Multifunctional carbon-based metal-free electrocatalysts for simultaneous oxygen reduction, oxygen evolution, and hydrogen evolution. Advanced Materials. 2017;**29**:1604942. DOI: 10.1002/adma.201604942

[59] Zhang JT, Qu LT, Shi GQ, Liu JY, Chen JF, Dai LM. N,P-Codoped carbon networks as efficient metal-free bifunctional catalysts for oxygen reduction and hydrogen evolution reactions. Angewandte Chemie, International Edition. 2016;**55**:2230-2234. DOI: 10.1002/anie.201510495

[60] Mulyadi A, Zhang Z, Dutzer M, Liu W, Deng YL. Facile approach for synthesis of doped carbon electrocatalyst from cellulose nanofibrils toward high-performance metal-free oxygen reduction and hydrogen evolution. Nano Energy. 2017;**32**:336-346. DOI: 10.1016/j.nanoen.2016.12.057

[61] Pei ZX, Gu JX, Wang YK, Tang ZJ, Liu ZX, Huang Y, Huang Y, Zhao JX, Chen ZF, Zhi CY. Component matters: Paving the roadmap toward enhanced electrocatalytic performance of graphitic C_3N_4-based catalysts via atomic tuning. ACS Nano. 2017;**11**:6004-6014. DOI: 10.1021/acsnano.7b01908

[62] Banks CE, Crossley A, Salter C, Wilkins SJ, Compton RG. Carbon nanotubes contain metal impurities which are responsible for the "Electrocatalysis" seen at some nanotube-modified electrodes. Angewandte Chemie, International Edition. 2006;**45**:2533. DOI: 10.1002/anie.200600033

[63] Wong CHA, Chua CK, Khezri B, Webster RD, Pumera M. Graphene oxide nanoribbons from the oxidative opening of carbon nanotubes retain electrochemically active metallic impurities. Angewandte Chemie, International Edition. 2013;**52**:8685. DOI: 10.1002/anie.201303837

[64] Guo ZY, Jiang CC, Teng C, Ren GY, Zhu Y, Jiang L. Sulfur, trace nitrogen and iron codoped hierarchically porous carbon foams as synergistic catalysts for oxygen reduction reaction. ACS Applied Materials & Interfaces. 2014;**6**:21454-21460. DOI: 10.1021/am506459f

[65] Liu SF, Han LL, Zhu J, Xiao WP, Wang J, Liu HF, Xin HL, Wang DL. Enhanced electrocatalytic activity and stability of Pd_3V/C nanoparticles with a trace amount of Pt decoration for the oxygen reduction reaction. Journal of Materials Chemistry A. 2015;**3**:20966-20972. DOI: 10.1039/c5ta05202e

[66] Lu BA, Sheng T, Tian N, Zhang ZC, Xiao C, Cao ZM, Ma HB, Zhou ZY, Sun SG. Octahedral PtCu alloy nanocrystals with high performance for oxygen reduction reaction and their enhanced stability by trace Au. Nano Energy. 2016;**33**:65-71. DOI: 10.1016/j.nanoen.2017.01.003

[67] Wang DL, Liu SF, Wang J, Lin RQ, Kawasaki M, Rus E, Silberstein KE, Lowe MA, Lin F, Nordlund D, Liu HF, Muller DA, Xin HL, Abrunña HD. Spontaneous incorporation of gold in palladium-based ternary nanoparticles makes durable electrocatalysts for oxygen reduction reaction. Nature Communications. 2016;**7**:11941. DOI: 10.1038/ncomms11941

[68] Masa J, Zhao AQ, Xia W, Sun ZY, Mei B, Muhler M, Schuhmann W. Trace metal residues promote the activity of supposedly metal-free nitrogen-modified carbon catalysts for the oxygen reduction reaction. Electrochemistry Communications. 2013;**34**:113-116. DOI: 10.1016/j.elecom.2013.05.032

[69] Wang L, Ambrosi A, Pumera M. "Metal-free" catalytic oxygen reduction reaction on heteroatom-doped graphene is caused by trace metal impurities. Angewandte Chemie, International Edition. 2013;**52**:13818-13821. DOI: 10.1002/anie.201309171

[70] Wang CC, Wu WD, Wang Y, Xu D, Yan F. Nitrogen doped carbon materials derived from Gentiana scabra Bunge as high-performance catalysts for the oxygen reduction reaction. New Journal of Chemistry. 2017;**41**:7392-7399. DOI: 10.1039/c7nj01178d

[71] Malko D, Kucernak A, Lopes T. Performance of Fe-N/C oxygen reduction Electrocatalysts toward NO_2-, NO, and NH_2OH electroreduction: From fundamental insights into the active center to a new method for environmental nitrite destruction. Journal of the American Chemical Society. 2016;**138**:16056-16068. DOI: 10.1021/jacs.6b09622

[72] Gupta S, Fierro C, Yeager E. The effects of cyanide on the electrochemical properties of transition-metal macrocycles for oxygen reduction in alkaline-solutions. Journal of Electroanalytical Chemistry. 1991;**306**:239-250. DOI: 10.1016/0022-0728(91)85233-F

[73] Singh D, Mamtani K, Bruening CR, Miller JT, Ozkan US. Use of H_2S to probe the active sites in FeNC catalysts for the oxygen reduction reaction (ORR) in acidic media. ACS Catalysis. 2014;**4**:3454-3462. DOI: 10.1021/cs500612k

[74] Pumera M, Miyahara Y. What amount of metallic impurities in carbon nanotubes is small enough not to dominate their redox properties? Nanoscale. 2009;**1**:260-265. DOI: 10.1039/b9nr00071b

[75] Fuel Cell Technologies Office Multi-Year Research, Development, and Demonstration Plan. November 2016. https://www.energy.gov/sites/prod/files/2017/05/f34/fcto_myrdd_fuel_cells.pdf

Chapter 4

Noble Metal Dispersed on Reduced Graphene Oxide and Its Application in PEM Fuel Cells

Adriana Marinoiu, Mircea Raceanu, Elena Carcadea, Aida Pantazi, Raluca Mesterca, Oana Tutunaru, Simona Nica, Daniela Bala, Mihai Varlam and Marius Enachescu

Additional information is available at the end of the chapter

http://dx.doi.org/10.5772/intechopen.80941

Abstract

Metal-dispersed nanoparticles on reduced graphene oxide as catalyst for oxygen reduction reaction (ORR) demonstrate promising applications in the energy sector. The catalyst activity enhancement and stability improvement investigated in this study are mandatory steps in obtaining feasible electrodes for PEMFC. The chapter deals with the synthesis of noble metal catalysts including platinum and gold nanoparticles dispersed on reduced graphene oxide (PtNPs/rGO and AuNPs/rGrO). The understanding of the correlations between the electrochemical activity on one side and the structure, composition and synthesis method on the other side are provided. Facile routes in order to prepare the well dispersed PtNPs/rGO and AuNPs/rGrO are included. The structure and morphology were characterized by different techniques, namely X-ray diffraction (XRD), Scanning Transmission Electron Microscopy (STEM), specific surface area measurements. In this context we report a hybrid derived electrocatalyst with increased electrochemical active area and enhanced mass-transport properties. The electrochemical performances of PtNPs/rGO and AuNPs/rGrO were tested and compared with a standard PEMFC configuration. The performed electrochemical characterization recommends the prepared materials as ORR electrocatalysts for the further fabrication of cathodes for PEM fuel cells. The research directions as well as perspectives on the subsequent development of more active and less expensive electrocatalysts are established.

Keywords: fuel cell, cathode, doped graphenes, oxygen reduction reaction

1. Introduction

Almost 60 years have passed from Feynman's famous and incredible visionary talk "There is plenty of room at the bottom" and many of his statements are the reality today. The new field he was just introducing was defined as having an enormous number of technical applications. And so right he was! In this chapter, we are going to discuss one of those applications. Fuel cells are among the major scientific discoveries that had a strange "life". Despite their modern tech aura, the wonderful discovery of Mr. Grove, 150 years ago, had in the last 20 years an extremely variable popularity, reaching their peak at the end of the last century, when scientists and stock promoters envisioned a world run on clean and inexhaustible resource—hydrogen. At that time, it was predicted that soon, cars will run on fuel cells and households will generate electricity from back-yard fuel cells. Improvements in stack design during that time led to increased power densities and lower costs. However, high manufacturing costs, marginal performance and short service life stood in the way of turning the hydrogen dream into reality. Nowadays, a new "wave" has emerged, partly due to exactly the new field introduced by Mr. Feynman—nanostructure-based catalysts.

The development of human society requires more resources to meet the enhanced energy demand of society. With the rapid increase in energy demand in people's everyday lives, research into new environment-friendly energy sources and their practical applications have attracted increasing attention. Fuel cells demonstrated important advantages with distinguishing features compared to conventional power sources, such as internal combustion engines or batteries, namely: higher efficiency and silent operation in comparison to internal combustion engines; no pollution considering the only by-product at the point of use is water; the maintenance of fuel cells is simple; low temperature proton exchange fuel cells (PEMFC) have low heat transmission; operating time is much longer than in the case of batteries, since doubling the operating time needs only doubling the content of fuel and not the doubling of the capacity of the unit itself; as opposed to batteries, fuel cells have no "memory effect" when are replenished.

The main advantages of new nanostructured materials are their very high surface area to volume ratio and high absorption rates. There are nanoscale materials of various types, including nanoparticles, nano-powders, nano-rods, nanotubes, and nanowires. It is well known that nanomaterials have multiple dimensionalities, including zero dimensional, 1-D, 2-D and 3-D. One dimensional materials are widely used in various applications because of their high surface area and porosity. Carbon-type materials are known to have good features, such as abundance, stability, environmental safety and high durability. They exhibit high chemical stability over a wide temperature range in both acidic and alkaline conditions, making them the most suitable candidates for electrodes in electrochemical energy devices. There are many available carbon allotropes, such as buckminster fullerenes, carbon nanotubes, graphene and nano-diamonds. In the last years, graphene is considered as a major material in energy conversion and storage applications in general and in PEM fuel cells topic particularly. Therefore, one of the cornerstones of the push towards future improvements in present-day PEM fuel cell, and the research and development generated by this push, is the introduction of nanostructured catalysts in order to mitigate the main issues of the technology—high prices and low service life.

http://dx.doi.org/10.5772/intechopen.80941

PEMFC cells are currently the leading technology for light duty vehicles and in a smaller proportion for stationary and other applications. Commercialization of light duty FC vehicles started recently. The market for FC vehicles is still limited to the present day, mainly due to an insufficient hydrogen fueling infrastructure, but also to a considerable cost of FC systems able to achieve the target lifetime [1, 2]. For example, it is recognized that a decrease in platinum loading has a negative impact in respect to durability. In this particular domain of catalyst durability for FC systems the smetal-dispersed nanoparticles can concurrently lower the catalytic system cost playing a significant role in technology developments in the near future [3]. Moreover, most of the researches have been devoted to reduce the resistance of the electrolyte membrane by lowering the thickness, which caused inferior mechanical properties of the thinned membrane.

The total cost of a fuel cells stack can be greatly reduced by reducing the catalyst load and using low- or non-Pt-based electrocatalysts. Therefore, the ways to improve the catalytic activity and reduce the cost of anodic and cathodic catalysis are critical issues to achieve the real fueling of the fuel cells. In PEM fuel cells, the efficiency of the cathode electrocatalyst plays an important role in increasing energy conversion efficiency and achieving higher power densities. In recent years, new 3D graphene-based materials have been developed, that have proved to be effective electrocatalysts for ORR [4]. The main directions for increasing the catalytic activity and reducing the production costs for the ORR catalysts were as follows: the development of nano-graphene nanostructures based on noble metals, either by doping with non-metals or by the deposition of non-metallic nanoparticles or metallic oxides with a catalytic role; decreasing the noble metal content of the electrocatalyst.

In recent years, various catalyst support materials have been proposed to meet the challenges. In addition to traditional carbon materials, non-carbon materials such as metal oxides, electroconducting polymers, carbides, nitrides, etc. have been proposed and sustained as catalysts. The nanostructured materials meet the requirements of a high-surface catalyst with high active surface sites and a low metal load. Consequently, a number of non-metallic catalysts have been developed, but the catalytic performance has been modest [5, 6]. The ORR reaction at the cathode plays a critical role in the performance of a fuel cell. Although substantial advances have been made in cathodic catalysis over the last decades, the slow kinetics of ORR electron transfer and overpotential are the disadvantages that limit the large-scale marketing of PEMFC.

The porous graphene has remarkable properties for electrochemical power systems [7]. In general, nanoelectrocatalysts based on graphene used in PEMFC can be classified into the following types, depending on the composition of the catalysts: (1) Pt-based nanocatalysts supported on graphene; (2) noble metals supported on graphene as electrocatalysts, including transition metals and their oxides, sulphide nanomaterials and metal complexes (3) Pt-free graphene-supported electrocatalysts, including alloys Pd, Au, Ag and nanomaterials; and (4) non-metal electrocatalysts, including surface functionalized graphene and heteroatom doped graphene. It should be noted that, despite the substantial advances made in the construction of advanced electrocatalysts based on graphene and the understanding of their electrocatalytic mechanism, a number of scientific and technical challenges still remain in order to achieve the commercialization of graphite-supported electrocatalysts in fuel cells. It is anticipated that graphene support nanomaterials are a promising class of fuel cell electrocatalysts.

The catalytic activity of the Pt graphene composites can be improved by increasing the charge transfer from the catalysts to the graphene substrate. The chemically functionalized graphene with interlayer structure contains network defects (bare spots, holes) and surface functional groups (carbonyls, epoxies, hydroxyls, etc.) that can bind metal nanoparticles and can retain them on the graphene surface. A strong metal–substrate interaction was demonstrated to enable the stability of the nanocatalyst, which can be improved by dispersion. Using Density Functional Theory (DFT) it was found that surface defects in the graphene support can also act as strong traps for Pt nanoclusters, leading to long-term stability of Pt graphene composites.

Metallic graphene hybrids have exhibited significant electrocatalytic activities when used as anodic and cathodic catalysts in PEM fuel cells. Both n- and p-type conductivities can be obtained by selecting metal dopants, and the carrier concentration can be controlled by the quantity of metal deposited [8]. For example, several transition metals with different work functions, such as Ti, Fe, Cu, Ag, Au, and Pt, have been used for graphene band modulation. In particular, band arrangement is not only determined by work function, but also affected by the interfacial interactions, as a consequence the metal structures would influence the charge transfer between metal and graphene. Moreover, first-principles calculations indicated that the carbon-vacancies attract and trap metal atoms [8]. The binding of a single metal atom nearby a single-vacancy (SV) on the graphene was investigated recently for Pt, Pd, Au, and Sn, using the density-functional theory (DFT). Regarding the pristine graphene, Pt, Pd, and Sn prefer to be adsorbed at the bridge site, while Au prefers the top site. On the single-vacancy graphene, all the metal atoms prefer to be trapped at the vacancy site and appear as dopants. The trapping abilities of the SV-graphene for different metal atoms, are different, that is, the Pt and Pd have the larger trapping zones. The diffusion barrier of a metal atom on the SV-graphene is much higher than that on the pristine graphene, and the Pt atom has the highest diffusion barrier from the SV site to the neighboring bridge sites. More electrons are transferred from the adatoms (or dopants) to the carbon atoms at the defect site, which induces changes in the electronic structures and properties of the systems. However, the Pt atom is easier to be incorporated into the SV-graphene [8].

In our previous efforts on the development of innovative fuel cell catalysts, an experimental approach of finding low cost alternative support material in PEMFC was developed [9]. The potential of using graphene oxide as support/catalyst for PEMFC was exploited. Moving forward, Pt/graphene nanocomposites were synthesized using a simple route involving chemical oxidation, exfoliation of graphene oxide, as well as functionalization with a compatible polymer. Poly-diallyldimethylammonium chloride (PDDA) was used as cationic polyelectrolyte, with ability of adsorption on the graphene surface through $\pi-\pi$ and electrostatic interactions, acting as a stabilizer for controlled synthesis of Pt/graphene [9, 10].

2. Experimental

2.1. Synthesis of graphene: noble metals nanocomposites

Graphite powder, $K_2S_2O_8$, P_2O_5, conc. H_2SO_4, $KMnO_4$, HI were purchased from Sigma-Aldrich, H_2O_2 and HCl were obtained from Oltchim SA Romania. The electrocatalysts were synthesized

via a facile process (**Figure 1**) described in detail elsewhere [11, 12]. Graphite oxide was prepared by the oxidation of graphite powder using P_2O_5, H_2SO_4, and $KMnO_4$ according to the Hummers' method, namely the graphitic powder was mixed with an oxidizing agent, filtered, washed and dried. Graphite oxide was dispersed in water by sonication for 2 h, forming the stable graphene oxide suspension (GO). Then, solutions of NaCl and the precursor of corresponding metal (water solutions of H_2PtCl_6 or $HAuCl_4$) were added individually to GO suspension under continuous mechanical stirring (500 rpm for 1 h).

Freshly prepared solution of $NaBH_4$ was added slowly to the reaction mixture under vigorous stirring. The reaction mixture was stirred for another 24 h for the complete reduction, then washed with large amount of water several times, separated by filtration and centrifugation in order to remove residual ions. The obtained mass was then dried. pH plays an important role in the obtaining of the metal dispersed rGO, therefore the values of this parameter were mentioned in the experimental part (**Figure 1**) during each proposed fabrication steps. Aqueous NaOH and HCl solutions were used to adjust the pH value. In this work, we took into consideration the preparation of highly dispersed platinum and gold nanoparticles on reduced Graphene Oxide nanosheets with different metal compositions: Pt/rGO_x and Au/rGO_y. It is known the fact that, during reduction step, graphene oxide gradually loses its oxygen-containing groups and could become hydrophobic, thus a direct reduction without a compatible polymer with ability of adsorption on the graphene surface, generally causes irreversible agglomerations. In our developed protocol synthesis PDDA was used as cationic polyelectrolyte owing to its expected reason of stabilizer effect, favoring the electrostatic interactions. Therefore, the bonding of reduced graphene oxide (rGO) with PDDA offers the possibility of controlling the behaviors of RGO in suspensions.

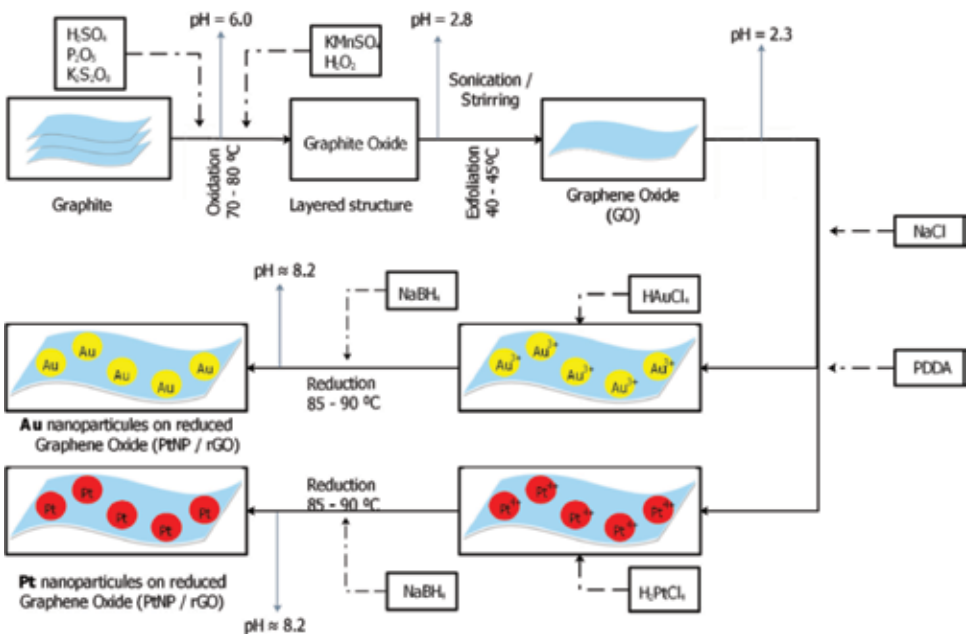

Figure 1. Reaction routes for the synthesis of metal nanoparticles on graphene oxide.

2.2. Catalysts characterization

The microstructure and morphology of prepared samples were evaluated by using the following techniques: Scanning Electron Microscopy (SEM), Scanning Transmission Electron Microscopy (STEM), specific surface area. Scanning Electron Microscopy (SEM) measurements were carried out using a Hitachi SU 8230 Scanning Electron Microscope equipped with EDS detector-analyzer. Hitachi HD 2700 Scanning Transmission Electron Microscope equipped with EDX Oxford detector-analyzer was used to perform graphene samples analysis. For the analysis, the samples in the form of powder were dispersed in bi-distilled water using a probe-type ultrasonic homogenizer and deposited on a standard Cu TEM grid. Also, EDX analysis was performed to determine the chemical composition of the samples. Autosorb IQ (Quantachrome, USA) instrumentation was used to perform the adsorption and desorption experiments at 77 K after initial pre-treatment of the samples by degassing at 115°C for 4 hours. The powder X-ray diffraction (XRD) analyses were performed at room temperature on a Rigaku SmartLab X Ray Diffractometer with Cu target $K_{\beta 1}$ = 1.39217 Å, $K_{\alpha 1}$ = 1.540598 Å and $K_{\alpha 2}$ = 1.544426 Å. The diffraction data was recorded for 2θ angles using the following parameters: tube voltage = 45 kV, tube current = 200 mA, scan range: 5–90°. The identification of the phase was made by referring to the International Center for Diffraction Data—ICDD (PDF-2) database.

2.3. Electrode preparation and electrochemical measurements

The modified carbon paste electrodes were prepared by mixing graphite powder with paraffin oil, then mixing in a mortar until a consistent uniformly wetted paste was obtained. The ratio of the two components was approximately 3:2 (w/w). The obtained paste was placed into a plastic syringe with an inner volume of 1.0 mL. The electrical contact was assured by a copper wire that was inserted into the back of the graphite paste. The modified electrodes were prepared by mixing certain amounts of carbon paste with platinum-doped reduced graphene oxide and gold-doped reduced graphene oxide in ratio of 109.7:0.3 and 109:1 (w/w), respectively. The obtained materials were pressed at the end of carbon paste from syringes. Thus, four electrodes were prepared: bare carbon paste electrode (CPE), graphene oxide modified carbon paste electrode (denoted by GO), platinum-doped reduced graphene oxide (denoted by Pt/rGO) and gold-doped reduced graphene oxide (denoted by Au/rGO). The surface of all electrodes was smoothed by polishing on a piece of weighing paper. Electrochemical measurements were carried out on a potentiostat/galvanostat system AutoLabPGStat 12, controlled by GPES (general purpose electrochemical system), electrochemical interface for Windows (version 4.9.007). Three electrodes in one compartment cell (10 mL) were used in all experiments. A glassy carbon electrode (Metrohm, 3 mm in diameter) and each modified carbon paste electrodes served as working electrodes. The counter electrode was a large area Pt wire. All experimental potentials were referred to Ag/AgCl, KCl_{sat} as reference electrode.

The electrochemical characterization of the modified carbon paste electrodes was carried out by cyclic voltammetry (CV) and differential pulse voltammetry (DPV). The CV experiments were recorded in 0.5 M KCl solution containing 1.0 mmol L^{-1} $K_3Fe(CN)_6$ in the potential range of (−0.35) to (+0.8) V at scan rates of 20–120 mV s^{-1}. DPV curves were recorded in the same potential domains with 5 mV potential and 25 mV as modulation amplitude.

3. Results and discussions

Firstly, the characterization of the prepared materials was performed to validate the microstructural quality and to confirm the metal presence and the structured morphology (**Figures 2** and **3**).

The crystalline structure of Pt/rGO_x and Au/rGO_y composites was characterized by X-ray diffraction (XRD). XRD patterns of prepared doped-graphene with Pt or Au nanoparticles are presented in **Figure 4**. The prepared materials exhibited characteristic diffraction peaks at 39.76° (38.18°), 46.24° (44.39°), 67.46° (64.58°), 81.29° (77.55°)corresponding to the (111), (200), (220), (311) planes of face-centered cubic structure of Pt (PDF Card 00-004-0802) and Au (PDF Card 00-004-0784), respectively. The diffraction peaks in all samples are also assigned to the structure of the graphene oxide support.

Based on the intensity of the main peaks from the XRD patterns and using on the Scherrer's equation, the mean crystallites sizes were computed: $D_{hkl} = K\lambda/B_{hkl}\cos\theta$, where D_{hkl} is the crystallite size in the direction perpendicular to the lattice planes (hkl), K is a constant related to crystallite shape, λ is the X-ray wavelength in nm, and B_{hkl} is the peak width at half-maximum peak height. The crystalline size estimated from the Scherrer equation is between 14 and 25 nm for Au/rGO and 7–15 nm for Pt/rGO.

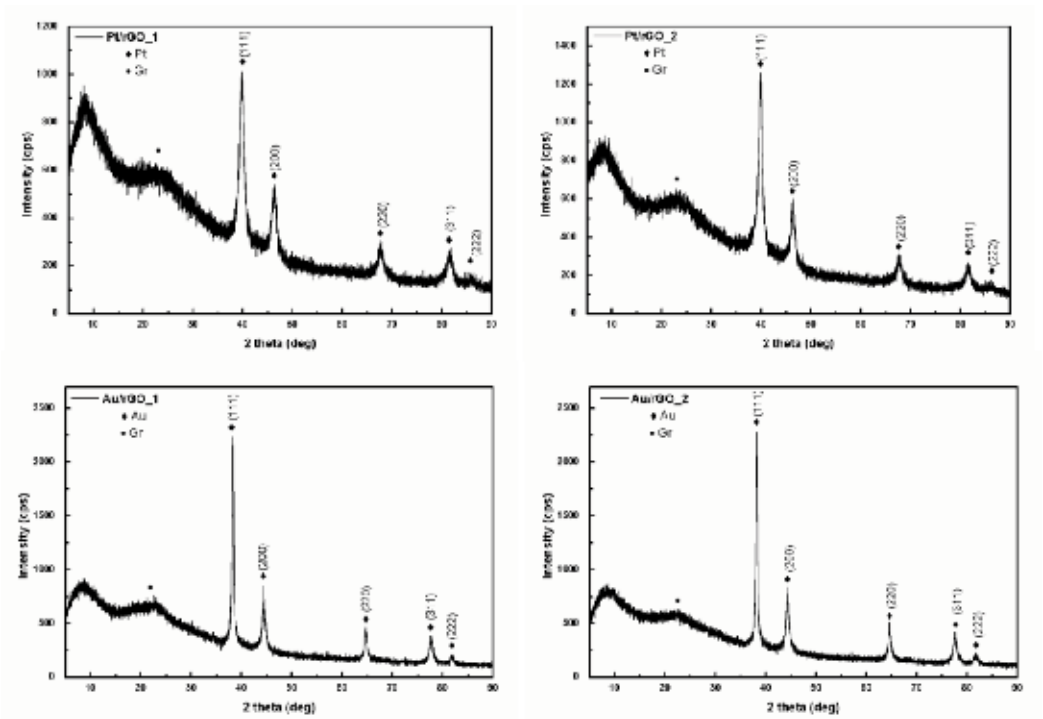

Figure 2. XRD patterns of metal-dispersed nanoparticles on reduced graphene oxide composites: Pt/rGO—up and Au/rGO—down.

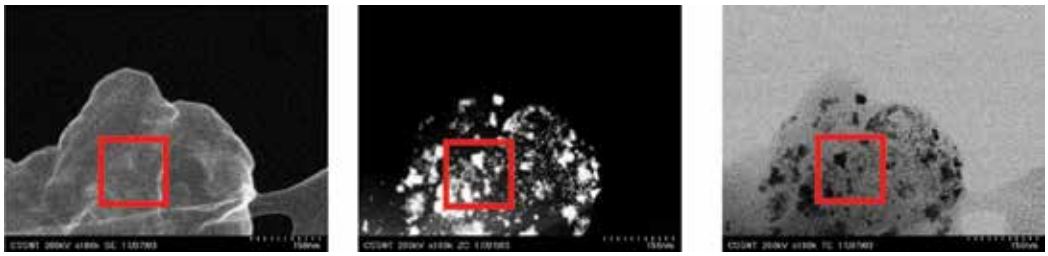

Figure 3. Co-localized SE—secondary electrons (left), ZC—phase contrast (middle) and TE—transmission electrons (right) images of the Pt/rGO_x sample.

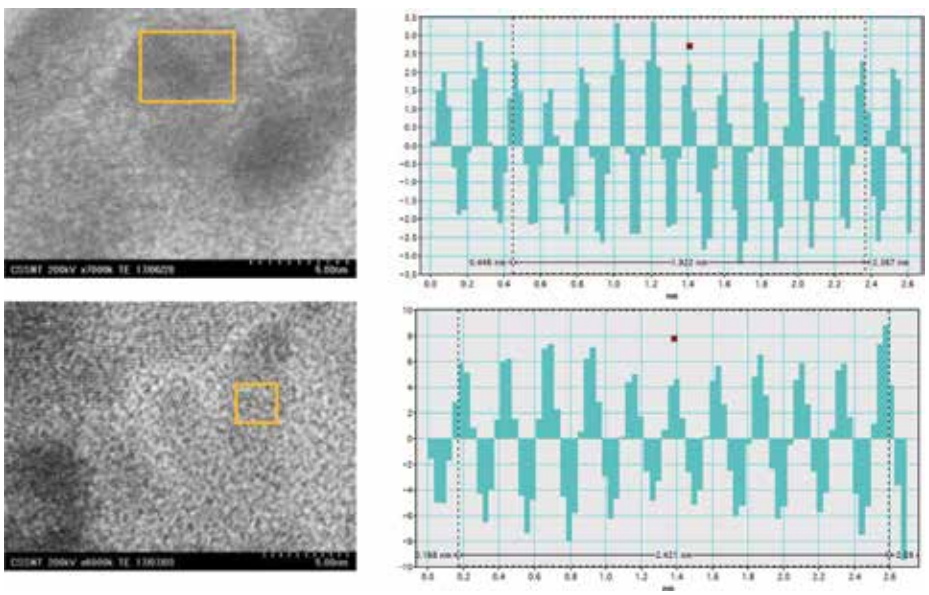

Figure 4. High resolution STEM images of the Pt/rGO_x sample were recorded in the marked area in the co-localized images from above (left). The lattice constant from the area marked in orange was measured and the resulting profiles revealed Pt and graphene specific d-spacings (right).

These obvious characteristic peaks indicate a good crystallinity of the supported Pt/Au nanoparticles in the prepared composites.

The distance between two layers is an important parameter to evaluate the structural information of graphene. Due to the presence of oxygen-containing functional groups attached on both sides of the graphene sheet and the atomic-scale roughness arising from structural defects (sp3 bonding) generated on the originally atomically flat graphene sheet the d-spacing of the GO. The rGO (002) plane was observed at 2θ of about 23° indicating interatomic spacing of about 0.384 nm.

Both metal-dispersed nanoparticles on reduced graphene oxide presented similar XRD peaks corresponding to the face-centered cubic crystalline Pt/Au and no trace of other phases was detected, suggesting that the modification of the drying conditions does not provide a major influence to the crystalline structure.

http://dx.doi.org/10.5772/intechopen.80941

The morphology of reduced graphene oxide doped with gold or platinum samples (Pt/rGO_x and Au/rGO_y) used in this work was examined using scanning transmission electron microscopy technique and the results are shown in **Figure 5**. The images were obtained with different detectors: SE—secondary electrons (left), ZC—phase contrast (middle) and TE—transmission electrons (right) at the same location on the sample. Structural studies were performed on all samples and obtained images were almost similar for each class of materials, namely Pt/rGO_x and Au/rGO_y, respectively.

The (200) plane in Platinum Nanoparticle with face-centered cubic structure was identified with a 1.922 Å d-spacing (ideal 1.962 Å)—up. Single layer graphene flake was identified with a 2.421 Å d-spacing (ideal 2.45 Å)—down.

The (111) plane in Gold Nanoparticle with face-centered cubic structure was identified with a 2.328 Å d-spacing (ideal 2.35 Å)—up. Single layer graphene flake was identified with a 2.461 Å d-spacing (ideal 2.45 Å)—down.

Figures 5 and **6** show the high resolution STEM micrographs, in which the interplanar distances can be clearly seen. The as marked interplanar distances are inserted in profiles from the orange marked areas, corresponding to the (111) and (200) face-centered cubic structure of Pt and Au, respectively, which is in agreement to XRD results.

STEM images showed the Pt and Au nanoparticles supported on the rGO as well-dispersed and well-separated metal nanoparticles, indicating a good spatial distribution of metal nanoparticles on the layered graphene sheets.

The Energy-Dispersive X-ray spectra (EDX) were measured to characterize the elemental heterogeneity of PtNP/rGO_x and AuNP/rGO_y composites. The quantitative analysis was performed at 400x magnification. The EDX spectra for PtNP/rGO_x show signals for carbon, oxygen and platinum with composition presented in **Table 1**. The EDX spectra for AuNP/rGO_y, present signals for carbon, oxygen and gold with composition presented in **Table 2**.

With the desirable structural information presented so far, the materials with higher metal content, were further characterized and tested.

The doping of Pt/Au into graphene oxide is expected to produce some changes in surface area and consequently to the pore size. Thus, due to the porous appearance of the materials confirmed by the performed analysis and taking into account the need for a high surface

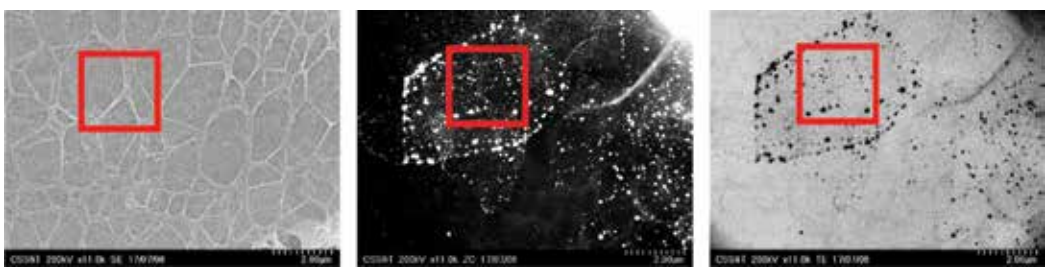

Figure 5. Co-localized SE—secondary electrons (left), ZC—phase contrast (middle) and TE—transmission electrons (right) images of the Au/rGO_y sample.

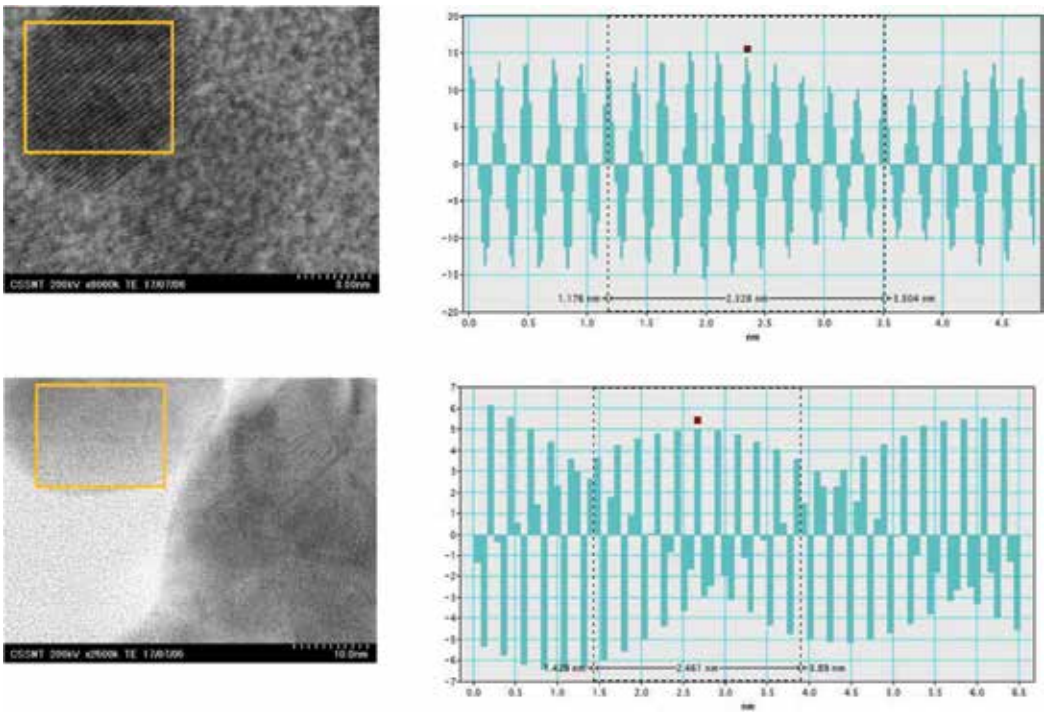

Figure 6. High resolution STEM images of the Au/rGO_y sample were recorded in the marked area in the co-localized images from above (left). The lattice constant from the area marked in orange was measured and the resulting profiles revealed Au and graphene specific d-spacings (right).

Element	PtNP/rGO_1		PtNP/rGO_2	
	Weight %	Atomic %	Weight %	Atomic %
C	58.96	86.01	62.47	85.87
O	10.25	11.22	11.57	11.98
Pt	30.78	2.77	25.96	2.20

Table 1. EDAX quantitative analysis—composition profile for PtNP/rGO_y.

Element	AuNP/rGO_1		AuNP/rGO_2	
	Weight %	Atomic %	Weight %	Atomic %
C	74.91	87.16	72.75	86.46
O	13.79	12.04	14.11	12.59
Au	11.30	0.80	13.14	0.95

Table 2. EDAX quantitative analysis—composition profile for AuNP/rGO_y.

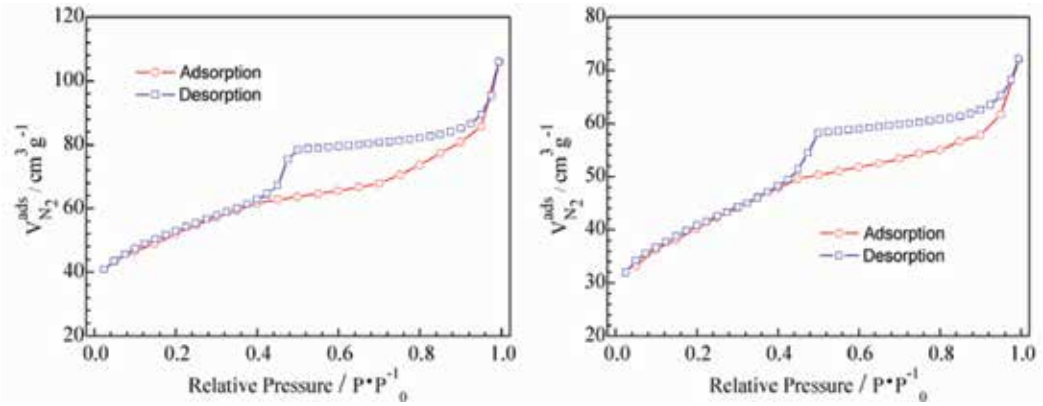

Figure 7. BET isotherms corresponding to Pt/rGO_x and Au/rGO_y.

area to provide an efficient ORR performance, we subsequently analyzed the surface area. The nitrogen adsorption–desorption isotherms were studied using Brunauer–Emmett–Teller (BET) and are provided in **Figure 7**. The hysteresis study also revealed that hysteresis loops showed parallel adsorption and desorption branches, regarded as Type H4 behavior among the IUPAC classification. This observation allows for a better understanding of the porous character of the prepared samples, demonstrating the presence of pores that are open at the end, but unconnected to each other. As shown, the isotherm curves of adsorption/desorption performance of samples were compatible with isotherm Type IV, with an abrupt increase at high relative pressure, with respect to IUPAC classification.

The BET specific surface areas are adequate, namely 158 and 107 $m^2 g^{-1}$ for Pt- and Au-doped graphene oxide with highest metal content. Our measured surface area of the prepared doped graphene samples could be connected with the stacking structure and agglomerated morphology of the reduced graphene sheets and could be attributed to an increasing in the number of closed pores during platinum/gold doping. The estimated radii presented in **Table 3** suggest a hierarchical interconnected porous framework in the prepared doped graphene. Different pore types displayed different roles in the PEMFC electrochemical performance, thus the existence of various porous characteristics ensures sufficient space that enables the access of the reactants to the catalytic sites and could accelerate the kinetic process of ion diffusion.

Based on the structural information presented above, the prepared Pt- and Au-doped graphene oxide was evaluated as ORR cathode under practical FC operation conditions. In comparison to commercial Pt/C, a better cathode performance, including the prepared catalytic

Samples	S_{BET} ($m^2 g^{-1}$)[(a)]	BJH pore volume ($cm^3 g^{-1}$)[(b)]	BJH pore radius (nm)
Pt/rGO	158	0.101	1.857
Au/rGO	107	0.059	1.964

[(a)]BET surface area calculated from the linear part of the BET plot (P/P_0 = 0.1–0.3).

[(b)]BJH pore volume, taken from the volume of N_2 adsorbed at P/P_0 = 0.99, using BJH method.

Table 3. Textural properties of Pt/rGO and Au/rGO.

system based on doped graphene can be easily anticipated, taking into account our recent results [11]. This improvement in performance was explained on the basis of higher electrical conductivity and durability parameters, essential for the PEMFC commercialization.

Electrochemical processes occur at the electrode/solution interface, in contrast to many other chemical measurements that involve bulk solutions. Due to the fact that the reaction is controlled by the electrode potential, electrochemistry is very sensitive and selective for the detection of electroactive species in extremely low limits of detection (nanomolar) and very small sample volumes (μL). The material used defines the performance, hence the continuous interest in developing new generation of electrodes. Carbon materials are widely used in industrial electrochemistry and modified electrodes are still developing with the aim of enhancing both the electrochemical characteristics and performance. There is a large range of carbon based forms available for use as an electrode material, with various allotropic forms exhibiting distinct properties. Among them, graphene materials present an enormous interest for electrochemists owing to their extraordinary physical, chemical and electrical properties. Graphenes are reported as performing electrode constituents for a wide variety of electrochemical applications, including the fabrication of energy storage devices, membrane material, and simultaneous characterization of ascorbic acid, dopamine and uric acid levels [13]. Graphene is the thinnest electrode material, but there are experimental parameters to be overcome: the first problem is the electrical connection of the graphene; the second issue is to avoid the aggregation of graphene sheets to form graphite through strong π–π interactions between the constituting sheets; the last limitation regards the quality of the obtained graphenes by various routes with different electrochemical properties.

The aim of the present research is the fundamental electrochemical characterization of modified graphene-based electrode materials. In electrochemical measurements, supporting electrolytes are widely used. They contain chemical species which are not electroactive in the range of used potentials and have higher conductivity and ionic strength in comparison with electroactive species. Therefore they increase the conductivity of the solution, maintain constant ionic strength and pH, eliminate the transport of electroactive species by ion migration. KCl solutions are widely used as supporting electrolyte, due to relatively high ion conductivity; also potassium ion has a smaller hydration sphere than other alkaline ions We focused our attention on developing novel electrodes using carbon paste as support to investigations of the classical ferri/ferro redox process with attention on the electrochemistry of Pt-doped reduced graphene oxide electrodes. All the modified electrodes were tested for the redox process of 1 mM potassium ferrocyanide(II) using 0.5 M KCl as electrolyte.

$$2\,K_3[Fe(CN)_6] + 2KOH \rightarrow 2\,K_4[Fe(CN)_6] + H_2O + O \quad (1)$$

$$Fe^{3+} + e^- \leftrightarrow Fe^{2+} \quad (2)$$

The electrochemical response of a standard glassy carbon was first tested. **Figure 8** depicts the cyclic voltammetry of the ferri/ferro redox system, scanned from 20 to 120 mV/s in the −0.35 to 0.80 V potential range. The peak-to-peak separation (ΔEp) at 100 mV s^{-1} is 181 mV. Analysis of the peak-to-peak separation as a function of voltage scan rate indicates that the electrochemical process is quasi-reversible within the employed scan rates. Monitoring of the voltammetric

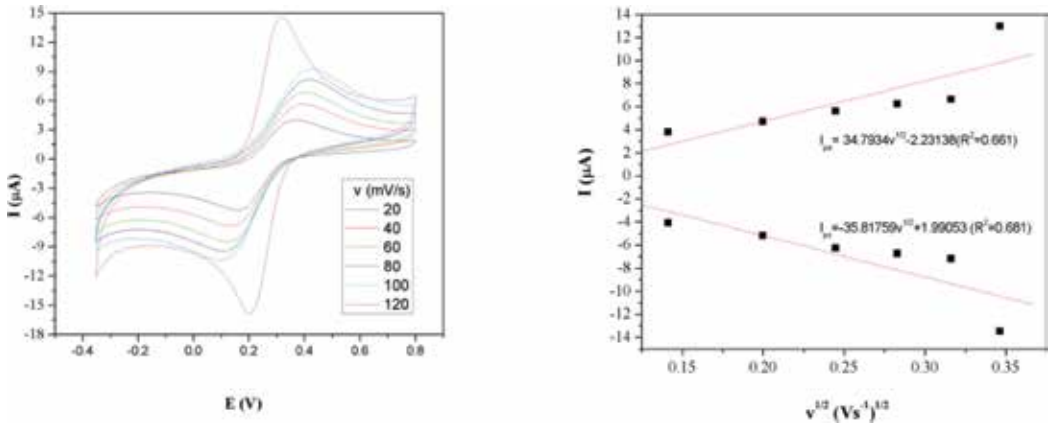

Figure 8. Cyclic voltammograms for 1.0 mM $K_3Fe(CN)_6$ in 0.5 M KCl solution on glassy carbon electrode, v = 20–120 mV s^{-1} (left) and plot of I *vs.* $v^{½}$ (right).

peak height as a function of the square-root of scan rate shows a highly linear response, indicating a diffusion electrochemical process in accordance with reported literature data [14].

The focus herein is to electrochemically characterize reduced GO modified electrodes for efficiency towards ferri/ferro redox probe. For achieving this goal, carbon paste electrodes were prepared by mixing graphite powder with paraffin oil in a ratio of approximately 3:2 (w/w). The two components are hand mixed in a mortar until a consistent wet paste is formed. The obtained paste is placed into a plastic syringe with an inner volume of 1.0 mL. For assuring the electrical contact, a copper wire was inserted into the back of the carbon paste. A control experiment was first performed utilizing a bare carbon paste electrode. The electrochemical characteristic signatures are similar with those of the glassy carbon, the peak-to-peak separations (ΔEp) at 100 mV s^{-1} being 325 mV. This, together with smaller intensity of the peaks indicates that the bare carbon paste electrode is not sensitive to the chosen redox probe. However, the electrochemical process is also diffusion controlled, the voltammetric peak height as a function of the square-root of scan rate also showing a linear response (**Figure 9**).

Next, the modified electrodes were prepared by mixing certain amounts of carbon paste with graphene oxide and then, carbon paste with metal-doped graphene oxide. We have previously observed that modified gold-doped reduced graphene oxide electrodes are sensitive for ferri/ferro redox systems. In all cases, the surface of the electrodes was smoothed by polishing with filter paper. All electrodes were kept in distilled water before and after measurements. The electrochemical measurements were carried out on a potentiostat galvanostat system using one compartment cell of 10 mL containing three electrodes. Each modified carbon paste electrode served as working electrodes. The counter electrode was a large area Pt wire and Ag/AgCl, KCl_{sat} constituted the reference electrode. The experiments were run in the potential range of −0.35 to 0.8 V at various scan rate.

To ensure a better evaluation of the Pt-doped rGO modified electrode, similar experiments with GO-modified electrode were performed. By comparison with the bare carbon paste electrode, the experimental results showed better defined anodic and cathodic peaks related

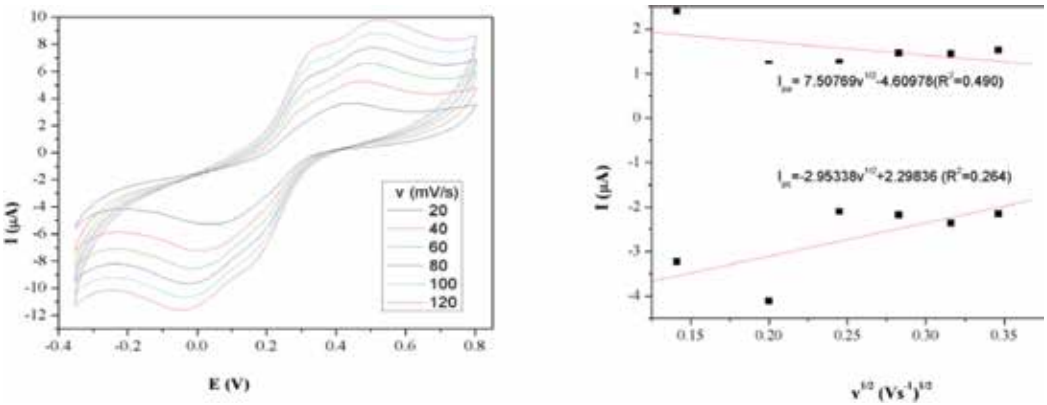

Figure 9. Cyclic voltammograms for 1.0 mM $K_3Fe(CN)_6$ in 0.5 M KCl solution on bare carbon paste electrode, v = 20–120 mV s^{-1} (left) and I *vs.* $v^{½}$ plot (right).

to $Fe(CN)_6^{3-}/Fe(CN)_6^{4-}$ redox couple for slow (20 mV/s) and high scan rates (100 mV/s) (**Figure 10**). The peak separation potential ΔEp was observed as 182 mV, similar with the results observed for the standard glassy carbon electrode. A comparison of cyclic voltammetry measurements is presented in **Figure 11**. In the case of the GO-modified electrode, for both slow and fast sweep rates, both the anodic and the cathodic peaks are sharper and well defined when compared to bare carbon paste electrode. This highlights the positive effect of the graphene oxide on the carbon paste support used for the preparation of the modified electrodes, an improvement of the analytical signal (peak height) being clearly observed.

The voltammetric profile of GO modified electrode was next explored by sweep rate variation from 20, 40, 80 to 120 mV/s. The results show that the anodic peaks increases with increasing the sweep rate and moves to positive potentials. Also, by increasing the sweep rate, the peak shape does not modify, which leads to the conclusion that this modified electrode is sensitive for the electrochemical investigation of the ferri/ferro process. Analysis of the voltammetric peak height as a function of the square-root of the scan rate reveals a highly linear response as observed for the above two investigated electrodes.

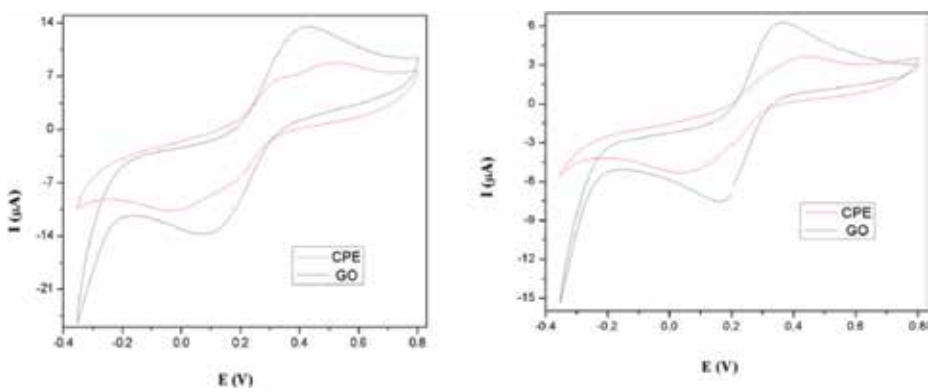

Figure 10. Comparison of the cyclic voltammograms of the modified electrodes according to the legends performed at 20 mV/s (left) and 100 mV/s (right) scan rate.

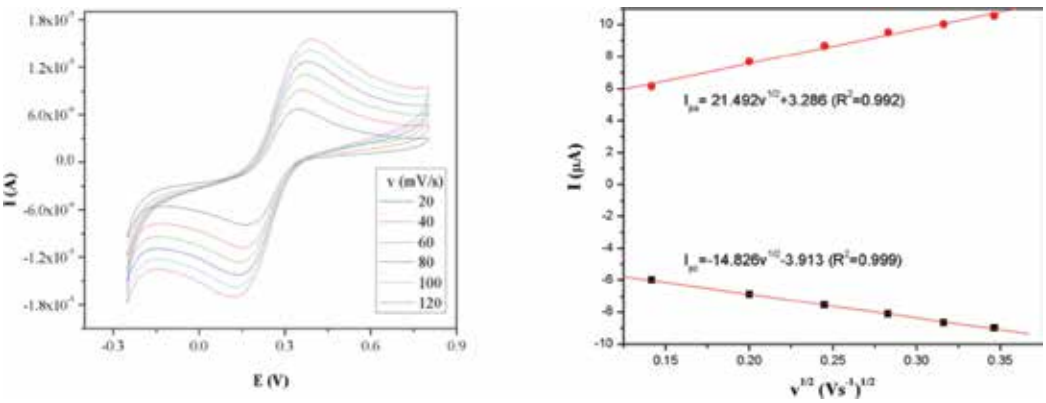

Figure 11. Cyclic voltammograms for 1.0 mM $K_3Fe(CN)_6$ in 0.5 M KCl solution on GO modified electrode, v = 20–120 mV s^{-1} (left) and I *vs*. $v^{½}$ plot (right).

Owing to the superior electrochemical response of the GO-modified electrode, we further explored whether the introduction of metal-doped rGO onto the carbon paste modified electrodes improves the electrochemical response of the studied redox system. Thus, we studied the Pt-doped rGO modified electrode. **Figure 12** shows an overlay of the cyclic voltammograms of Pt/rGO and GO modified electrodes. Analysis of the cyclic voltammograms reveals that the platinum-doped rGO modified electrode exhibits an enhancement of the current response when compared to GO which translates in better electrocatalytic activity for both oxidation and reduction processes, due to the metal presence. A better electrochemical performance than the non-metal modified GO electrode was recorded with a current 3.94 times higher than bare carbon paste electrode (**Table 4**). Both anodic and cathodic peak potentials

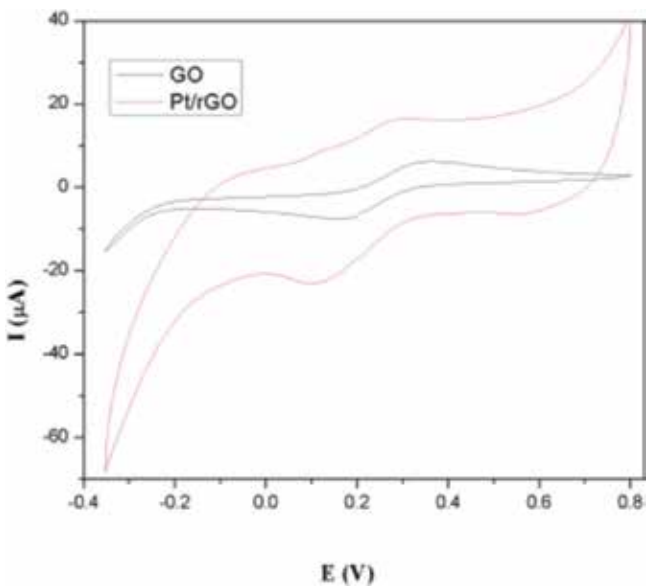

Figure 12. Overlay of the cyclic voltammograms for GO and Pt-doped rGO modified electrodes for the redox process of 1.0 mM $K_3Fe(CN)_6$ in 0.5 M KCl solution (v = 20 mV s^{-1}).

Entry	Electrode type	I_a (A)	I_c (A)	ΔE (mV)	A (cm^2)
1.	CPE	$2.40 \cdot 10^{-6}$	$-3.23 \cdot 10^{-6}$	325	0.0165
2.	GO	$6.14 \cdot 10^{-6}$	$-5.99 \cdot 10^{-6}$	182	0.0309
3.	Au/rGO	$9.45 \cdot 10^{-6}$	$-1.47 \cdot 10^{-5}$	200	0.2020
4.	Pt/rGO	$5.01 \cdot 10^{-6}$	$-8.04 \cdot 10^{-6}$	153	0.0660

Table 4. Electrochemical data from CV measurements at 20 mV/s; I_a and I_c represent the anodic and cathodic peak currents, ΔE is the separation between the peak potentials and A is the area of an electrode, with the corresponding measurements units.

are shifted by approximately −80 mV for Pt/rGO, when compared with the potential of bare carbon paste electrode. An increase in the peak currents and a decrease in the separation between the peak potentials (ΔEp) at 20 mV s^{-1} were observed for all modified electrodes in comparison to the bare CPE (ΔEp = 385 mV), indicating that the electron transfer reaction was kinetically and thermodynamically favored at the graphene oxide modified electrode surface.

By increasing the scan rate, the intensity of the peak increases not only in the anodic direction, but also in the cathodic side. The peaks are not well defined, most likely because of the low concentration of the platinum-doped reduced graphene oxide in the modified electrode. The effect of varying the scan rate results in the slight shifting of the peak potentials to higher values, indicating a quasi-reversible electron transfer. The plot of the peak height *vs.* square-root of the scan rate is illustrated in **Figure 13**, on the right. Both, the anodic and the cathodic peak currents reveal linear response at all scan rates with very good correlation factors above 0.9. These results indicate that the electrochemical process is, as previously observed, controlled by the diffusion of the electroactive species. Modified electrodes containing platinum-doped graphene materials cause an increase of the current, however due to the low concentration, the peaks are not well defined. Reported literature data showed that the electrochemical response of graphene modified electrodes can be improved by increasing the amount of graphene into the electrode [15]. The electrochemical data and areas of the electrodes presented in **Table 4** reveal that the Pt-doped rGO modified electrode has a higher electroactive area than the graphene oxide electrode.

We have shown earlier that Au/rGO modified electrode exhibits an enhancement of the current response when compared to classical glassy carbon, which translates in better electrocatalytic activity for both oxidation and reduction processes. The Au/rGO modified electrode showed a current almost four times higher than bare carbon paste electrode.

A comparison of the cyclic voltammograms of GO, Pt- and Au-doped graphene material electrodes is shown in **Figure 14**. The cyclic voltammetric response of the gold-containing modified electrode shows well defined redox peaks with a peak-to-peak separation, ΔE, of 200 mV. Thus, it was clearly revealed that the insertion of gold onto the modified graphene oxide electrodes gives improved electrochemical response for the ferri/ferro redox signal.

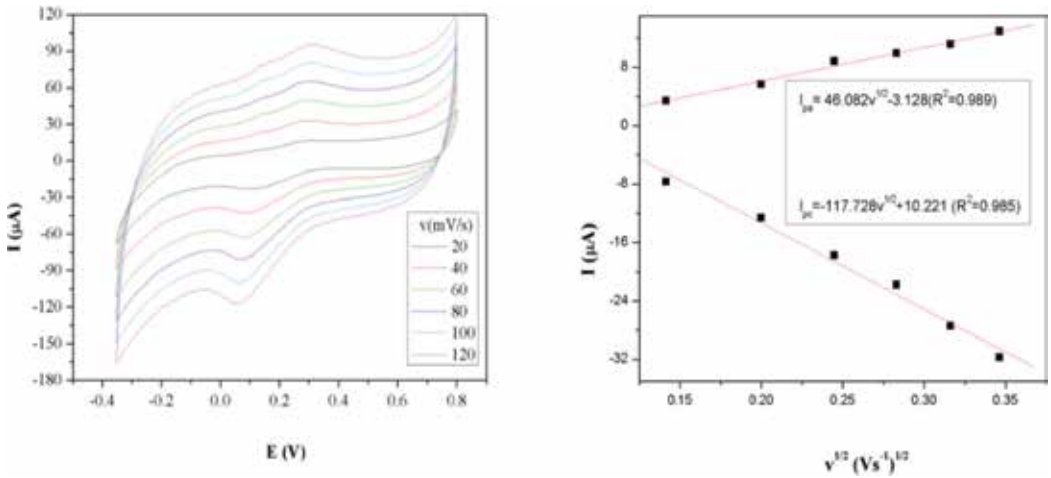

Figure 13. Cyclic voltammograms for 1.0 mM $K_3Fe(CN)_6$ in 0.5 M KCl solution on Pt/rGO modified electrode, v = 20–120 mV s^{-1} (left) and plot of I *vs*. $v^{½}$ (right).

However, the parameter of most significant importance is represented by the position of the voltammetric peak, rather than the magnitude of the wave. In the case of the metal-doped graphene modified electrodes, the larger peak current is likely due to a slightly larger surface area at the electrode (see **Table 4**).

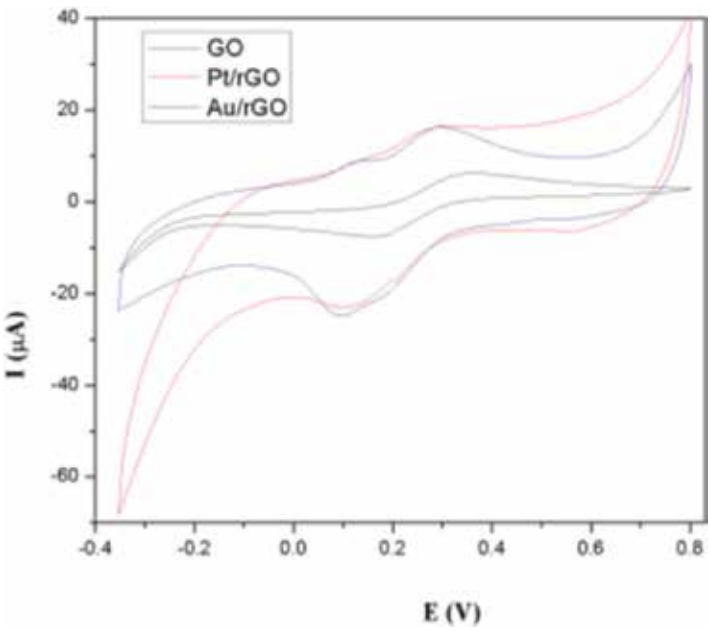

Figure 14. Overlay of the cyclic voltammograms for GO, Pt-doped rGO and Au-doped rGO modified electrodes for the redox process of 1.0 mM $K_3Fe(CN)_6$ in 0.5 M KCl solution (v = 20 mV s^{-1}).

In order to better investigate the electroanalytical outcome of these graphene modified electrodes, we performed differential pulse voltammetry (DPV) measurements. The DPV experiments were meant to support the cyclic voltammetry investigations, as it is clearly known that DPV can assist in resolving the signals due to species with close half-wave potentials, as it measures the difference between two currents, before the end of the pulse and before its application. The strength of this technique is evident when poor electrochemical signals are obtained in cyclic voltammetry, enabling the registration of well-defined signals through the elimination of the non-Faradaic processes. Moreover, DPV provides useful information when the resolving of the voltammetric signals given by two species with close half-wave potentials is needed, producing easily quantifiable peak shaped responses.

Figure 15 compares the differential pulse voltammograms of the graphene modified carbon paste electrodes, as well as the classical glassy carbon electrode. In all cases, sharp and well-resolved peaks are observed. The anodic (right side) and cathodic (left side) peaks are higher for the metal-doped reduced graphene oxide modified electrodes with the highest peak current being observed for the gold doped reduced graphene oxide modified electrode. An important parameter of an electrode material is its electronic properties, namely, the density of electronic states (DOS). The DOS of graphene materials has been reported as being high and it can be increased by varying the amounts of loaded graphene. Gold has a DOS of 0.28 states atom^{-1} eV^{-1} with high conductivity due to high proportion of atomic orbitals. Thus, the Au-doped rGO modified electrodes are highly sensitive for electrochemical investigation of the ferri/ferro redox system.

The active surface areas of the graphene modified electrodes were estimated according to the slope of the I_a *vs.* square root of the scan rates plot for a 1.0 mM $K_3[Fe(CN)_6]$, solution using 0.50 M KCl electrolyte, according to Randles–Sevcik equation [16]:

$$I_a = 2.69 \cdot 10^5 \cdot n^{3/2} \cdot D^{1/2} \cdot A \cdot c \cdot v^{1/2} \quad (3)$$

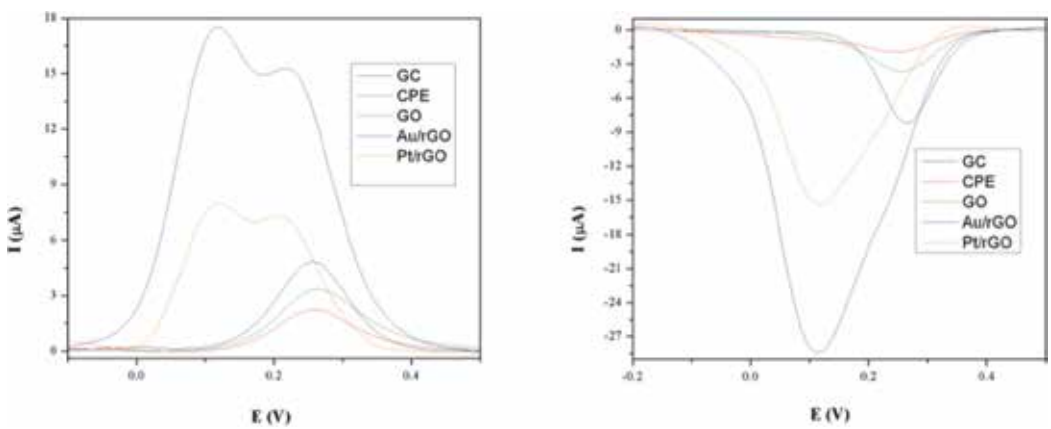

Figure 15. DPV voltammograms for graphene modified electrodes and commercially available glassy carbon electrode (GC): oxidation (left) and reduction (right) with optimized DPV parameters: modulation amplitude of 25 mV and step potential 5 mV.

where I_a refers to the anodic peak current, n to the electron transfer number, A to the surface area of the electrode, D is the diffusion coefficient, c the concentration of $K_3[Fe(CN)_6]$ and ν is the scan rate.

For n = 1 and D = 6.68 × 10^{-6} cm^2 s^{-1} using the slope of the Ip–$\nu^{1/2}$ relation, the microscopic areas were calculated for all the used modified electrodes. The results show that metal-doped graphene oxide materials cause an increase in the active surface of the electrode. The comparison between modified GO electrode and Au-doped rGO reveals a higher active surface of the latter electrode which recommends this material as an electrocatalyst for the ORR reaction in fuel cells. Also, the Pt-doped rGO modified electrode exhibits an electrode active surface two times higher than the graphene oxide modified electrode.

Under PEMFC conditions at cell voltage of around 1.0 V during no-load, the Pt metal dissolution is expected. Moreover, Pt oxides are produced at potentials higher than 0.6 V_{SHE}. In particularly at potentials above 0.95 V_{SHE}, oxygen atoms can replace Pt atoms, thus the potential cycling cause remarkable changes of the catalyst structure. The catalyst exposure to such an accelerated test namely the potential cycling between 0.0–1.2 V_{SHE} lead to a fast catalyst aging, opposed to the constant potential holding test [17]. Thus, the potential cycling could be used as simultaneous CV characterization and degradation testing tool.

For this purpose, the in-situ electrochemical evaluation was performed in a single fuel cell system PEMFC with active area of 25 cm^2 (ElectroChem, USA). A detailed description of the electrodes and membrane electrode assembly fabrication procedure was reported in our previous studies [11–13]. For actual study, the Pt loading was established at 0.2 mg_{Pt} cm^{-2} for anode of all developed fuel cells. The cathode catalyst layer was modified by taking into account three FC configurations, as follows: deposition of commercial Pt/C catalyst Hispec 4000 with 0.4 mg_{Pt} cm^{-2} loading (case 1); commercial Pt/C 0.2 mg_{Pt} cm^{-2} and Pt/rGO with 0.2 mg_{Pt} cm^{-2} loading (case 2); commercial Pt/C 0.2 mg_{Pt} cm^{-2} and Au/rGO with 0.2 mg_{Au} cm^{-2} loading (case 3).The fuel cell test station included specific devices such as configured workstation, fuel cell, DS electronic load, bubble-type humidifiers. The PEMFC was operated at 0.7 V for 1 h for membrane electrode assembly conditioning. After steady state operating conditions were maintained, the cyclic voltammetry measurements were performed in a H_2/N_2 mode cell, from 0.025 to 1.2 V at a scan rate of 0.05 V/s. The flow rates of reactants (50 and 150 mL min^{-1}) gases (H_2 and N_2) were adjusted using flow controllers. The cell temperature and pressure were fixed at 70°C and 1 bar pressure. The developed control system based on NI c-RIO hardware was used to control the PEMFC system.

Carbon corrosion causes the detachment of metal nanoparticles and thus electrical isolation and electrocatalytic inactivity. Taking into account the instabilities due to catalyst support which lead to diminishing of FC performance, we investigated the support aging. **Figures 16–18** present the cyclic voltammograms before and catalyst exposure to 2000 cycles between 0.025 and 1.2 V potential cycling. Our preliminary results indicated that the oxidation and reduction signals approx at 0.025–0.3 V decreased differently after accelerated test, indicating the loss in electrochemical surface area for all cases, more pronounced being recorded for commercial catalyst. In case 1 it is easily to observe the change in hydrogen adsorption/desorption on Pt both for hydrogen oxidation and hydrogen reduction. In case 2 and 3, insignificant changes

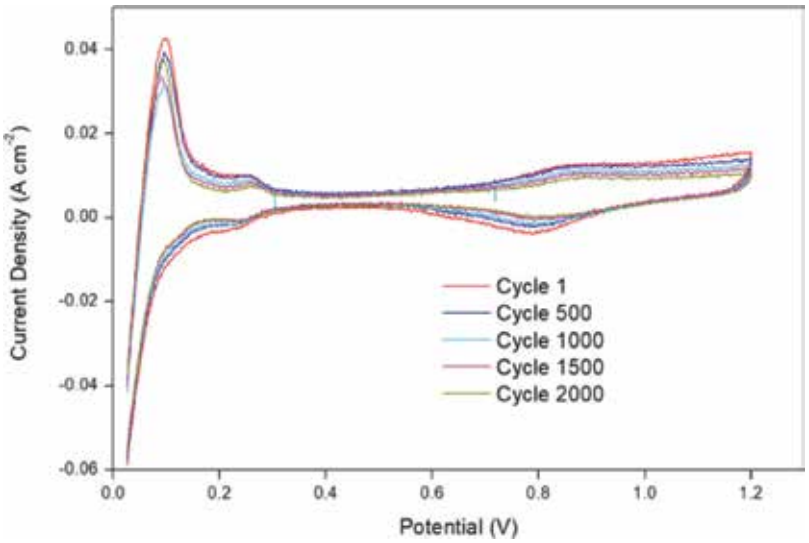

Figure 16. Cyclic voltammetry of commercial Pt/C for 2000 cycles in following operation conditions: temperature 70°C; scan rate 50 mV/s.

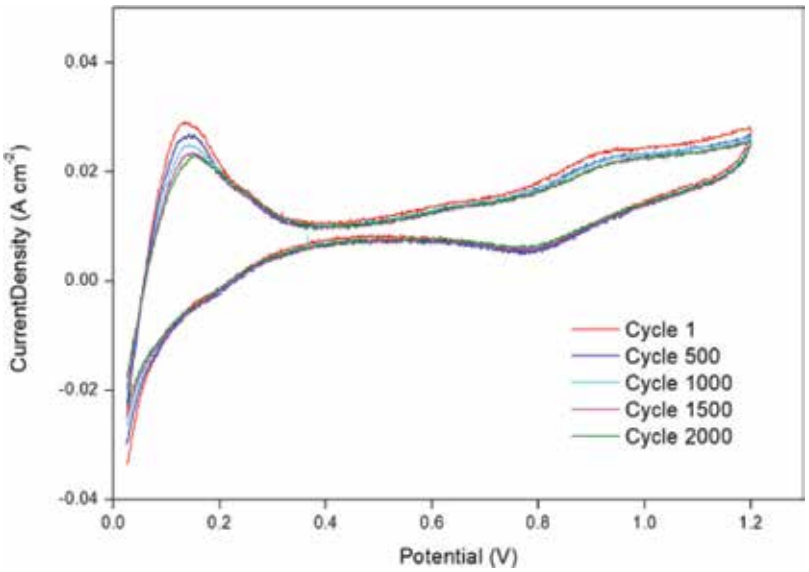

Figure 17. Cyclic voltammetry of Pt/rGO for 2000 cycles in following operation conditions: temperature 70°C; scan rate 50 mV/s.

were observed for reduction signal, which recommend Pt- and Au-doped rGO as potential ORR catalyst for a more comprehensive investigation.

Clearly, there are many types of GO modified electrodes and each is performing for different redox system, but the electrochemistry of graphene materials is far from being fully explored.

http://dx.doi.org/10.5772/intechopen.80941

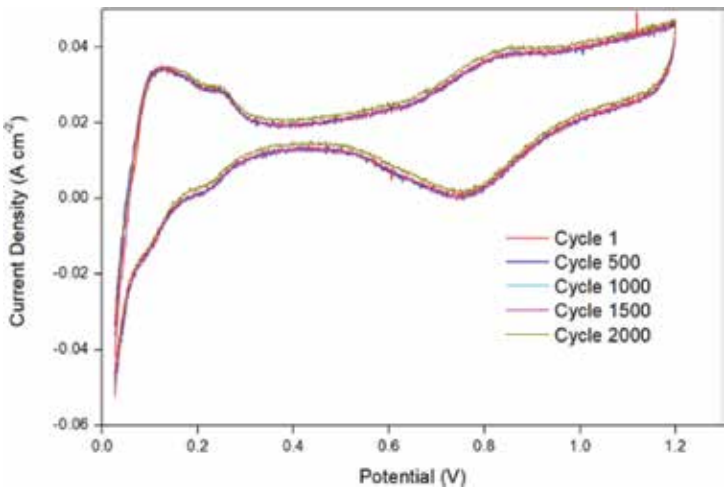

Figure 18. Cyclic voltammetry of Au/rGO for 2000 cycles in following operation conditions: temperature 70°C; scan rate 50 mV/s.

The graphene based material modified electrodes presented herein can significantly contribute to the fundamental understanding of graphene electrochemistry and its application as an electrode material. Future work can be directed to exploring these modified electrodes towards the application of graphene materials in ORR reactions for the development of performing fuel cells.

4. Conclusions

In conclusion, we have successfully synthesized PtNP/rGO and Au NP/rGO nanomaterials. The successful incorporation of Au and Pt nanoparticles into the graphene oxide structure was confirmed. SEM and STEM images show the good spatial distribution of metal nanoparticles onto the layered graphene sheets. Electrocatalytic performance of the prepared materials towards the ORR reaction using cyclic voltammetry and differential pulse voltammetry show that metal-doped graphene oxide materials caused an increase in the active surface of the electrodes. The results obtained by electrochemical characterizations suggest that metal-dispersed nanoparticles on reduced graphene oxide holds a great application potential as a promising electrocatalyst for oxygen reduction reaction due to the advantages of facile preparation and increased catalytic performance. It can be anticipated that the PtNP/rGO and AuNP/rGO composite materials hold great potential for developing novel ORR electrodes for PEM fuel cells. This imparts a high level of confidence that the materials developed as ORR electrocatalysts will be used in our future studies for the fabrication of cathodes for PEM fuel cell, the goal being the improvement of the fuel cell in terms of performance, life time and durability. Therefore, the reason for designed ORR electrocatalyst involves the advantage of improved catalytic activity due to the incorporation of a noble metal (platinum/gold) and ameliorated durability from the 1-dimensional structure.

Acknowledgements

This work is supported by the Ministry of Research and Innovation from Romania by the National Plan of R&D, Project No. PN 18 12 01 02, PN 18 12 01 04 and by Executive Agency for Higher Education, Research, Development and Innovation, under Project M-ERA.net 37/2016. The authors wish to thank Dr. Izabela Jinga from the Centre of Organic Chemistry 'Costin D. Nenitescu' Romanian Academy for her work in the electrochemical experimental study.

Conflict of interest

The authors declare that there is no conflict of interest.

Author details

Adriana Marinoiu[1]*, Mircea Raceanu[1], Elena Carcadea[1], Aida Pantazi[2], Raluca Mesterca[2], Oana Tutunaru[2], Simona Nica[3], Daniela Bala[4], Mihai Varlam[1] and Marius Enachescu[2]

*Address all correspondence to: adriana.marinoiu@icsi.ro

1 RD Institute for Cryogenics and Isotopic Technologies—ICSI, Rm Valcea, Romania

2 Center for Surface Science and Nanotechnology, Politehnica University of Bucharest, Romania

3 Centre of Organic Chemistry 'Costin D. Nenitescu' Romanian Academy, Romania

4 Department of Physical Chemistry, Faculty of Chemistry, University of Bucharest, Romania

References

[1] Gasteiger HA, Marković NM. Just a dream—Or future reality? Science. 2009;**324**(5923): 48-49. DOI: 10.1126/science.1172083

[2] Zhu C, Dong S. Recent progress in graphene-based nanomaterials as advanced electrocatalysts towards oxygen reduction reaction. Nanoscale. 2013;**5**:1753-1767. DOI: 10.1039/C2NR33839D

[3] Lale IS et al. Engineered catalyst layer design with graphene-carbon black hybrid supports for enhanced platinum utilization in PEM fuel cell. International Journal of Hydrogen Energy. 2017;**42**(2):1085-1092. DOI: 10.1016/j.ijhydene.2016.08.210

[4] Shuo D, Anli S, Li T, Wang S. Molecular doping of graphene as metal-free electrocatalyst for oxygen reduction reaction. Chemical Communications. 2014;**50**:10672-10675. DOI: 10.1039/C4CC05055J

[5] Li M, Zhang L, Xu Q, Niu J, Xia Z. N-doped graphene as catalysts for oxygen reduction and oxygen evolution reactions: Theoretical considerations. Journal of Catalysis. 2014;**314**:66-72. DOI: 10.1016/j.jcat.2014.03.011

[6] Agnoli S, Favaro M. Doping graphene with boron: A review of synthesis methods, physicochemical characterization, and emerging applications. Journal of Materials Chemistry A. 2016;**4**:5002-5025. DOI: 10.1039/C5TA10599D

[7] Jiang L, Fan Z. Design of advanced porous graphene materials: From graphene nanomesh to 3D architectures. Nanoscale. 2014;**6**:1922-1945. DOI: 10.1039/C3NR04555B

[8] Yanan T, Zongxian Y, Xianqi D. Trapping of metal atoms in the defects on graphene. The Journal of Chemical Physics. 2011;**135**:224704. DOI: 10.1063/1.3666849

[9] Marinoiu A, Cobzaru C, Carcadea E, Raceanu M, Atkinson I, Varlam M, et al. An experimental approach for finding low cost alternative support material in PEM fuel cells. Revue Roumaine de Chimie. 2016;**61**(4-5):433-440

[10] Marinoiu A, Teodorescu C, Carcadea E, Raceanu M, Varlam M, Cobzaru C, et al. Convenient graphene based materials as potential candidates for low cost fuel cell catalysts. Reaction Kinetics Mechanisms and Catalysis. 2016;**118**:281-296. DOI: 10.1007/s11144-016-1016-7

[11] Marinoiu A, Raceanu M, Carcadea E, Varlam M, Stefanescu I. Doped Graphene as non-metallic catalyst for fuel cells. Materials Science. 2017;**23**:108-113. DOI: 10.5755/j01.ms.23.2.16216

[12] Marinoiu A, Raceanu M, Carcadea E, Varlam M, Balan D, Ion-Ebrasu D, et al. Iodine-doped graphene for enhanced electrocatalytic oxygen reduction reaction in proton exchange membrane fuel cell applications. Journal of Electrochemical Energy Conversion and Storage. 2017;**14**:31001. DOI: 10.1115/1.4036684

[13] Marinoiu A, Raceanu M, Carcadea E, Varlam M, Stefanescu I. Low cost iodine intercalated graphene for fuel cells electrodes. Applied Surface Science. 2017;**424**:93-100. DOI: 10.1016/j.apsusc.2017.01.295

[14] Sun CL, Lee HH, Yang JM, Wu CC. The simultaneous electrochemical detection of ascorbic acid, dopamine, and uric acid using graphene/size-selected Pt nanocomposites. Biosensors & Bioelectronics. 2011;**26**:3450. DOI: 10.1016/j.apsusc.2017.01.295

[15] Lin WJ, Liao CS, Jhang JH, Tsai YC. Graphene modified basal and edge plane pyrolytic graphite electrodes for electrocatalytic oxidation of hydrogen peroxide and β-nicotinamide adenine dinucleotide. Electrochemistry Communications. 2009;**11**:2153

[16] Bard AJ, Faulkner LR. Electrochemical Methods. New York: Wiley; 1980

[17] Dana S, Hulstede J, Wagner P, Kruusenberg I, Tommeveski K, Dyck A, et al. Stability of Pt nanoparticles on alternative carbon supports for oxygen reduction reaction. Journal of the Electrochemical Society. 2017;**164**:995

Section 2

Electrocatalysts for Water Splitting

Chapter 5

Electrocatalytic Properties of Molybdenum and Tungsten Alloys in the Hydrogen Evolution Reaction

Valeriy Kublanovsky and Yuliya Yapontseva

Additional information is available at the end of the chapter

http://dx.doi.org/10.5772/intechopen.79058

Abstract

The search for new electrode materials which are able to intensify the currently used process for the electrolytic production of pure hydrogen is an important scientific and technical problem. Promising materials for making electrodes or for the modification of currently used nickel cathodes are alloys of iron subgroup metals with molybdenum or tungsten, which show a higher catalytic activity in the hydrogen reduction reaction compared with pure nickel or cobalt and have a high corrosion resistance in aggressive media. The present chapter demonstrates that the catalytic, magnetic, and corrosive properties of coatings depend not only on the chemical composition of the alloy but also on its phase composition and morphology so that even coatings having the same chemical composition, but obtained under different conditions, possess different properties. Thus, by changing the electrolyte composition and the electrolysis parameters, one can obtain coatings with optimal set of functional properties and the distribution of metals on the surface which ensure hydrogen spillover and, hence, a high rate of the desired reaction.

Keywords: electrocatalytic activity, hydrogen evolution, electrodeposition, molybdenum, tungsten, spillover, corrosion

1. Introduction

The amount of energy consumed in the world has been steadily increasing in the recent decades, and the nonrenewable fossil energy sources account for over 80% of it [1]. In view of this, the search for efficient, environmentally appropriate methods for the generation of renewable energy is a vital present-day scientific problem [2]. One such promising trends is fuel cells [3, 4], the operation of which is directly bound up with the availability of high-purity hydrogen.

At the present time, the wide use of pure hydrogen is economically inexpedient in comparison, e.g., with the use of natural gas, because of the high cost of its production. The industrial method for hydrogen production by the electrolysis of alkaline aqueous solutions [5] has a number of disadvantages, such as the large expenditure of energy, low efficiency of the process, and the necessity of using noble metals as catalysts. Low carbon steel, which is corrosion-nonresistant in alkaline medium, and nickel also possess a catalytic effect in the hydrogen evolution reaction [6]; nevertheless, the problem of search for electrode materials with lower hydrogen evolution overpotential and high corrosion resistance remains vital. For instance, platinum group catalysts can be replaced by cheaper materials, such as nickel, molybdenum, and iron-chromium and iron-manganese alloys, in electrolysis in ionic liquids [7]. However, if the high cost of ionic liquids themselves is taken into account, there is no considerable reduction in the cost of materials for pure hydrogen production.

1.1. Hydrogen electroreduction mechanism and spillover effect

In the general form, the hydrogen electroreduction process in an alkaline medium is described by the Volmer (1)—Heyrovsky (2)—Tafel (3) mechanism with the following stages:

$$Me + H_2O + e \rightarrow MeH_{ads} + OH^- \quad (1)$$

$$MeH_{ads} + H_2O + e \rightarrow H_2 + Me + OH^- \quad (2)$$

$$2MeH_{ads} \rightarrow H_2 + 2Me \quad (3)$$

The rate of electrocatalytic reaction depends on the energy of adsorbed species, i.e., on the energy of hydrogen atoms. The plot of the exchange current density of hydrogen evolution reaction against hydrogen-metal bond energy passes through a maximum and has a volcano-like shape (**Figure 1**).

At low Me—H bond energy, the process is controlled by the discharge step, reaction (1). At very high Me—H bond energy, the process is controlled by the electrochemical desorption step, reaction (2). On nickel, cobalt, and iron, the rate-determining step changes from reaction (1) to (2) with increasing polarization. Thus, the most important parameter that determines electrocatalytic activity is the energy of bonding of adsorbed species to the catalyst [9]. When catalysts consisting of two metals are used, the formation of several alloy types, such as mechanical mixtures, solid solutions, and intermetallics is possible. From an analysis of the mechanism of electrocatalytic processes, metal-metal bond energy, and the properties of different alloy types, the authors of [9] conclude that the alloys formed by the metals that are on the different branches of the volcano plot and especially the alloys formed by d-metals with unoccupied d-orbitals (of groups IV–VI) and d-metals of group VIII with a large number of filled d-orbitals possess electrocatalytic activity.

It is known from literature that transition-metal alloys, viz. alloys of iron subgroup metals with molybdenum and tungsten, which show electrocatalytic properties with respect to

http://dx.doi.org/10.5772/intechopen.79058

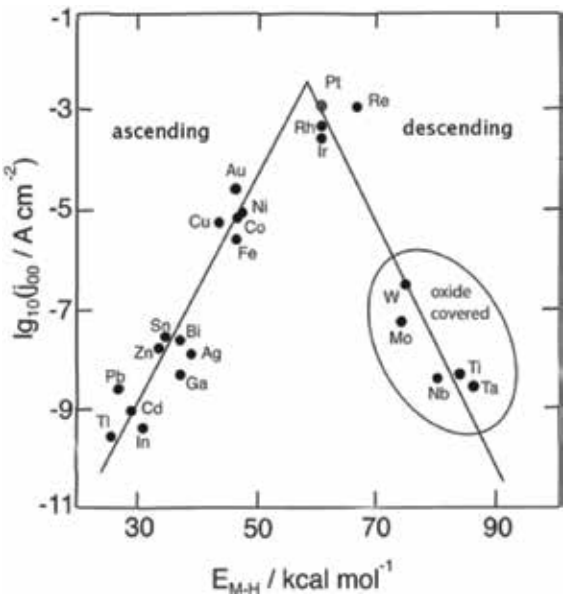

Figure 1. Dependence of the exchange current density of hydrogen evolution reaction in acid solutions against hydrogen-metal bond energy. Reprinted with permission from Ref. [8].

hydrogen reduction reaction both in acidic [10–13] and in alkaline aqueous solutions [14–17], meet these requirements, and that the use of the electrochemical method for the deposition of thin alloy coatings makes it possible to reduce the cost of electrode materials and hence the cost of produced hydrogen.

The synergetic action of alloys in comparison with individual metals is explained by researchers not only by the type of formed alloy and its chemical composition but also by the difference in the mechanism of hydrogen electroreduction on the metals, as well as by the phenomenon of interfacial diffusion of adsorbed hydrogen, hydrogen spillover. The authors of [18] showed the frequent occurrence of this phenomenon in various catalytic processes and catalyst types. Spillover is called the transport of active species, sorbed or formed on one phase, to another phase, which does not sorb and form these species. A study of the synergetic effect of alloys of cobalt and nickel with molybdenum and tungsten with allowance for hydrogen spillover was carried out in [19] for hydrodesulphurization reaction as an example, and it was suggested that different process stages occur on different catalyst phases, between which hydrogen spillover takes place. The spillover phenomenon is of great practical importance, the study of which will help to design new multiphase catalysts, where the catalytic reaction takes place by interfacial diffusion.

As applied to the alloys of molybdenum and tungsten with iron group metals, the spillover phenomenon can account for the synergetic effect of these alloys, in the case of which the discharge step on Mo(W) takes place quickly, and on Co(Ni, Fe), the electrochemical desorption step is fast. Thus, in order that this mechanism may be effected, the active centers of different nature must be at the distance from one another that makes possible the surface diffusion of hydrogen adatoms, and hence the alloy must be a solid solution or an intermetallic.

2. Electrocatalytic properties of nickel alloys

Nickel is the most commonly used cathode material in electrolyzers for hydrogen production [20] due to its catalytic properties, corrosion resistance in alkaline medium, and low cost. A possible way of intensifying the process and improving the required properties is electrode surface modification by molybdenum and tungsten alloys; therefore, many papers are devoted to the study of the electrodeposition and catalytic activity of NiMo and NiW alloys. For instance, the authors of [21] studied the electrodeposition of a NiMo alloy on a copper and a nickel substrate from a citrate electrolyte with pH 9.5 and a concentration ratio of the metals of 1/12. The best catalytic activity was found for a coating containing 41 wt.% molybdenum, and it was shown that the hydrogen evolution overpotential at the obtained alloy is lower compared with pure nickel in the model 1 M NaOH solution. In the study [22], a citrate electrolyte with pH 6.0 was also used, and it was shown that it is possible to deposit an alloy containing 28.5 at.% Mo, which reduces the hydrogen evolution overpotential in 8 M NaOH at 90°C from 122 to 21 $mV \cdot dec^{-1}$ relative to nickel. The authors of [23] found that when a SAS is added to a citrate-ammonia electrolyte for deposition, nanocrystalline coatings having catalytic activity at a molybdenum content of 19.59 at.% can be obtained. Chialvo and co-authors [24] studied the catalytic activity of thermal NiMo alloys as a function of the amount of molybdenum (0–25 at.%) and showed that the higher the Mo content, the lower the hydrogen overpotential. From an analysis of literature data, it can be concluded that there is no unambiguous dependence of electrocatalytic activity on the chemical composition of the coating; for each particular deposition electrolyte, activity is proportional to the molybdenum content, but from the comparison of a large number of papers, it becomes clear that the determining factor is electrolysis conditions, which determine the morphology, the true surface area, the presence of cracks, or an oxide phase on the alloy surface. Therefore, the catalytic properties of electrocatalytic alloys are determined experimentally in each particular case.

On the basis of investigations carried out by the authors of [25], it was concluded that molybdenum-bearing alloys are more active in the hydrogen evolution reaction in alkaline medium than tungsten-bearing alloys. When investigating the properties of Ni-Mo, Ni-W, Co-Mo, and Co-W alloys, it was also found that cobalt alloys show a higher catalytic activity than nickel alloys.

3. Electrocatalytic properties of cobalt alloys

The main characteristics of electrocatalytic activity in HER are reaction exchange current and hydrogen reduction overpotential. Therefore, the main method for studying this process is voltammetry.

3.1. Tungsten alloys

In the study [26], an investigation on the electrocatalytic properties of Co-W alloys electrodeposited from a polyligand citrate-pyrophosphate electrolyte had been carried out. The

http://dx.doi.org/10.5772/intechopen.79058

coatings were deposited in a solution containing 0.1 mol L^{-1} of $CoSO_4$, 0.2 mol L^{-1} of Na_2WO_4, 0.2 mol L^{-1} of Na_3Cit (where Cit—citrate ions), 0.2 mol L^{-1} of $K_4P_2O_7$, 0.5 mol L^{-1} of Na_2SO_4 and in solutions containing SASs: 2 mL L^{-1} of water-soluble resin neonol, whose efficiency was shown when electrodepositing Co-W alloys from a citrate-ammonia electrolyte [27], and 1.5 g L^{-1} and 4.5 g L^{-1} of a nonionic SAS, OP-10 emulsifier. All experiments were performed under forced convection conditions in a current density range of 5.0–30.0 mA cm^{-2} at 50°C and electrolyte pH 8.5.

It can be seen from **Figure 2** that the composition of the coatings deposited from a citrate-pyrophosphate electrolyte is constant regardless of deposition current density and addition of SASs. All coatings containing on an average 22 at.% W, nevertheless, differ in the current efficiency of their deposition and in the morphology of the produced surface. A small increase in current efficiency for alloys is observed in the case of adding a SAS (neonol or OP-10) to the electrolyte. For instance, at 5.0 mA cm^{-2} in the presence of neonol, the current efficiency reaches 68%, and a compact, bright, adherent coating is formed. The addition of OP-10 has a noticeable effect only at a concentration of 4.5 g L^{-1}.

The addition of SASs to the electrolyte and deposition current density affects greatly the quality and morphology (**Figure 3**). For instance, in the electrolyte without additives at a current density of 5.0 mA cm^{-2}, compact bright coatings are deposited. When the current density is increased to 10.0 mA cm^{-2}, the coating becomes more stressed, and microcracks appear, and at 30.0 mA cm^{-2}, the formation of spherulites is observed. The addition of neonol makes it possible to obtain high-quality fine-crystalline deposits in a wider current density range, and the addition OP-10, on the contrary, facilitates the formation of spherulites and favors surface development.

The electrocatalytic properties of CoW coatings in the hydrogen reduction reaction were investigated by stationary voltammetry in 1.0 and 6.0 mol L^{-1} KOH solutions because KOH is used in industrial water electrolysis, and under experimental conditions, i.e., at room temperature, the solution has a maximum electrical conductivity at 28 wt.% KOH.

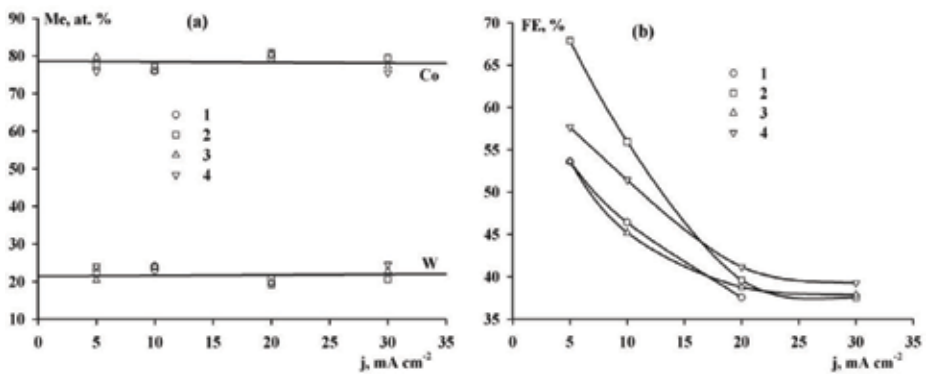

Figure 2. Dependence of the composition (a) and current efficiency (b) of Co-W alloys obtained from electrolyte: 1—without additives; 2—neonol; and 3 and 4—OP-10 (1.5 and 4.5 g L^{-1}) on the deposition current density.

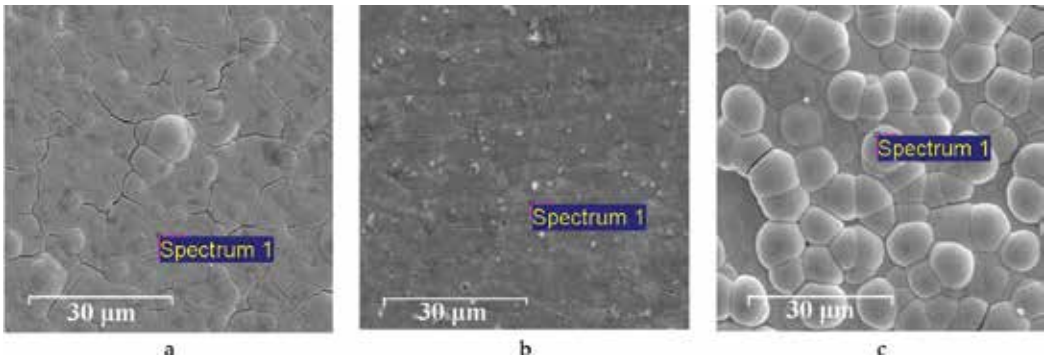

Figure 3. Microphotographs of the surface of alloys obtained from electrolytes (a) without additives and (b) neonol at a current density of 10.0 mA cm^{-2} and (c) OP-10 at 30.0 mA cm^{-2}.

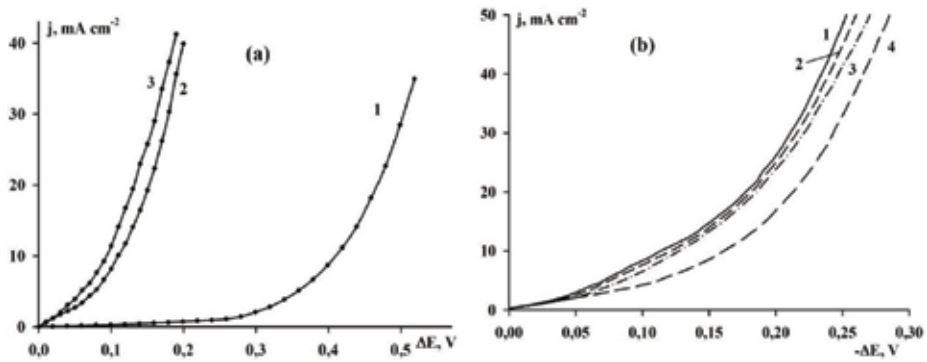

Figure 4. (a) Volt-ampere curves for the electroreduction of hydrogen in a solution of 1.0 mol L^{-1} KOH on cobalt (1) and CoW alloys (2 and 3) electrodeposited from the electrolyte without additives at 10.0 and 20.0 mA cm^{-2}, respectively. (b) Volt-ampere curves for the electroreduction of hydrogen in 6.0 mol L^{-1} KOH solution on CoW alloys, obtained from electrolytes: 1—without additives; 2—neonol; and 3 and 4—OP-10 (1.5 and 4.5 g L^{-1}) at a current density of 10.0 mA cm^{-2}.

Figure 4a shows a considerable decrease in hydrogen overpotential on CoW alloys relative to electrolytic cobalt. For instance, at the current density of 30.0 mA cm^{-2}, the overpotential decreases by 360 mV. As one would expect, a higher electrocatalytic activity is observed for the coating with more developed surface with spherulites morphology.

Figure 4b shows the effect of SASs added to an electrolyte for the deposition of CoW alloys on their electrocatalytic properties in a solution analogous to industrial electrolyte for hydrogen production. It can be seen that in this particular case, the addition of SAS rather has adverse effects, i.e., smoothing the surface during electrodeposition improves the mechanical and corrosive properties of the coating, but reduces its true surface area.

3.2. Molybdenum alloys

In the study [28], cobalt and Co-Mo alloys were deposited from a citrate-pyrophosphate electrolyte, proposed earlier [29], with the different concentration ratio of the metals in the

http://dx.doi.org/10.5772/intechopen.79058

solution: [Co]:[Mo] = 20:1; 10:1: 5:1; 1:1 in a current density range of 10–100 mA cm^{-2} at 50°C. The studies of hydrogen electroreduction on Co-Mo alloys were carried out in solutions with different mineralization and pH, viz. 0.01 mol L^{-1} H_2SO_4; 0.5 mol L^{-1} Na_2SO_4; and 1.0 mol L^{-1} KOH. The voltammetric measurements for the determination of the kinetic parameters of hydrogen reduction were made at 25°C. The current-potential curves were recorded under potentiostatic conditions with a step of 20 mV. Before each experiment, argon was passed through the solution for 30 min.

In order to show clearly the catalytic effect of the alloy in comparison with an individual metal, current-potential curves of hydrogen reduction on pure cobalt deposited from a citrate-pyrophosphate electrolyte at a current density of 30 mA cm^{-2} and a temperature of 50°C have been obtained.

Figure 5 shows current-potential curves of hydrogen electroreduction in an acidic, an alkaline, and a neutral medium on electrolytic cobalt cathodes and cathodes made of Co-Mo alloys electrodeposited at the same current density and temperature.

Because of differences in electroreduction mechanism at different pH values, the lowest hydrogen evolution overpotential on cobalt is observed in an acidic medium and the highest in a neutral medium, as is the case with the dependence obtained for a mercury electrode and described in [30]. In the case of cobalt cathode, the coefficient *b* of the Tafel portion of the polarization curve for the acidic, alkaline, and neutral media was 0.122, 0.142, and 0.125 V, and the exchange current density was 1.93, 4.59×10^{-2} and 6.31×10^{-3} mA cm^{-2}, respectively.

Figure 5 shows a considerable decrease in hydrogen evolution overpotential on the alloy. For instance, at the current density of 10 mA cm^{-2}, the overpotential value in the alkaline medium is lower by over 200 mV.

The plots shown in **Figure 6** have been obtained on alloys electrodeposited at different current densities of 10–100 mA cm^{-2}. The abscissa of the figure gives the ratio of the amounts of the metals in the alloy, and not the exact percentage because of the peculiarities of EDX

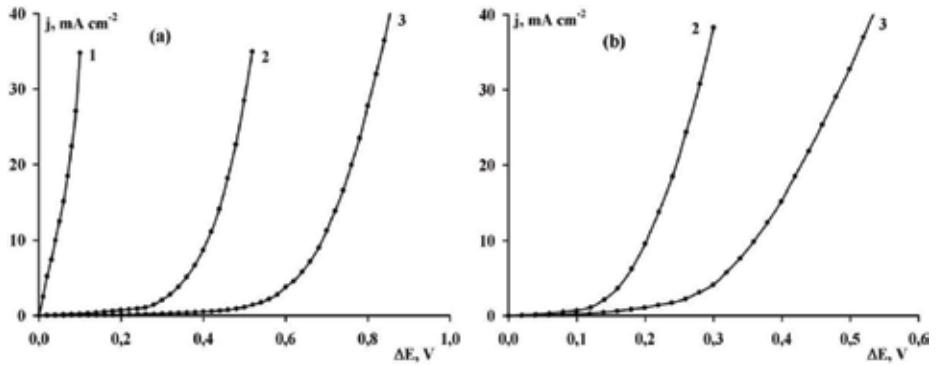

Figure 5. Stationary current-potential curves of the electroreduction of hydrogen evolution on electrolytic cobalt (a) and Co-Mo alloys (b) with the ratio [Mo]/[Mo] + [Co] = 0.33 electrodeposited at the current density 30 mA cm^{-2}, in media with different pH: 1—H_2SO_4, 2—KOH, and 3—Na_2SO_4.

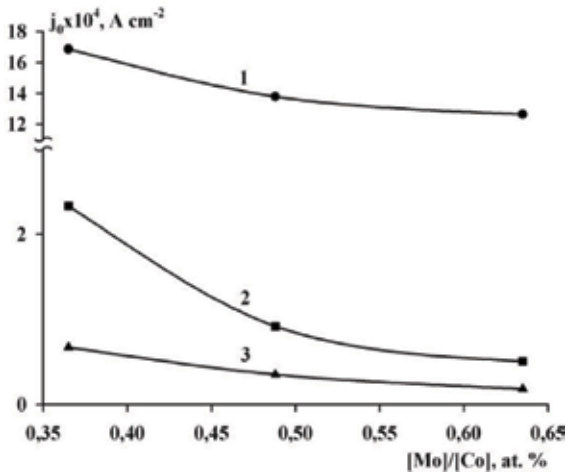

Figure 6. Dependence of the exchange current densities of the hydrogen electroreduction reaction on the ratio of molybdenum to cobalt in alloys electrodeposited at current densities of 10, 30, and 100 mA cm^{-2} from the solution with a [Co]:[Mo] ratio of 1:1 in various media: 1—H_2SO_4, 2—KOH, and 3—Na_2SO_4.

analysis, in which the coating surface layer, on which a large amount of oxygen and carbon are adsorbed. The adsorbed light elements can be removed by polishing the surface or treating it with argon ions. Both in this and in the initial case, the ratio of the metals in the alloy remains constant, as was shown in [17], with a coating depth of up to 100 nm. Thus, the ratio of molybdenum and cobalt in the surface layer, determined by EDX analysis, corresponds to the volumetric chemical composition of the alloy.

In the alloys deposited from an electrolyte with the concentration ratio [Co]:[Mo] = 1:1, the amount of molybdenum decreases and the exchange current density of the hydrogen reduction reaction increases with increasing deposition current density, which can be accounted for in terms of the value which the surface morphology and the true electrode area have, as was shown in [17]. **Figure 7** shows surface micrographs of alloys electrodeposited at two current densities of 10 and 100 mA cm^{-2}. It can be seen that at a low current density, smooth, fine-crystalline, and

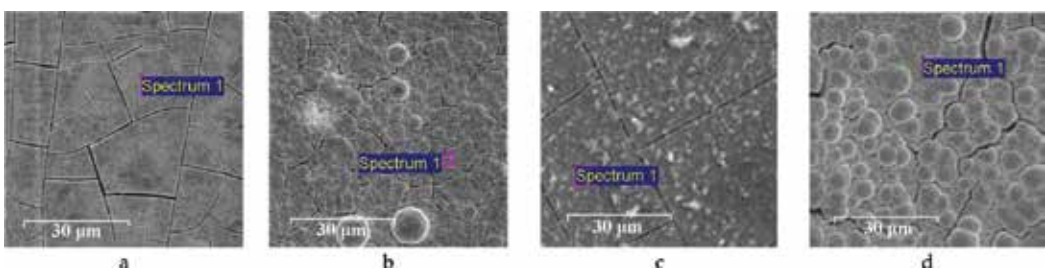

Figure 7. The morphology of Co-Mo alloys precipitated from electrolytes [Co]:[Mo] = 1:1 (a and b) and [Co]:[Mo] = 5:1 (c and d) at current densities of: a and c—10 mA cm^{-2}; b and d—100 mA cm^{-2} and the ratio of metals [Mo]/[Mo] + [Co] equal to 0.39, 0.27, 0.28, and 0.21, respectively.

http://dx.doi.org/10.5772/intechopen.79058

bright coatings are deposited in spite of the presence of microcracks. Increasing the deposition current density to 100 mA cm^{-2} results in the formation of spherulites and considerable surface development. This regularity is observed for all investigated solutions.

The conclusion that the electrocatalytic activity decreases with increasing refractory metal content may contradict papers, published earlier, on the properties of Co-Mo coatings [17, 14]. However, attention should be called on how the coating composition was changed. There are several ways of influencing the chemical composition of alloys, viz. changing the electrolyte composition and pH, temperature, current density, hydrodynamic regime, etc. For instance, in the study [14], a change in alloy composition is achieved by changing both deposition current density and electrolyte composition and in the study [17], by changing pH and, hence, the concentration ratio of different complex species that are able to be discharged to form an alloy. Thus, it is impossible to obtain a rigorous dependence of catalytic activity on the composition of coating deposited under different conditions, because the electrolysis conditions influence not only chemical but also phase composition, which in turn influences the properties of the alloy as a whole.

The effect of change in the composition of the solution for alloy electrodeposition on the electrocatalytic properties is clearly seen in **Figure 8**, which shows current-potential curves of hydrogen electroreduction on cobalt and alloys deposited at a current density of 30 mA cm^{-2} from electrolytes containing different sodium molybdate concentrations. It is seen from the figure that the highest hydrogen evolution overpotential is observed on cobalt deposits and the lowest on the alloy deposited from the electrolyte with [Co]:[Mo] = 10:1. The kinetic parameters of hydrogen electroreduction in an alkaline medium are presented in **Table 1**.

The difference in the value of hydrogen exchange current on alloys with the same chemical composition is seen in **Figure 9**.

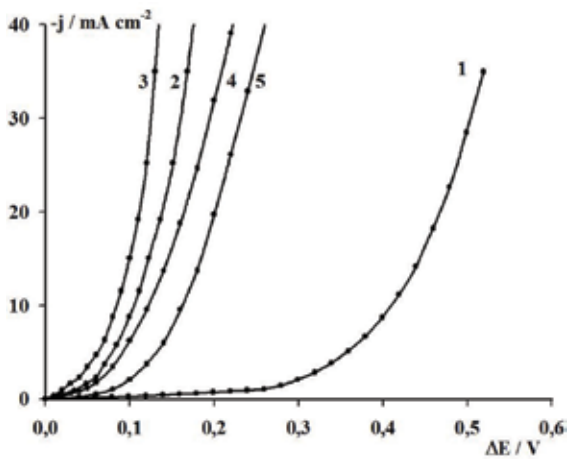

Figure 8. Polarization curves obtained in KOH solution on cobalt (1) and Co-Mo alloys with the ratio of metals [Mo]/[Mo]+[Co] equal to (2)—0.11, (3)—0.19, (4)—0.23, and (5)—0.33, respectively, electrodeposited at 30 mA·cm^{-2} from electrolytes [Co]:[Mo] = 20:1, 10:1, 5:1, 1:1, respectively.

Electrolyte	$j_{dep.}$ (mA cm^{-2})	E_0 (V)	*a*	*b*	j_0 (mA cm^{-2})	[Mo]/([Mo] + [Co])*
Co	30	−0.821	0.190	0.142	4.59×10^{-2}	—
[Co]:[Mo] = 20:1	10	−0.910	0.181	0.134	4.46×10^{-2}	0.22
	30	−0.985	0.038	0.077	3.21×10^{-1}	0.11
[Co]:[Mo] = 10:1	10	−0.940	0.125	0.091	9.23×10^{-2}	0.25
	20	−1.005	0.045	0.058	1.67×10^{-1}	0.23
	30	−1.025	0.025	0.056	3.58×10^{-1}	0.19
[Co]:[Mo] = 5:1	10	−0.920	0.130	0.155	1.25×10^{-1}	0.28
	30	−0.980	0.050	0.062	1.56×10^{-1}	0.23
	100	−1.000	0.035	0.053	2.19×10^{-1}	0.21
[Co]:[Mo] = 1:1	10	−0.900	0.189	0.146	5.08×10^{-2}	0.39
	20	−0.935	0.110	0.089	5.81×10^{-2}	0.37
	30	−0.980	0.083	0.080	9.17×10^{-2}	0.33
	40	−0.965	0.069	0.077	1.27×10^{-1}	0.30
	100	−1.010	0.043	0.068	2.33×10^{-1}	0.27

Here, $j_{dep.}$ is the current density of alloy deposition; E_0 is the stationary potential of the alloy in a KOH solution; *a* and *b* are coefficients in the Tafel equation; and j_0 is hydrogen exchange current density.

*The ratio of the metals was calculated based on their atomic fraction in alloys.

Table 1. Kinetic parameters of hydrogen reduction reaction in a 1 mol L^{-1} KOH.

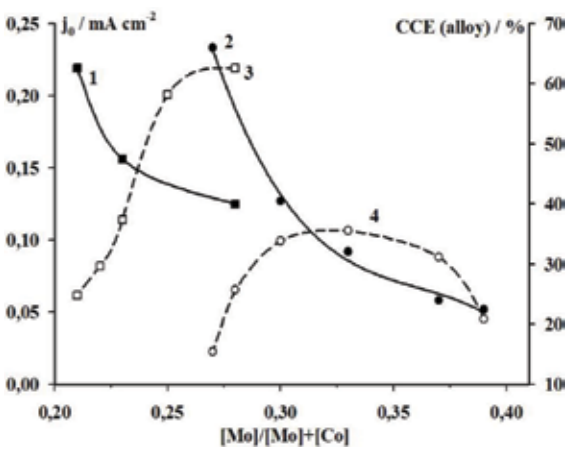

Figure 9. The dependence of the exchange current of the hydrogen reduction in a 1.0 mol L^{-1} KOH solution (1 and 2) and the current efficiency (3 and 4) of the Co-Mo alloys electrodeposited in the electrolytes [Co]:[Mo] = 5:1 and [Co]:[Mo] = 1:1 on the ratio of metals in the alloy.

http://dx.doi.org/10.5772/intechopen.79058

In **Figure 9**, attention should be called on how the current efficiency of the deposition of the alloy and its electrocatalytic activity correlate with each other. In spite of the fact that the current efficiency was measured for a citrate-pyrophosphate electrolyte for deposition, this electrolyte is a weakly alkaline salt solutions, in which the alloys that are formed also exhibit electrocatalytic activity against the parallel cathodes process, with hydrogen electroreduction; therefore, the plots shown in **Figure 9** are of antibate character. Therefore, alloys, electrodeposited at high current densities up to 100 mA cm^{-2} and having the highest catalytic activity (for all deposition electrolytes) are deposited with the lowest current efficiency.

From the obtained data, it can be concluded that in the case of Co-Mo alloys electrodeposited from citrate-pyrophosphate electrolytes, the hydrogen exchange current decreases for each particular electrolyte with increasing amount of molybdenum in the alloy. However, in a series of electrolytes with the different concentration ratio of the discharging metals, the alloys that differ greatly in chemical composition can have the same electrocatalytic activity; this can be seen in **Figure 10**, which shows values of hydrogen exchange currents and stationary potentials for alloys deposited at the same current density, but from different electrolytes.

An extreme form is typical both of the plots of hydrogen exchange current density vs. the ratio of the alloy components and of the stationary potential values of the alloy in the KOH solution.

Thus, the optimal electrolyte for the making of electrocatalytic Co-Mo alloys is the electrolyte with a cobalt and molybdenum concentration ratio of 10:1, which occupies an intermediate position in the series of investigated solutions; so, increasing or decreasing the concentration of sodium molybdate and hence of molybdenum in the alloy results in the deterioration of the catalytic properties of the coating.

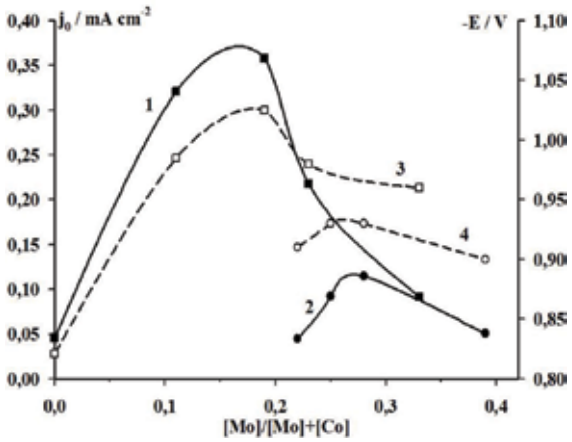

Figure 10. The dependence of the exchange current (1 and 2) and the stationary potential (3 and 4) in the KOH solution on the molybdenum and cobalt ratio in alloys deposited at current densities, mA cm^{-2}. 1: 3—30; and 2: 4—10.

It is known [10] that the electrocatalytic activity of electrode material can be increased by several ways, e.g., by increasing the true working surface area of the catalyst, viz. by making the catalyst not in the form of a continuous film, but in the form of nanofibers [31]. The true surface area must be estimated when fabricating continuous alloy coatings, as this was done in [17]; it should be noted, however, that the factor of surface development is not determining in the ascertainment of the causes of the electrocatalytic activity of the materials under investigation. Another important factor is the nature of the metals comprising the alloy, which was shown in [25], but the physicochemical properties of one metal do not account for the synergetic effect in the use of alloys. The phenomenon that describes most reliably the synergetic action of two or more metals is spillover effect, which was described in [10–12]. Since hydrogen evolution occurs on Co and Mo with different rate-determining steps, as was said above, the occurrence of hydrogen spillover makes it possible to bring about a fact reaction (1) on molybdenum atoms and a rapid electrochemical desorption (2) on cobalt atoms.

Because of this, the synergetic effect of the alloy will manifest itself when the atoms are arranged in an optimal manner to perform sequential reaction steps. This is possible when the alloy is an intermetallic, an amorphous phase, or solid solutions with nanosized crystals.

When we attempted to investigate the coatings obtained by us by X-ray phase analysis, we have not obtained somewhat well-defined peaks of phases, i.e., the coatings were either very fine-crystalline, below the device sensitivity level, or amorphous. However, different properties (e.g., corrosion or magnetic properties) of Co-Mo alloys of the same composition have also been obtained by us earlier. Their phase composition has been studied by us by stripping analysis and shown in [32].

4. Corrosion properties

Some of the main characteristics of modern catalytic materials are not only their activity in the desired reaction but also mechanical strength and corrosion resistance in aggressive media; therefore, the comprehensive investigation of the physicochemical properties of the electrode material is an important scientific and technical problem.

4.1. Tungsten alloys

In the study [26], the corrosion characteristics of electrolytic Co-W alloys deposited from a citrate-pyrophosphate electrolyte in 3.5% NaCl and 6 mol L^{-1} KOH solutions at 25°C have been determined by EIS and stationary voltammetry (**Figure 11**).

The impedance hodographs obtained at a stationary potential in a corrosive medium can be described by a circuit comprising the ohmic resistance of the solution, charge transfer (corrosion) resistance, and a constant phase element. The corrosion parameters calculated in accordance with this equivalent circuit are listed **Table 2**.

The coating deposited at a current density of 5.0 mA cm^{-2} has the highest corrosion stability because in the region of kinetic control of electrochemical reaction, most fine-crystalline

http://dx.doi.org/10.5772/intechopen.79058

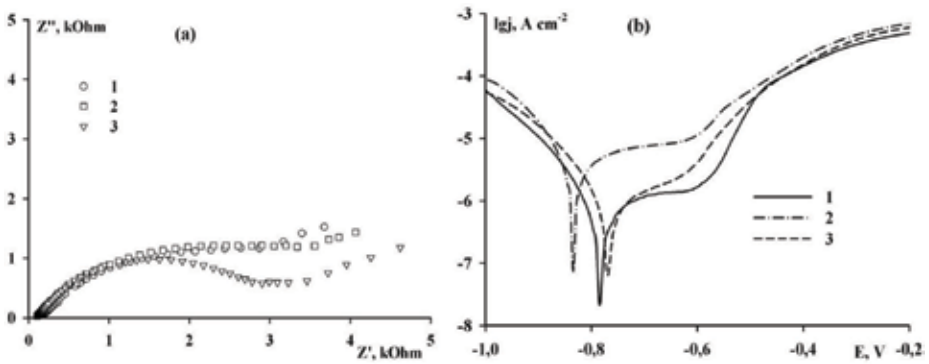

Figure 11. Electrochemical impedance spectra (a) and current-potential curves (b) obtained in the case of corrosion of coatings electrodeposited from a citrate-pyrophosphate electrolyte at the current densities mA cm^{-2}: 1—5.0; 2—10.0; and 3—20.0.

and compact deposits are formed. Since the chemical composition of the coatings deposited from a citrate-pyrophosphate electrolyte is almost constant, the dependence of polarization resistance on deposition current density can be attributed to a difference in surface morphology and the appearance of microcracks on increasing the deposition current. On the whole, the corrosion rate of the obtained alloys is comparable with that in an analogous solution of electrolytic chromium deposited from Cr(III) and Cr(VI) baths in the study [33] (**Figure 12**).

The parameters of the corrosion process, determined by the electrochemical impedance method, have been calculated on the basis of an equivalent circuit comprising the ohmic resistance of the solution, corrosion resistance, a constant phase element, and Warburg impedance (**Table 3**).

The corrosion studies, carried out by us, of CoW alloys in a 6.0 mol L^{-1} KOH solution showed that the corrosion resistance in a concentrated KOH solution (**Figure 12**) is two order of magnitude lower than in a model NaCl solution; nevertheless, the coatings can be considered corrosion proof. It was noted that the coatings obtained for the experiment are of the worst quality in comparison with others, since they are intermediate at the transition from fine crystalline to spherulite deposits. The deposits of these two types are dense and smooth, and only at 10.0 mA cm^{-2}, the largest number of cracks is observed, which accordingly affects the properties of coatings; nevertheless, the coatings have a low corrosion rate and are passivated in alkaline solution.

	j (mA cm^{-2})	W (at.%)	R (kOhm cm^{-2})	R_p (kOhm cm^{-2})	E_{corr} (V)	$J_{corr} \times 10^5$ (A cm^{-2})
1	5.0	23.3	18.0	41.2	−0.782	1.35
2	10.0	24.0	18.8	6.9	−0.834	8.53
3	20.0	20.8	12.8	16.6	−0.786	5.24

Here, j is alloy deposition current density; W is tungsten content, at.%; R is corrosion resistance determined by the impedance method; R_p is corrosion resistance determined by voltammetry; E_{corr} is corrosion potential; and j_{corr} is corrosion current density.

Table 2. Corrosion parameters of alloys in a 3.5% NaCl solution.

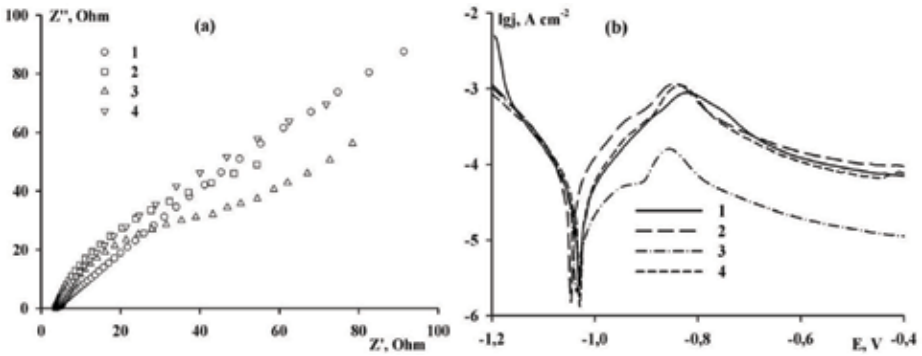

Figure 12. Spectra of electrochemical impedance (a) and current-potential curves (b), obtained in the case of corrosion in a 6.0 mol L^{-1} KOH solution, for coatings electrodeposited at a current density of 10.0 mA cm^{-2} from electrolytes 1—no additives; 2—neonol; 3 and 4—OP-10 (1.5 and 4.5 g L^{-1}).

Electrolyte	W (at.%)	R (kOhm cm^{-2})	R_p (kOhm cm^{-2})	E_{corr} (V)	$J_{corr} \times 10^3$ (A cm^{-2})
1	24.0	0.92	0.58	−1.03	0.84
2	23.7	0.46	0.37	−1.05	0.11
3	24.0	0.34	0.40	−1.04	0.17
4	22.6	0.40	0.48	−1.03	0.12

Table 3. Corrosion parameters of alloys in a 6 mol L^{-1} KOH solution.

4.2. Molybdenum alloys

To determine the corrosion properties of electrolytic Co-Mo alloys in the study [34], the coatings were deposited from a citrate-pyrophosphate electrolyte with different concentration ratios of the metals: [Co]/[Mo] = 1/1 and [Co]/[Mo] = 5/1. The aim of the authors was a large percentage of a component having ferromagnetic properties, i.e., cobalt. To fabricate cobalt-rich alloys, electrolytes with low sodium molybdate content and, hence, with small amount of molybdenum in the coating are used.

As is seen from **Figure 13**, the amount of molybdenum in the alloy electrodeposited from an electrolyte at [Co]/[Mo] = 5/1 decreased relative to the alloy deposited from an electrolyte with [Co]/[Mo] = 1/1; in this case, however, no direct proportionality between the molybdenum content of the alloy and solution is observed. For instance, the concentration ratio of molybdate and cobalt in the electrolyte was 0.2 and changed from 0.4 to 0.27 in the coating. The amount of cobalt in the deposit changes only slightly on increasing the current density, but the percentage of nonmetallic impurities, mainly oxygen, increases, which affect the internal stresses in the deposit. Nevertheless, this change in the concentration ratio of the metals in the solution leads to a great increase in current efficiency for the alloy at low current densities (**Figure 13b**). Thus, it can be stated that in terms of the cobalt content of the alloy, the most optimal conditions for the deposition of magnetic coatings are current densities of 10–50 mA cm^{-2}.

http://dx.doi.org/10.5772/intechopen.79058

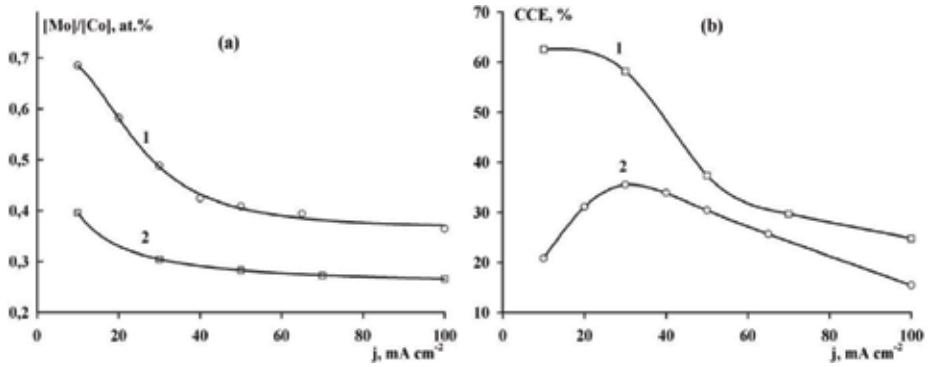

Figure 13. Dependence of the ratio of the metals content (a) and current efficiency (b) for alloys electrodeposited from electrolytes with a concentration ratios [Co]/[Mo] = 1/1 and [Co]/[Mo] = 5/1 on current density.

The corrosion test of the obtained coatings was carried out in a sulfate-chloride solution. The calculation of corrosion resistance from electrochemical impedance data has been performed on the basis of an equivalent circuit comprising the ohmic resistance of the solution, charge transfer resistance, and a constant phase element.

Alloy samples electrodeposited from an electrolyte with [Co]/[Mo] = 5/1 with increasing current density, i.e., with decreasing molybdenum content (**Figure 13**, curve 2), and an alloy electrodeposited from an analogous citrate electrolyte containing no pyrophosphate at 30 mA cm^{-2}, have been investigated. **Figure 14** and **Table 4** show no clear correlation between the molybdenum content of the alloy and corrosion resistance. Besides, the coatings deposited from solutions with the same ratio of the metals in the presence and absence of pyrophosphate are similar in anticorrosion properties despite the difference in their chemical composition.

The anticorrosion resistance of Co-Mo coatings is usually associated with the percentage content of molybdenum in them as a more corrosion-resistant metal, and the magnetic properties

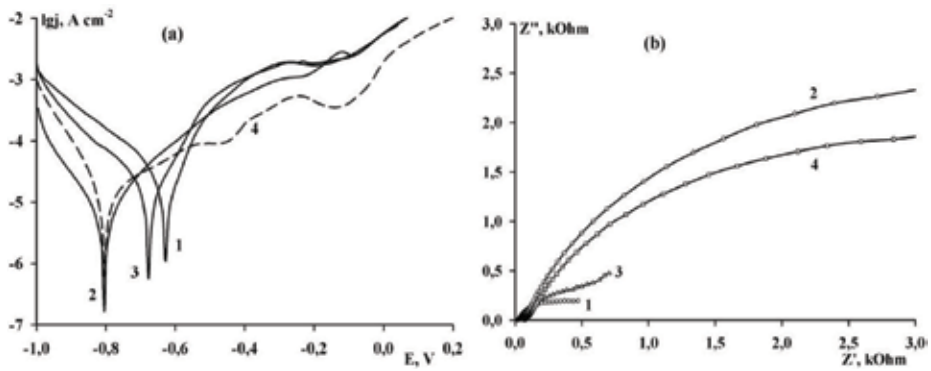

Figure 14. Stationary current-potential curves (a) and electrochemical impedance spectra (b) of the corrosion of alloys deposited from polyligand electrolyte (1–3) and a citrate electrolyte (4) at the deposition current densities, mA cm^{-2}: 1—10; 2 and 4—30; and 3—50.

Electrolyte	j (mA cm^{-2})	Mo (at.%)	R (Ohm)	R_p (Ohm)	E_{corr} (V)	J_{corr} (A cm^{-2})
Citrate-pyrophosphate	10	21.5	5.05×10^2	2.97×10^3	−0.627	3.58×10^{-4}
	30	17.4	5.71×10^3	1.77×10^4	−0.804	829×10^{-6}
	50	16.0	7.02×10^2	3.55×10^2	−0.677	6.40×10^{-4}
Citrate	30	23.9	4.57×10^3	8.06×10^3	−0.804	2.83×10^{-5}

Here, j is deposition current density.

Table 4. Dependence of the corrosion parameters of Co-Mo alloys on alloy composition.

of coatings—with a cobalt content as a metal with ferromagnetic properties. However, the functional properties of coatings can depend not only on the chemical composition of the alloy but also on its phase composition, morphology, thickness, porosity, and other factors.

When studying the corrosion and magnetic properties of Co-Mo coatings [32] deposited from a citrate-pyrophosphate electrolyte, it was found that for the coatings obtained under different electrolysis conditions and having the same chemical composition, the corrosion stability and magnetic parameters are different; it was suggested that the properties of the alloy largely depend on its phase composition.

In the study, the corrosion and magnetic properties of coatings with same Mo content of the alloy (21.2 at.%), deposited from a citrate-pyrophosphate electrolyte under different electrolysis conditions, have been investigated. The corrosion stability of the coatings was studied in a solution containing 7 g L^{-1} Na_2SO_4 and 7 g L^{-1} NaCl at pH 6.0 and 24 ± 1°C (**Table 5**). The magnetic properties (**Table 6**) of the obtained deposits were determined by means of a vibrating sample magnetometer in fields of up to 20 kOe at room temperature (**Table 5**).

The magnetic characteristics of such Alloys are also given. Their calculated values are listed in **Table 6**. The main criteria for evaluating the properties of soft-magnetic materials are low coercive force, low remanent magnetization and high saturation magnetization, as well as the ability to reach saturation magnetization in low intensity fields. It is evident from **Table 6** that the largest saturation magnetization values—927 Gs were obtained at a magnetic field intensity of 3 kOe for the alloys deposited from an electrolyte with a ratio of 5:1. For the coatings deposited from an electrolyte with a ratio of 1:1, no saturation magnetization is observed even at 20 kOe; the maximum value obtained under experimental conditions for alloys deposited at 25° and 50°C was 113 and 290 Gs, respectively. Thus, it can be concluded that the alloy deposited from an electrolyte with the concentration ratio of the metals [Co]/[Mo] = 5/1. We assumed that such a difference in functional properties for the coatings having the same chemical composition may be due to a difference in their phase composition.

Deposition electrolyte	j (mA cm^{-2})	t (°C)	R_p (Ohm)	E_{corr} (V)	J_{corr} (A cm^{-2})
[Co]/[Mo] = 1/1	30	25	2.71×10^3	−0.804	8.44×10^{-5}
[Co]/[Mo] = 1/1	40	50	9.82×10^2	−0.808	2.54×10^{-4}
[Co]/[Mo] = 5/1	10	50	2.97×10^3	−0.627	3.58×10^{-4}

Table 5. Corrosion properties of alloys having the same chemical composition (21.2 at.% Mo).

Deposition electrolyte	j (mA cm^{-2})	t (°C)	H (Oe)	M_R (Gs)	M_S (Gs)
[Co]/[Mo] = 1/1	30	25	155	5.0	113
[Co]/[Mo] = 1/1	40	50	117	20.0	290
[Co]/[Mo] = 5/1	10	50	102	252	927

Here, H is coercive force, M_R is remanent magnetization, and M_S is saturation magnetization.

Table 6. Magnetic properties of alloys having the same chemical composition (21.2 at.% Mo).

To study the phase composition, the electrochemical method of linear stripping voltammetric analysis (LSVA) was used [35]. An advantage of this method, besides simplicity, is the possibility to follow the dissolution dynamics of the alloy. Before the stripping analysis, a 0.5 μM thick layer of Co or Co-Mo alloys were deposited onto the working electrode from a citrate-pyrophosphate electrolyte with the concentration ratios of the metals [Co]/[Mo] = 1/1 and [Co]/[Mo] = 5/1 at a current density of 10–100 mA cm^{-2} and a temperature of 25 and 50°C.

The electrolyte for the anodic dissolution of the obtained alloy deposits must meet the following requirements: it must have a high electrical conductivity, be nonaggressive toward the coating, and not cause spontaneous chemical dissolution. In this electrolyte, an electrochemical side reaction paralleling the anodic dissolution of the deposit under investigation must be ruled out. The use of various acids as working solutions was considered inexpedient since the electrochemical process in such electrolytes is paralleled by the chemical dissolution of the coating under analysis. Alkaline solutions are unsuitable for use as working electrolytes because of passivation processes on the surface of samples under investigation. The optimal solution for the anodic dissolution of coatings under investigation is NaCl solution, which makes it possible to obtain on the current-potential curves clear peaks corresponding to the dissolution potentials of the various phases of the alloy. The stripping analysis of coatings was performed in a 0.5 M NaCl solution at 25°C on a rotating disk electrode at a rotational speed of 774 rpm.

Figure 15 shows a current-potential curve of the dissolution of freshly deposited cobalt (curve 1) in a 0.5 M NaCl solution. The observed dissolution peaks are traditionally attributed to the complex phase structure of metals and alloys, but their number depends on the electrolyte in which dissolution is performed [35]. The plot of cobalt dissolution current vs. potential exhibits three peaks, which we further use in order to distinguish the peaks of dissolution of the alloy from the peaks of cobalt dissolution. The figure shows plots except the oxygen and chlorine evolution curve. It can be seen that in the case of dissolution of alloys, the magnitude of the peaks and their number are different. For instance, for the alloys deposited from an electrolyte with the same concentration ratio of the metals, the magnitude of peak 1 is the same, but besides it, only one large peak is observed for the alloy obtained at 50°C and 40 mA cm^{-2}, whereas two peaks are observed for the alloy obtained at 25°C and 30 mA cm^{-2}. However, for the alloy deposited from an electrolyte with lower molybdate content, the magnitude of peak 1 is much larger than for other alloys. Based on the potentials of the peaks, the known cathodic quantity of electricity, the phase diagram of the double layer, and stoichiometry, it can be suggested that peaks 1 and 3 relate to cobalt dissolution and peak 2 to the dissolution of a solid solution of the chemical compound CoMo in cobalt.

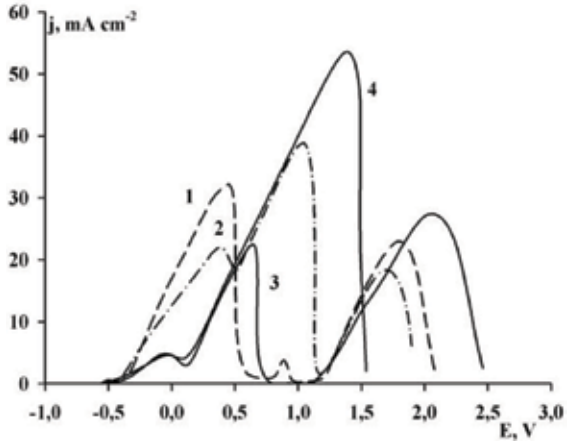

Figure 15. Anodic dissolution curves for pure cobalt (curve 1) and Co-Mo alloys (21.1 at.% Mo) deposited under the following conditions: 2—Co:Mo = 5:1, 50°C, 10 mA cm^{-2}; 3—Co:Mo = 1:1, 25°C, 30 mA cm^{-2}; 4—Co:Mo = 1:1, 50°C, 40 mA cm^{-2}.

Thus, the alloy deposited from an electrolyte containing a small amount of molybdate contains a larger amount of cobalt bound into neither a chemical compound nor a solid solution; this can explain the 200 mV shift of the corrosion potential of this alloy to positive values, i.e., cobalt is a more electropositive metal than molybdenum, as well as the improvement of the magnetic properties of the alloy. The increase in peak 2 indicates an increase in the percentage of the molybdenum-rich phase, which results in the improvement of the corrosion properties of alloys.

Stripping analysis of alloys deposited from an electrolyte with [Co]/[Mo]=1/1 at different current densities is shown in **Figure 16**. It is seen from the figure that for the coatings obtained at lower deposition current densities 10–20 mA cm^{-2}, three dissolution peaks are observed. For the alloys deposited at 30 and 40 mA cm^{-2}, only two dissolution peaks are observed. The magnitude of peak 1 remains unchanged, and it can be assumed to correspond to the amount of cobalt that is directly on the electrode surface, i.e., dissolution of the less corrosion-resistant component than the alloy takes place, and since the electrode geometry does not change, the quantity of electricity for dissolution remains constant too. In the remaining alloy phase at different current densities, different redistribution of cobalt between the solid solution and the free α-phase takes place.

To study the alloy formation process, anodic polarization curves have been obtained for Co-Mo alloys deposited from an electrolyte with [Co]/[Mo] = 1/1 under the conditions corresponding to the maximum current efficiency: a current density of 30 mA cm^{-2} and at temperature of 50°C [36]. The coatings were deposited during 30, 60, 120, and 210 s (**Figure 17**). All current-potential curves of the dissolution of Co-Mo alloys exhibit two peaks. As one would expect, the quantity of electricity for the dissolution of the solid solution increases linearly with deposition time. We failed, however, to determine the order of deposition of the components; using this method, it is impossible to either confirm or refute the hypothesis that cobalt deposits first, which catalyzes later the reduction of molybdenum. Under our experimental conditions, an alloy phase which grows uniformly with increasing deposition time is present in the alloy even within a deposition time of 30 s.

http://dx.doi.org/10.5772/intechopen.79058

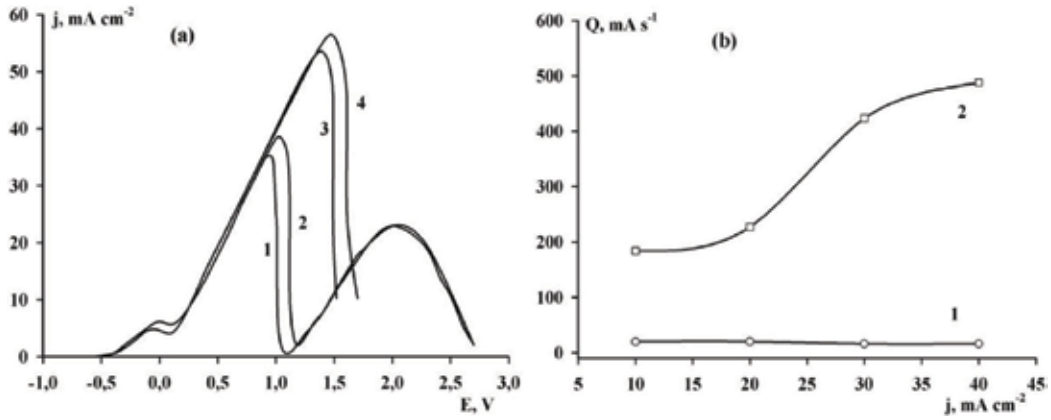

Figure 16. (a) Anodic current-potential curves of the dissolution of Co-Mo alloys deposited from an electrolyte at [Co]/[Mo] = 1/1 at 50°C at different current densities, mA cm^{-2}: 1—10, 2—20, 3—30, 4—40 and (b) The magnitude of anodic dissolution peaks.

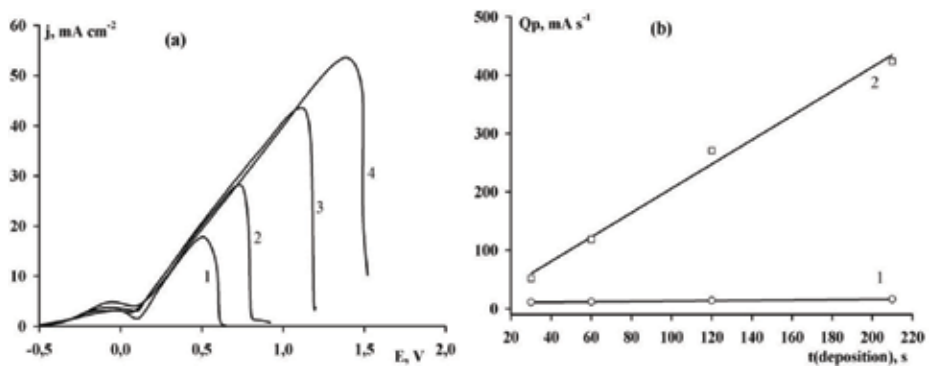

Figure 17. (a) Anodic current-potential curves of the dissolution of Co-Mo alloys deposited from an electrolyte with [Co]/[Mo]=1/1 at 30 mA·cm^{-2} and 50°C at different deposition time, s: 1—30, 2—60, 3—120, 4—210. (b) The magnitude of the anodic dissolution peaks: 1—the first peak, and 2—the second peak.

5. Conclusions

Electrolytic alloys of molybdenum and tungsten with iron subgroup metals possess catalytic properties in the hydrogen evolution reaction and can be used as a coating which improves the properties of exiting nickel cathodes.

For each particular electrolyte and particular deposition conditions, the activity of the alloy and its corrosion stability increase with the amount of molybdenum, but the comparison of data obtained by different authors does not give a clear correlation.

The properties of alloys depend not only on their chemical composition but also on their phase composition. The alloy containing the same amount of molybdenum, but fabricated under different conditions, has different corrosion and magnetic properties.

The amorphous and nanocrystalline structure of electrolytic alloys makes hydrogen spillover possible, which greatly accelerates the hydrogen reduction process in alkaline electrolytes.

Electrolytic coatings of refractory metals alloys have a wide range of physicochemical properties. Controlling the electrolysis modes allows precipitating and accurately controlling the chemical and phase composition of the coatings, and hence producing corrosion-resistant materials for soft magnetic materials, electrocatalysts, and wear-resistant coatings.

Author details

Valeriy Kublanovsky* and Yuliya Yapontseva

*Address all correspondence to: kublanovsky@ionc.kar.net

V. I. Vernadskii Institute of General and Inorganic Chemistry of the Ukrainian NAS, Kyiv, Ukraine

References

[1] Moriarty P, Honnery D. Hydrogen's role in an uncertain energy future. International Journal of Hydrogen Energy. 2009;**34**:31-39. DOI: 10.1016/j.ijhydene.2008.10.060

[2] Marbán G, Valdés-Solís T. Towards the hydrogen economy. International Journal of Hydrogen Energy. 2007;**32**:1625-1637. DOI: 10.1016/j.ijhydene.2006.12.017

[3] Jacobson MZ, Colella WG, Golden DM. Cleaning the air and improving health with hydrogen fuel-cell vehicles. Science. 2005;**308**:1901-1905. DOI: 10.1126/science.1109157

[4] Brumfiel G. Hydrogen cars fuel debate on basic research. Nature. 2003;**422**:104. DOI: 10.1038/422104a

[5] Ulleberg O. Modeling of advanced alkaline electrolyzers: A system simulation approach. International Journal of Hydrogen Energy. 2003;**28**:21-33. DOI: 10.1016/S0360-3199(02)00033-2

[6] Divisek J, Schmitz H, Steffen B. Electrocatalyst materials for hydrogen evolution. Electrochimica Acta. 1994;**39**:1723-1731. DOI: 10.1016/0013-4686(94)85157-3

[7] Loget G, Padilha JC, Martini EA, de Souza MO, de Souza RF. Efficiency and stability of transition metal electrocatalysts for the hydrogen evolution reaction using ionic liquids as electrolytes. International Journal of Hydrogen Energy. 2009;**34**:84-90. DOI: 10.1016/j.ijhydene.2008.10.032

[8] Quaino P, Juarez F, Santos E, Schmickler W. Volcano plots in hydrogen electrocatalysis—Uses and abuses. Beilstein Journal of Nanotechnology. 2014;**5**:846-854. DOI: 10.3762/bjnano.5.96

[9] Korovin N. On the connection between the electrocatalytic activity of metals in the hydrogen evolution reaction with their properties. Elektrokhimiya. 1991;**27**(12):1629-1633

[10] Navarro-Flores E, Chong Z, Omanovic S. Characterization of Ni, NiMo, NiW and NiFe electroactive coatings as electrocatalysts for hydrogen evolution in an acidic medium. Journal of Molecular Catalysis A: Chemical. 2005;**226**:179-197. DOI: 10.1016/j.molcata.2004.10.029

[11] Highfield JG, Claude E, Oguro K. Electrocatalytic synergism in Ni/Mo cathodes for hydrogen evolution in acid medium: A new model. Electrochimica Acta. 1999;**44**:2805-2814. DOI: 10.1016/S0013-4686(98)00403-4

[12] Martinez S, Metikoš-Huković M, Valek L. Electrocatalytic properties of electrodeposited Ni–15Mo cathodes for the HER in acid solutions: Synergistic electronic effect. Journal of Molecular Catalysis A: Chemical. 2006;**245**:114-121. DOI: 10.1016/j.molcata.2005.09.040

[13] Ved M, Sakhnenko N, Bairachnaya T, Tkachenko N. Structure and properties of electrolytic cobalt-tungsten alloy coatings. Functional Materials. 2008;**15**:613-617

[14] Subramania A, Sathiya Priya AR, Muralidharan VS. Electrocatalytic cobalt–molybdenum alloy deposits. International Journal of Hydrogen Energy. 2007;**32**:2843-2847. DOI: 10.1016/j.ijhydene.2006.12.027

[15] Arul Raj I. On the catalytic activity of Ni-Mo-Fe composite surface coatings for the hydrogen cathodes in the industrial electrochemical production of hydrogen. Applied Surface Science. 1992;**59**:245-252. DOI: 10.1016/0169-4332(92)90124-G

[16] Krstajic NV, Jovic VD, Gajic-Krstajic L, Jovic BM, Antozzi AL, Martelli GN. Electrodeposition of Ni–Mo alloy coatings and their characterization as cathodes for hydrogen evolution in sodium hydroxide solution. International Journal of Hydrogen Energy. 2008;**33**:3676-3687. DOI: 10.1016/j.ijhydene.2008.04.039

[17] Kuznetsov VV, Kalinkina AA, Pshenichkina TV, Balabaev VV. Electrocatalytic properties of cobalt-molybdenum alloy deposits in the hydrogen evolution reaction. Russian Journal of Electrochemistry. 2008;**44**:1350-1358. DOI: 10.1134/S1023193508120070

[18] Rosanov VV, Krylov OV. Spillover of hydrogen in heterogeneous catalysis. Uspekhi Khimii. 1997;**66**(2):117-130

[19] Delmon B. A new hypothesis explaining synergy between two phases in heterogeneous catalysis the case of hydrodesulfurization catalysts. Bulletin des Societes Chimiques Belges. 1979;**88**:979-987

[20] Santos Diogo MF, Sequeira César AC, Figueiredo José L. Hydrogen production by alkaline water electrolysis. Quimica Nova. 2013;**36**(8):1176-1193. DOI: 10.1590/S0100-40422013000800017

[21] Manazoglu M, Hapcı G, Orhan G. Effect of electrolysis parameters of Ni–Mo alloy on the electrocatalytic activity for hydrogen evaluation and their stability in alkali medium. Journal of Applied Electrochemistry. 2016;**46**:191-204. DOI: 10.1007/s10800-015-0908-y

[22] Mech K, Zabinski P, Mucha M, Kowalik R. Electrodeposition of catalytically active Ni-Mo alloys. Archives of Metallurgy and Materials. 2013;**58**(1):227-229. DOI: 10.2478/v10172-012-0178-1

[23] Chao X, Zhou J-b, Zeng M, Xin-ling F, Liu X-j, Li J-m. Electrodeposition mechanism and characterization of Ni-Mo alloy and its electrocatalytic performance for hydrogen evolution. International Journal of Hydrogen Energy. 2016;**41**:13341-13349. DOI: 10.1016/j.ijhydene.2016.06.205

[24] Gennero de Chialvo MR, Chialvo AC. Hydrogen evolution reaction on smooth Ni(1−x) + Mo(x) alloys ($0 \leq x \leq 0.25$). Journal of Electroanalytical Chemistry. 1998;**448**:87-93. DOI: 10.1016/S0022-0728(98)00011-4

[25] Fan C, Piron DL, Sleb A, Paradis P. Study of electrodeposited nickel-molybdenum, nickel-tungsten, cobalt-molybdenum, and cobalt-tungsten as hydrogen electrodes in alkaline water electrolysis. Journal of the Electrochemical Society. 1994;**141**:382-387. DOI: 10.1149/1.2054736

[26] Yapontseva YS, Dikusar AI, Kyblanovskii VS. Study of the composition, corrosion, and catalytic properties of Co-W alloys electrodeposited from a citrate-pyrophosphate electrolyte. Surface Engineering and Applied Electrochemistry. 2014;**50**:330-336. DOI: 10.3103/S1068375514040139

[27] Tsyntsaru N, Dikusar A, Cesiulis H, Celis J-P, Bobanova Z, Sidel'nikova S, Belevskii S, Yapontseva Y, Bersirova O, Kublanovsky V. Tribological and corrosive characteristics of electrochemical coatings based on cobalt and iron superalloys. Powder Metallurgy and Metal Ceramics. 2009;**48**:419-428. DOI: 10.1007/s11106-009-9150-7

[28] Kublanovsky VS, Yapontseva Yu S. Electrocatalytic properties of Co-Mo alloys electrodeposited from a citrate-pyrophosphate electrolyte. Electrocatalysis. 2014;**5**:372-378. DOI: 10.1007/s12678-014-0197-y

[29] Yapontseva YS, Gromova VA, Kublanovsky VS, Dikusar AI. Electrodeposition of Co-Mo alloys from a citrate-pyrophosphate electrolyte. Ukrainskii Khimicheskii Zhurnal. 2008; **74**:44-48

[30] Antropov LI. Theoretical Electrochemistry. Honolulu: University Press of the Pacific; 2001. 572 p

[31] Lee JK, Yi Y, Lee HJ, Uhm S, Lee J. Electrocatalytic activity of Ni nanowires prepared by galvanic electrodeposition for hydrogen evolution reaction. Catalysis Today. 2009;**146**: 188-191. DOI: 10.1016/j.cattod.2008.12.007

[32] Gromova VA, Yapontseva YS, Kulbanovskiy VS. Stripping analysis of electrolytic Co-Mo alloys obtained from a polyligand citrate-pyrophosphate electrolyte. Metallofizika i Noveishie Tekhnologii. 2008;**30**:467-476

[33] Saravanan G, Mohan S. Corrosion behavior of Cr electrodeposited from Cr(VI) and Cr(III)—Bathes using direct (DCD) and pulse electrodeposition (PED) techniques. Corrosion Science. 2009;**51**:197-202. DOI: 10.1016/j.corsci.2008.10.005

[34] Kublanovskii VS, Yapontseva YS, Troshchenkov YN, et al. Corrosion and magnetic properties of electrolytic Co-Mo alloys. Russian Journal of Applied Chemistry. 2010;**83**: 440-444. DOI: 10.1134/S1070427210030134

[35] Skibina L, Stevanivić J, Despić AR. ALSV investigation of the phase composition of electrolytic Cu + Sn alloys. Journal of Electroanalytical Chemistry. 1991;**310**:391-401. DOI: 10.1016/0022-0728(91)85274-S

[36] Vas'ko AT. Elektrokhimiya molibdena i vol'frama (Electrochemistry of Molybdenum and Tungsten). Kiev: Nauk. Dumka; 1977. p. 148

Edited by Abhijit Ray, Indrajit Mukhopadhyay and Ranjan K. Pati

The book starts with a theoretical understanding of electrocatalysis in the framework of density functional theory followed by a vivid review of oxygen reduction reactions. A special emphasis has been placed on electrocatalysts for a proton-exchange membrane-based fuel cell where graphene with noble metal dispersion plays a significant role in electron transfer at thermodynamically favourable conditions. The latter part of the book deals with two 2D materials with high economic viability and process ability and MoS_2 and WS_2 for their prospects in water-splitting from renewable energy.

Published in London, UK

IntechOpen

ISBN 978-1-83881-705-3